Manipulation of magnetic anisotropy in ferromagnetic semiconductors

Murat Cubukcu

THÈSE DE L'UNIVERSITÉ PIERRE ET MARIE CURIE – PARIS VI

SPÉCIALITÉ SCIENCES DES MATÉRIAUX

présentée par

MURAT CUBUKCU

pour l'obtention du titre de

DOCTEUR DE L'UNIVERSITÉ PIERRE ET MARIE CURIE – PARIS VI

Sujet :

MANIPULATION OF MAGNETIC ANISOTROPY IN FERROMAGNETIC SEMICONDUCTORS

Soutenue le 25 juin 2010 devant le jury composé de

Mr. JOERG WUNDERLICH – *Rapporteur*
Mr. JEAN MARIE GEORGE – *Rapporteur*

Mr. ALBERT FERT – *Président*
Mr. NITIN SAMARTH – *Examinateur*
Mr. MASSIMILIANO MARANGOLO – *Examinateur*
Mr. JURGEN von BARDELEBEN – *Directeur de thèse*

Institut des NanoSciences de Paris – UMR 7588
Université Pierre et Marie Curie – Paris VI

Acknowledgments

First, I would like to thank the jury who evaluated my thesis. I would like to thank **Joerg Wunderlich** from "Hitachi cambridge laboratory" of United Kingdom and **Jean-Marie George** from "Unité Mixte de Physique CNRS/Thales" of France who agreed to be my referees. Thanks very much also to my teacher **Albert Fert** from "Unité Mixte de Physique CNRS/Thales" of France who was the president of the committee, generous to spend a part of his time on this thesis. I would like to extend my sincere gratitude to my examiners: **Nitin Samarth** from "Pennsylvania State University" of United State America and **Massimiliano Marangolo** from "Université Pierre et Marie Curie" of France. Dear Nitin, I want to thank you especially for all the helpful discussions we had. The presence of these researchers in my PhD jury is a great honour for me.

This thesis has been prepared within the Institut des NanoSciences de Paris. I would like to thank **Bernard Perrin**, director of the institute, allowing me to pursue this thesis in the best conditions.

I would like to thank **Jürgen von Bardeleben**, my supervisor most sincerely for his support, his patience and the new ideas he put in this thesis. He encouraged me to develop the abilities essential to research during these three years. Thanks again dear Jürgen for allowing me to travel in different countries for the conferences or school during this thesis. I want to specially thank you for that rock concert in the evening after the MMM conference at Washington. My thanks also go to my second supervisor **Jean-Louis Cantin** and my colleague **Khashayar Khazen**. Thank you to dear Jean-Louis for the time you spent in editing my thesis and all our friendship. Thank you to dear Khashayar for your support.

I also have to thank **Aristide Lemaître** and **Adeline Maître** from "Laboratoire de Photonique et de Nanostructures" in Marcoussis for supplying us with many very high quality GaMnAs and GaMnAsP monolayers and multilayers GaMnAs samples and electrical transport measurements. Dear Adeline I wish you an excellent thesis. I would like to thank also **Ludovic Largeau** and **Olivia Mau-**

guin for X-ray diffraction measurements.

I must also acknowledge **Meng Zhu**, **Marc Wilson** and **Peter Schiffer** from Pennsylvania State University" for providing us MnAs/GaMnAs bilayers and MnAs monolayers samples.

I would like to thank **Catherine Gourdon**, **Laura Thevenard** and **Sanaz Haghgoo** for the Kerr-Effect measurements and the domain wall studies in the GaMnAsP samples. I would also like to thank **Ian Vickridge** for helping me in the RBS measurements and analysis.

I should thank all the members of our Institute, for supporting me in different occasions. I would like to specially thank **Tristan Cren** and **Bernard Croset** for their kindness, their support, listening and consulting. Thanks a lot dear Tristan for your contribution to energy surface representations.

I should address most special acknowledgements to my parents and my friends. Particularly, I want to thank my sister **Leyla** whose support is indispensable to me.

I dedicate this thesis to my parents.

Contents

Introduction

The subject of my thesis manipulation of magnetic anisotropies in ferromagnetic thin epitaxial semiconducting layers is situated in the field of spintronics. In spintronics it is the spin dependent electronic transport properties which are used to create new structures and functionalities. It was first exploited in purely metallic materials and was highlighted by the 2007 Nobel prize in Physics awarded to Albert Fert and Peter Grünberg. The interesting challenge is to combine these functions with semiconductor materials of technological importance such as Si and the III-V compounds. Materials naturally magnetic and semiconductor in nature, like (EuO, GdN) do exist but their Curie temperature remains low essentially due to the weak magnetic coupling of the localized electrons of the magnetic atoms and the delocalized electrons. They are usually also difficult to grow and their quality remains far from the semiconductor technology grade. Their low Curie temperature, large defect concentrations, difficulties of doping, and weak compatibility with existing semiconductor technology render these materials not well suited for applications up to now.

The alternative route is to render artificially magnetic a conventional semiconductor material. This is a priori possible by convincing a magnetic impurity to incorporate the semiconductor matrix. The material is then called: "Diluted Magnetic Semiconductor" (DMS). A theoretical work by Dietl et al.[37] based on mean field calculations predicted ferromagnetism above room temperature for different p type semiconductors doped with 5% of magnetic Mn ions. The danger of this approach, where magnetism is induced by extrinsic atoms, is of course to generate ferromagnetism from magnetic clusters or second phase formation during the growth of the alloys. Up to now, experimental results do not confirm these predictions which have been, in the meantime, questioned by others, but nevertheless a large numbers of experimental and theoretical studies have been initiated in this context.

So far, only the (III,Mn)V alloys have shown to satisfy to predictions of ferromagnetism. Among them, (Ga,Mn)As is the best understood DMS material and has

been widely studied in the last decade. It becomes ferromagnetic for Mn concentration higher than 1%, but can be prepared with much higher Mn concentration, up to 25%, thanks to sophisticated growth techniques. A Curie temperature up to 195 K has been demonstrated. The high quality of this system allows to use it as a model system to understand and test the coupling between the ferromagnetic ordering and external parameter to "tailor" its ferromagnetic properties. Whereas its basic properties are well known hybride structures dedicated to manipulate the anisotropies and the Curie temperature by external perturbations such as an electric field, optical spin injection or by applying a strain are now actively studied. In this field (Ga,Mn)As has some limitations linked to the dependence of all properties on the Mn doping level. I will show in this work that quaternary alloys with phosphorous are a promising alternative as the strain can be modulated widely and independently from the Mn.

In my PhD work, I have studied for the first time the magnetic properties of such quaternary ferromagnetic alloys (Ga,Mn)(As,P). My results confirm that these alloys have indeed some important advantages over (Ga,Mn)As and can be grown with excellent quality by LT-MBE on GaAs substrates. Whereas in (Ga,Mn)As the magnetic anisotropy is intimately related to the Mn doping level and cannot be changed easily in an independent way this can be done in the (Ga,Mn)(As,P) epitaxial films via the phosphorous concentration. I have shown that it is possible to engineer the easy axis of magnetization to in-plane or out-of-plane with adequate phosphorous doping. With intermediate P levels critically strained layers with negligible uniform anisotropy can also be obtained. In addition the electronic properties of the Mn acceptor change also with the phosphorous concentration which allows us to explore different conductivity regimes (free carriers/ impurity band conduction). The results of combined FMR, SQUID and transport measurements on epitaxial (Ga,Mn)(As,P) layers with different phosphorous and Mn concentrations grown by low temperature MBE on GaAs(001) are presented in Chapters 3 and 4.

MnAs is an interesting ferromagnetic metal which can also be grown epitaxially on GaAs and (Ga,Mn)As. It is ferromagnetic up to room temperature and presents a mixed phase between 0°C and 30°C which gives rise to to self organized stripes of ferromagnetic alpha phase and paramagnetic beta phase regions. We have studied the magnetic anisotropy of ultrathin MnAs layers grown on GaAs(111) and (Ga,Mn)As(001) by FMR spectroscopy and SQUID. Due to the high intrinsic anisotropy of the hexagonal MnAs we had to use high frequency FMR (115GHz) to

perform these studies. We have equally investigated the coupling between the two ferromagnetic layers in MnAs/GaMnAs bilayers. The results are given in chapter 5.

The magnetization dynamics will be of importance for device applications as it limits the device speed. The rate at which magnetization reach equilibrium is described by the Gilbert damping factor, introduced in the Landau-Lifschitz equation as a phenomenological term. It was recently shown that it could be justified by first principles calculations of the time evolution of spin observable in the presence of the spin orbital terms [73]. Our results presented chapter 6 questioned the scalar nature of the damping factor considered up to now to describe the relaxation phenomenon and the magnetic domain wall propagation.

Before presenting the experimental results, I will review in the first chapter the general properties of (Ga,Mn)As and (Ga,Mn)(As,P) alloys and will then introduce briefly, in chapter 2, the basis of the experimental methods that were mainly applied in this work.

Chapter 1

Ferromagnetic Semiconductors

1.1 Spintronics

Spintronics, a subject at the intersection between magnetism, micro-electronics and nano-physics, is a new field of research which is in rapid expansion. Spintronic devices based on the giant magneto-resistance (GMR) are one of the key elements in information technology. The GMR, discovered by Albert Fert and Peter Grünberg in 1988 (for which they obtained the 2007 Nobel Prize in Physics) [1, 2], exploits the influence of the spin of the electrons on the electrical conduction in a magnetic multilayer composed of alternate ferromagnetic and non-magnetic layers, Fe and Cr for example. Since then, other promising new subjects have been developed like the phenomena of spin transfer, spintronics with semiconductors, molecular spintronics or single-electron spintronics [59, 60, 8].

Spintronics with semiconductors should ideally rely on the use of ferromagnetic semiconductors compatible with technologically important materials like Si, Ge or the III-V compounds. However these basic semiconductors are not ferromagnetic but can be made so when alloyed with magnetic impurity ions; $Ga_{1-x}Mn_xAs$ is such a case and has been widely studied in the last decade. Its fundamental properties are now well known and more sophisticated hybrid structures are currently under investigation as they allow electrical or optical control of its properties. A particular effort is dedicated to the control of the magnetic anisotropies by an applied electric field [24, 23], as well as the study of TMR (Tunnel Magnetoresistance) and TAMR (Tunneling Anisotropic Magnetoresistance) effects [47, 48].

1.2 Diluted magnetic semiconductors (DMS)

Diluted magnetic semiconductors (DMS) can be realized by alloying with magnetic ions most often 3d transition metal ions. The semiconductor GaAs which is widely used in micro-electronic has attracted most attention due to the relatively high Curie temperatures which already been obtained and the even higher ones predicted. To make these materials ferromagnetic Mn is a dopant of choice due to the high spin state of the Mn^{+2} ion and its high solubility.

The DMS materials have some advantages intimately related to their band-structure, lower carrier concentrations and longer spin coherence length as compared to metallic ferromagnetic layer.

In II-VI based DMS, the magnetic interaction is generally dominated by anti-ferromagnetic super-exchange, which leads to anti-ferromagnetic or spin-glass behavior. Long range ferromagnetic ordering even though with a low critical temperature has been demonstrated in some II-VI DMS, (Cd,Mn)Te [50], (Zn,Mn)Te [58] and room temperature ferro-magnetism in (Zn,Mn)Te [137]. Contrary to mean field theory predictions by Dietl et al.[34], of Curie temperatures near room temperature for 5 % Mn doped p-type GaN and ZnO reliable experimental results for such materials have not yet been reported.

Carrier-induced ferromagnetism has clearly been observed in different III-V DMS epitaxial films. The first publication concerned $In_{1-x}Mn_xAs$ [108, 113] and later $Ga_{1-x}Mn_xAs$ [14]. These films had to be grown by low temperature molecular beam epitaxy (LT-MBE) to allow the incorporation of magnetic atoms at considerably higher concentration than possible under thermal equilibrium conditions. Due to the acceptor character of the Mn dopant they are p-type III-V DMS the magnetic properties of which are strongly influenced by the valence band structure and the hole concentration [111].

1.3 Diluted ferromagnetic III-V semiconductors: $Ga_{1-x}Mn_xAs$

In this section I will first present the lattice and electronic structure of the III-Mn-V DMS $Ga_{1-x}Mn_xAs$. Then I will address the current understanding of the origin of the ferromagnetism in this material and finally discuss how the valence band structure and magnetic anisotropies are related.

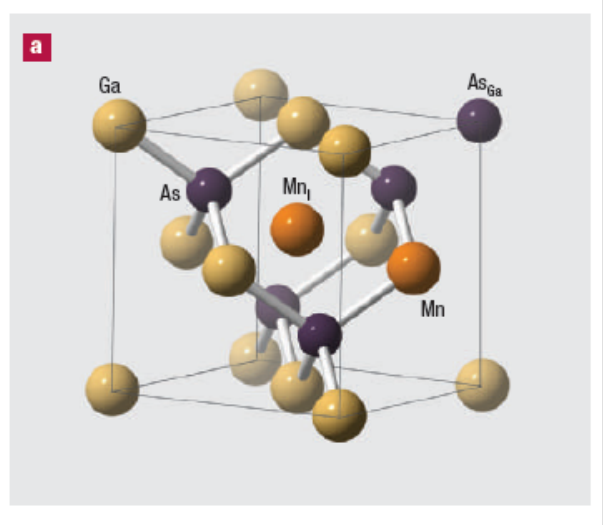

Figure 1.1: Lattice of $Ga_{1-x}Mn_xAs$ showing unit cell with defects: Mn_I and As_{Ga} are represent Mn interstitial and As anti-site respectively[100].

1.3.1 Lattice Structure

III-Mn-V DMS $Ga_{1-x}Mn_xAs$ crystallizes in the zinc-blende structure. In fig. 1.1, we show the GaAs unit cell with the relevant defects induced by the growth conditions. For low doping levels the Mn atom substitutes exclusively a Ga atom, whereas for higher doping levels ($> 10^{19}cm^{-3}$) Mn interstitial (Mn_I) ions are also formed. The incorporation of Mn at several at % does modify the lattice constant from that of undoped GaAs. The low temperature MBE growth introduces also other native defects, in particular arsenic anti-site (As_{Ga}) defects which are known to further modify the lattice constant. The electrical compensation in these films can not be neglected due to the presence of these defects which are both double donors [80]. When Mn is incorporated on a Ga site, it is a single acceptor, providing the holes required to mediate the ferromagnetic interaction between the local magnetic moments of the substitutional Mn atoms. The solubility of Mn in the GaAs matrix at thermal equilibrium under normal growth conditions is only about 0.1 %. To increase the doping above this level a non equilibrium growth technique, low temperature molecular beam epitaxy (LT-MBE) is required. With this technique total Mn concentrations of up to 20 % have been achieved in ultra-thin films.

The magnetic properties of as grown films are deceiving: low critical temperatures (< 50K) and low hole concentrations ($< 10^{20}cm^{-3}$). Post growth thermal annealing at temperatures between 200 °C and 250 °C allows to overcome at least partially this problem due to the out-diffusion of interstitial Mn ions to the surface.

The efficiency of the annealing depends on the surface state: free surface, presence of capping layers such as GaAs or a-As and is further influenced by the annealing atmospheres such as nitrogen, oxygen, air and vacuum. Each laboratory uses slightly different annealing conditions as concerns the duration and temperature, atmosphere for the optimization of the films. In our case standard conditions of 1h annealing at 250°C under vacuum have been used.

Post growth thermal annealing is an important treatment necessary to optimize the magnetic properties of $Ga_{1-x}Mn_xAs$. The thermal annealing allows to modify the defect concentrations, mainly Mn_I. Thus the electrical compensation and the lattice mismatch related strain are modified. According to calculations based on the full-potential linearised plane-wave method, substitutional Mn will reduce the lattice constant whereas the presence of As_{Ga} and Mn_I lead an expansion of the lattice constant [103]. As the concentrations of the As_{Ga} and Mn_I defects are in general not known and in fact not easy to determine correlations between defects concentrations and lattice constants are rather unreliable [135, 172].

The As anti-site defects are not removed by this low temperature annealing. They are stable up to 450 °C but such high annealing temperatures cannot be used as they would precipitate the substitutional Mn ions and form granular layers with embedded MnAs clusters. The As anti-site concentration is also sensitive to the growth conditions: th use of As_2 dimer molecules instead of As_4 during the MBE growth[19] and a low As/Ga flux ratio[52] will reduce its importance .

1.3.2 Electronic Structure of substitutional and interstitial Mn

The electrical properties of the manganese ions in $Ga_{1-x}Mn_xAs$ depend strongly on the crystallographic position. We consider here first the case where the Mn is located on the Ga cation site. In $Ga_{1-x}Mn_xAs$, the atoms have the following electronic configurations: [Ar]$3d^{10}4s^{\ 2}\ p^1$ for Ga, [Ar]$3d^5 4s^{\ 2}$ for Mn, and [Ar]$3d^{10}\ 4s^2p^3$ for As.

As the Mn atoms are substituted for trivalent cations they introduce an acceptor state which in the neutral charge state A^0 should lead to a Mn^{+3} ground state. However due to a high de-localization of the hole wave-function the ground-state is usually described by the configuration ($3d^5$+hole) which leaves the Mn ion in the high S=5/2 spin state. The neutral and ionized Mn ion in highly doped samples with de-localized holes will have a ${}^6A_1$ ground-state (zero angular momentum (L=0)

and spin S=5/2) and a Landé g factor g=2.00. The tetrahedral crystal field induces a splitting of the 3d levels of Mn into two groups, t_{2g} ($3d_{xy}$, $3d_{xz}$,$3d_{yz}$) and e_g ($3d_{x^2-y^2}$, $3d_{z^2}$). These levels are further modified by the p-d hybridization. Electron spin resonance(ESR) [152] measurements and infra-red absorption measurements [95] have been used to determine the ground state of the Mn atoms. Depending on the dopant concentration the associated p-type conductivity is either thermally activated, impurity band type or metallic for the highest doping values.

GaAs is an intermediate band-gap material with a gap energy of E_g=1.5 eV at low temperature (T≈0). The substitutional Mn dopant introduces an acceptor level -/0 at 113 meV above the valence band [169], with a Bohr radius of a_B=7.8 A°. When the concentration of the Mn increases above $10^{18}cm^{-3}$ the acceptor states will start to overlap and form an impurity band. At high Mn (x>0.03) concentration the impurity band will merge with the valence band, leading to the insulator-to-metal transition characterized by a temperature independent resistivity [78].

The role of interstitial manganese in $Ga_{1-x}Mn_xAs$ has been studied by Kacman et al.[39]. In principle Mn_I can occupy either a tetrahedral or a hexagonal interstitial site. The main information about the actual site occupation stems from PIXE and RBS channelling experiments. According to these results Mn_I occupies mainly one tetrahedral interstitial site surrounded by negatively charged As nearest neighbors. As in p-type material the Mn_I donor will be fully ionized (Mn_I^{+2}) with a ground state $^6A_1$ one might wonder whether it can contribute to the ferromagnetic phase. According to Kacman et al.[39] Mn_I^{+2} has only a negligible kinetic exchange constant and will thus not be expected to contribute to the ferromagnetism in such layers. However, if they occupy sites near a substitutional Mn ion anti-ferromagnetic coupled Mn_{Ga}-Mn_I pairs will form with a coupling energy of 0.3 eV which will reduce the magnetization of the layers.

1.3.3 Origine of Ferromagnetism

1.3.3.1 Exchange Interaction

Exchange interaction is the source of the long range magnetic order in ferromagnetic materials. It is basically an electrostatic interaction, reflecting the energy gain arising from the separation of charges of the same sign. Indeed, when electrons have the same spin state, the orbital wave function must be antisymmetric, lowering the probability to find electrons close together.

If the exchange interaction occurs between electrons localized on neighboring

ions, it is called direct exchange. Because efficient direct exchange implies an important overlap of the magnetic ions wave functions, it does not explain the magnetic ordering occurring in many magnetic materials, and especially in DMS, for which indirect exchange interactions are generally predominant.

Super-exchange (Kramer) is a mechanism which allows to increase the range of the direct exchange. Super-exchange interaction can couple two magnetic ions separated by a non magnetic atom. The interaction is mediated by the non magnetic ion which becomes spin polarised because the transfer of one of its electron to one of its magnetic neighbour is spin dependent. In (III,Mn)V alloys, super-exchange contributes to anti-ferromagnetic interaction between neighbouring Mn.

Double exchange (Zener) occurs when the magnetic ions have a mixed valency. Manganese for example undergoes double exchange in substoichiometric $LaSrMnO_3$ where both the Mn^{+3} and Mn^{+4} oxidation states coexist. The coupling is, in this case, explained by the difference in the probabilities, for one electron of a given spin state, to hop from one magnetic ion to another. The hopping is indeed much less probable if the electron is not spin polarised like the electrons of the receiving ions. In (III,Mn)V materials, a different type of double exchange -kinetic exchange- controls the magnetic properties of low doped films and wider gap materials. Indeed, Mn acceptor states at concentrations beyond the Mott transition form an impurity band, participating to the electrical conduction, and thus induce a carrier mediated double exchange between Mn^{+2} ions.

Carrier mediated exchange interaction can be also encountered in metals where the conductions electrons are spin polarised by interaction with the localised moments of magnetic ions. This indirect exchange mechanism was formalised by Ruderman, Kittel, Kasuya and Yosida and is called RKKY interaction. The exchange coupling constant depends on r, the distance between the localised moments and, assuming a spherical Fermi surface of radius k_F, is proportional to $\cos(2k_F r)/r^3$. Consequently, the sign of the coupling depends on the distance between the magnetic ions (i.e. their concentration), which can then be either ferro- or antiferromagnetically coupled.

Finally, kinetic exchange (Zener) applies to localised moment coupled through polarised itinerant carriers. The s- or p- band itinerant carriers propagate the spin polarisation between the localized moments. When the coupling is weak (weak polarisation of the carrier) the effect is well described by the RKKY theory.

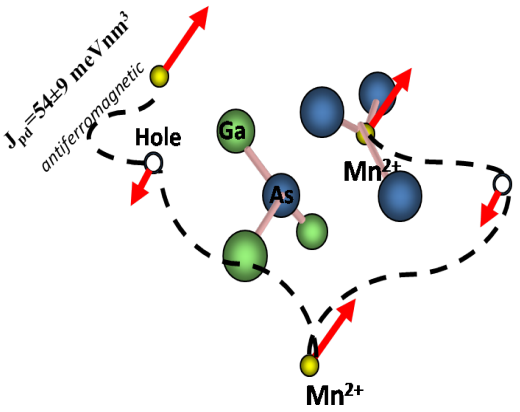

Figure 1.2: Schmetic presentation of two coupled system: a direct antiferromagnetic interaction between the itinerant holes and the localized Mn magnetic moments and an indirect ferromagnetic interaction between the Mn magnetic moments resulting from their coupling to the holes.

1.3.3.2 Carrier Induced of Ferromagnetism

In $Ga_{1-x}Mn_xAs$, the interaction between the magnetic moments of the Mn ions depends strongly on the conductivity regime, i.e., impurity band or metallic conduction and the Mn (magnetic moment) concentration [79]. The dipole-dipole interaction between Mn ions can be neglected for $Ga_{1-x}Mn_xAs$ because of the DMS nature of this material, which leaves the electron spin, the Pauli exclusion principle and the repulsive Coulomb interaction, as the principal parameters determining the ferro-magnetism.

The number of local moments participating in the ordered state and the number of holes may differ from the number of substitutional Mn impurities in the system due to presence charge and moment-compensating defects and an effective Mn doping must be given in addition to the total doping level.

At low dopant concentrations the average distance between substitutional Mn impurities is much larger than the impurity effective Bohr radius. In this case the holes remain localized at the Mn ions [121]. Ferromagnetism has only been observed for doping concentrations above 1% [125, 115].

At even higher Mn concentration the impurity band gradually merges with the valence band [88] and the impurity states become fully de-localised. In these metallic ferromagnets $Ga_{1-x}Mn_xAs$, the coupling between Mn local moment is mediated by the p-d kinetic-exchange mechanism [35, 38, 105, 76, 78] (fig. 1.2).

1.3.4 Band Structure

As the de-localised carriers in degenerate $Ga_{1-x}Mn_xAs$ films are in the valence band of the GaAs host material, they can be described in $\overrightarrow{k}.\ \overrightarrow{p}$ perturbation theory. The valence band in GaAs consists of four subbands when spin is neglected and each band is twofold degenerate is the spin is included. Three of the bands are degenerate at $\overrightarrow{k} = \overrightarrow{0}$ and form the upper edge of the band. The two top valence band can be approximately described by parabolic bands with different curvatures, the so-called heavy hole (HH) and light hole (LH) bands. The total Hamiltonian is composed of the Kohn-Luttinger $\overrightarrow{k}.\overrightarrow{p}$ Hamiltonian, the p-d exchange term, the strain Hamiltonian and the one of the Zeeman effect:

$$H_{tot} = H_{k.p} + H_{echange} + H_{strain} + H_{Zeeman} \tag{1.1}$$

In the absence of the exchange interaction and the strain, the heavy holes ($j_z = \mp 3/2$) and the light holes ($j_z = \mp 1/2$) constitute the band Γ_8 which is four times degenerate at the center of the Brillouin zone. They are mainly composed of the hybridized As sp orbitals. The lower valence band Γ_7 is separated by the spin orbit coupling, $\triangle_{SO}$, by 340 meV which in GaP reduces to 80 meV.

The exchange Hamiltonian between the 3d electrons ($\vec{S_i}$) of Mn and the carriers ($\vec{\sigma_j}$) can be written in the following way:

$$H_{ech} = \sum_{i,j} J(r_{ij})\ \vec{S_i}\vec{\sigma_j} \tag{1.2}$$

It is in general solved within the mean field and virtual crystal approximations. The exchange Hamiltonian between the valence and conduction bands and the localised 3d electrons of Mn (i.e. H_{sd} and H_{pd} respectively) can then be written as:

$$H_{sd} = -x_{Mn}N_0\alpha <\vec{S}> .\ \vec{\sigma} \tag{1.3}$$

$$H_{pd} = -x_{Mn}N_0\beta <\vec{S}> .\ \vec{\sigma} \tag{1.4}$$

where $<\vec{S}>$ is the mean field magnetic spin, x_{Mn} magnetic ion concentration. Here, symbol β used for comparison with the case DMS II-VI where its is used instead of the pd exchange interaction (J_{pd}) and N_0 instead of J_0. There is no report concerning measurements of $N_0\alpha$ for $Ga_{1-x}Mn_xAs$. Its value in II-VI magnetic semiconductor has been measured as 0.2 eV [63]. The exchange integral constant, obtained from photo-emission measurements is J_{pd}=54 $\mp$ 9 meV nm^3 [116].

A non-zero magnetization oriented parallel to the z-direction, will split the conduction band and valence bands:

$$\triangle E_c = x_{Mn} N_0 \alpha < S_z > \sigma_z \tag{1.5}$$

$$\triangle E_v = x_{Mn} N_0 \frac{\beta}{3} < S_z > j_z \tag{1.6}$$

The shift of the energy of the heavy holes ($j_z = \mp 3/2$) is 3 times larger than that of the light holes ($j_z = \mp 1/2$).

The tetragonal deformation of the lattice induced by the lattice mismatch between the film and the substrate lifts the degeneracy of the heavy and light holes which split by an amount of $2\mathrm{b}Q_\epsilon$. b is the deformation parameter (for GaAs is =1,7). Neglecting the hydrostatic deformation Q_ϵ it can be expressed as a function of the tensorial deformation ϵ_{ij} and the elastic moduli by:

$$Q_\epsilon = \epsilon_{zz} - \frac{\epsilon_{xx} + \epsilon_{yy}}{2} = \epsilon_{xx} |1 - 2\frac{C_{12}}{C_{11}}| \tag{1.7}$$

The sign of the epitaxial strain has a direct impact on the relative position of of the light and heavy hole bands at $\overrightarrow{k} = \overrightarrow{0}$. It is shown that the effect is opposite for the layers under compression or extension.

At the center of the Brillouin zone, the exchange coupling can be expressed in terms of the reduced in-plane and normal-to-plane magnetization, $m_{xy} = \frac{M_x^2 + M_y^2}{M^2}$ and $m_z = \frac{M_z}{M}$ respectively given by:

$$\triangle_{\varepsilon_{HH}} = 6 B_G m_z \tag{1.8}$$

$$\triangle_{\varepsilon_{LH}} = 2 B_G \sqrt{m_z^2 + 4 m_{xy}^2} \tag{1.9}$$

where $B_G = \frac{\beta M}{6 g \mu_B}$ is the hole splitting parameter. The heavy holes are pure spin states $[(X \mp Y) \uparrow]$, while the light holes are mixed states $[(X \mp Y) \uparrow \mp 2Z \downarrow]$.

The valence band is anisotropic, due to the non-parabolic character of the bands, the spin-orbit coupling, the epitaxial strain, and the exchange interaction.

1.3.5 Magnetic Anisotropy

The strong spin-orbit coupling interaction makes the band structure sensitive to the direction of the magnetization which gives rise to magneto-crystalline anisotropy.

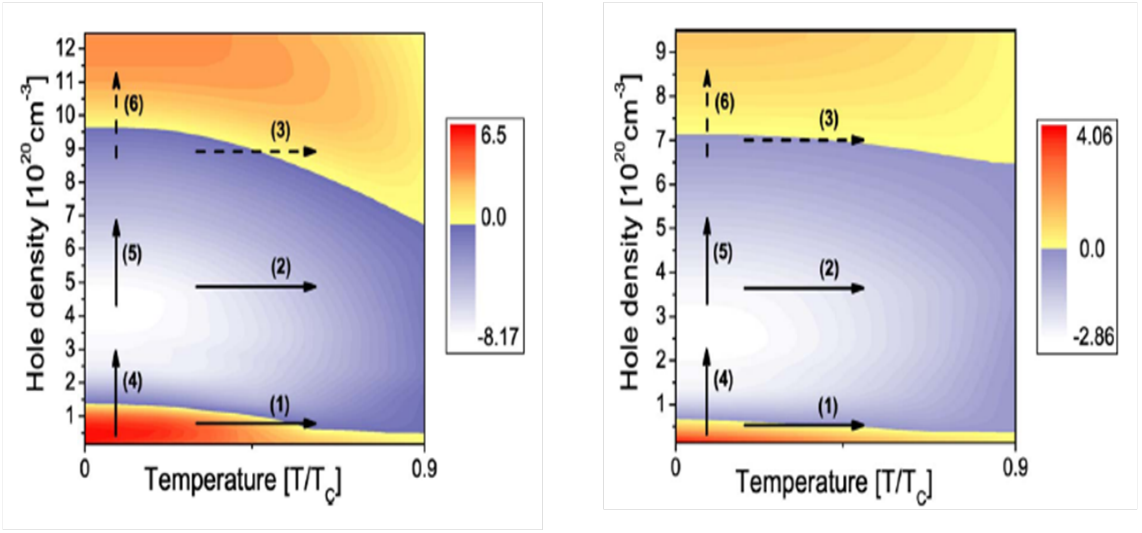

Figure 1.3: Anisotropy energy $\triangle$E=$E(M_{\parallel})$-$E(M_{\perp})$ (kJ m^{-3} calculated for x=8% (left) and x=4% (right), strain tensor e_0=-0.2%. Positive(negative) $\triangle$E corresponds perpendicular easy axis (in-plane easy axis). Arrows mark anisotropy transitions driven by a change of temperature and hole density[171].

1.3.5.1 Shape Anisotropy

Magnetic shape anisotropy is the consequence of long-range dipolar interaction. The surface divergence of the magnetization gives rise to a demagnetization field. The shape anisotropy energy per unit volume is E_A=$\frac{\mu_0}{2}\mathbf{M}^2 cos^2\theta$, where θ is the angle that saturation magnetization **M** subtends to the normal plane. Because of the small value of the saturation magnetization in the DMS, the in-plane vs out-of plane shape anisotropy E_A is only about 1.4 kJ/m^3 (0.06 T) for Mn doping x=5 % [171].

A main property of $Ga_{1-x}Mn_xAs$ is the fact that the shape anisotropy is weak as compared to the spin-orbit coupling induced magneto-crystalline anisotropy.

1.3.5.2 Magneto-crystalline Anisotropy

The magnetization measurements have shown that the in-plane or perpendicular-to-plane easy axis direction is exclusively determined by the sign of the growth-induced strain in typically at 5 % Mn doped thin films on GaAs(001). An in-plane easy axis develops for films with compressive strain whereas a tensile strain results in a perpendicular-to-plane easy axis. The magneto-crystalline anisotropy varies with the strain, hole density, Mn concentration and temperature. Recently, Zemen et al.[171] have published a detailed calculation of the easy-axes of magnetization for

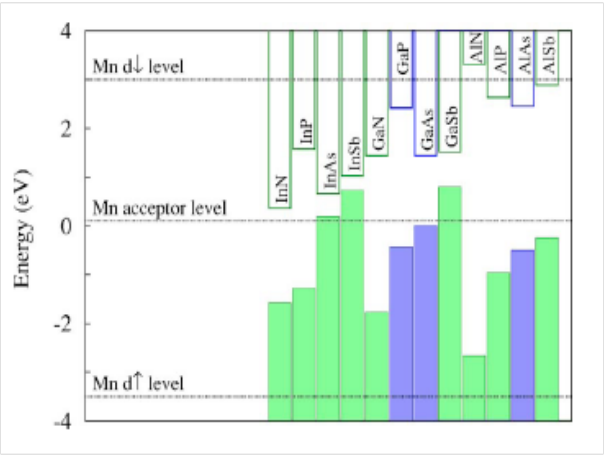

Figure 1.4: Valence band and conduction band offsets across the family of III-VI semiconductors. The Mn acceptor level is kept constant in this diagram according to the empirical internal reference rule[102].

various configurations and compared them with the published experimental results [140, 157, 158, 138, 97]. A change of orientation of the easy axes can be induced by changes in the material parameters, i.e., Mn concentration, hole concentration, strain and by the temperature. In fig.1.3, we show the difference $\triangle$E in the total energy density for the magnetization lying in-plane $[E_{tot}(M_{\parallel})]$ and out of plane $[E_{tot}(M_{\perp})]$ as a function of the hole density and temperature for a compressive strained film. Solid arrows mark easy axis behavior as a function of doping and temperature which have been observed experimentally. At low hole densities, the reorientation with increasing temperature of the easy axis from a perpendicular-to-plane to an in-plane direction has been observed. Increasing the temperature at high hole densities can induce a switching of the easy direction from in-plane to perpendicular to-plane. The in-plane easy axis direction is also a function of strain, temperature, Mn and hole concentration and the [100], [110] and [1-10] directions are not equivalent.

The components of the magneto-crystalline anisotropy can be described in terms of the free energy density with terms dependent on the crystal symmetry. In the mean field model two anisotropy constants (uni-axial and cubic) with in-plane and out-of-plane components had to be introduced to interpret the experimental findings. All these parameters and their contribution to the determination of the easy axes are discussed in detail in the following chapter.

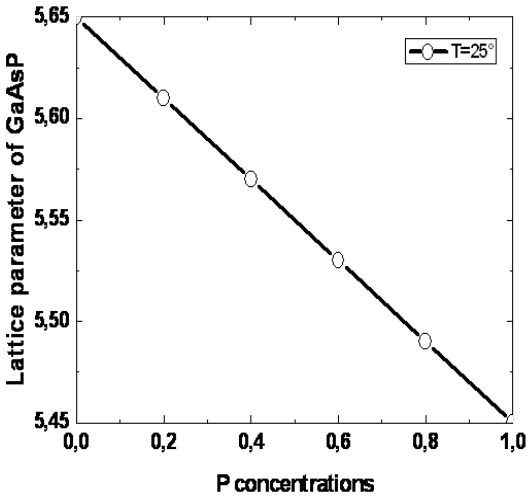

Figure 1.5: Variation of the lattice parameter of GaAsP as a function of P concentration for T=25°[127].

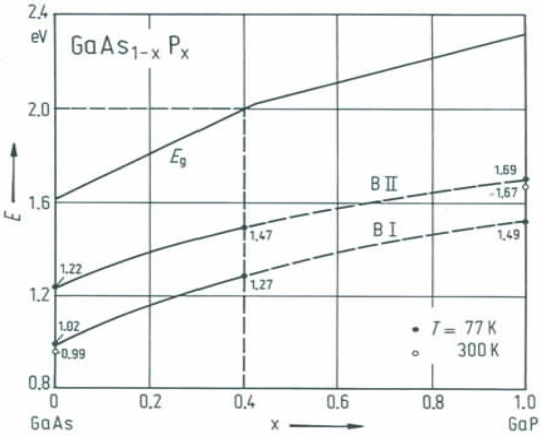

Figure 1.6: Band gap energy and peak energy of two photo-luminescence bands B I, B II as a function of Phosphorous concentration; T=77 K[53].

1.4 Quaternary ferromagnetic semiconductors: $Ga_{1-x}Mn_xAs_{1-y}P_y$

The related III-V compound GaP has been extensively studied as concerns its electronic structure and the electronic states introduced by the 3d transition metal ions such as Mn [11, 28]. GaP is a high gap indirect band semiconductor. As shown in fig.1.4 the valence band maxima and conduction band minima shift to higher energies as compared to GaAs when the Mn vacuum level is taken as a reference[102]. GaP has a smaller lattice constant than GaAs, favoring a priori a stronger exchange interaction in GaMnP. However the wider bandgap results in a stronger localisation of the holes which modifies the electronic states of the Mn acceptor into Mn^{+2} and Mn^{+3}. In fact, there have been no reports of a metallic conduction state in GaMnP. Scarpulla et al.[141] have prepared GaMnP by ion implantation followed by pulse laser annealing with maximum x≈0.06 and T_c=60K [141]. These authors found that the samples prepared by this technique were always insulating. The two times smaller Curie temperature of GaMnP compared to GaMnAs prepared under similar condition has been attributed to the shorter range of the magnetic interaction in the impurity band regime.

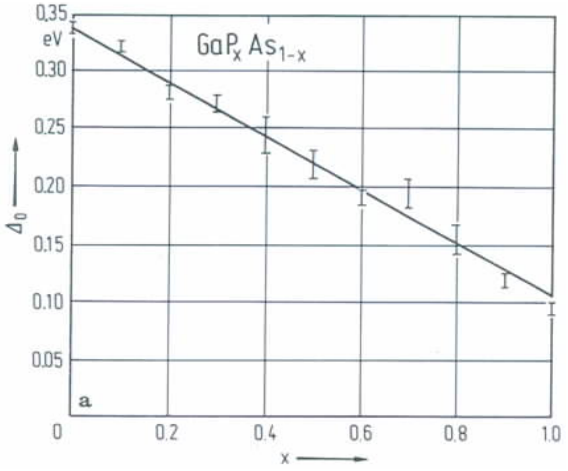

Figure 1.7: Composition dependence of the spin orbit splitting energy $\triangle_0$ of the valence band[56].

The mean-field T_c calculation by Masek et al.[102] have predicted an increase of the Curie temperature in highly doped GaMnAsP alloys. In the mean-field kinetic-

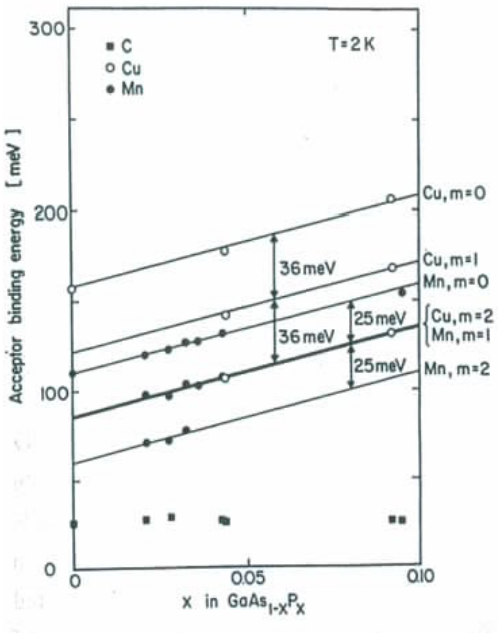

Figure 1.8: Estimated energy positions relative to the valence band maximum of the Cu and Mn deep defects and the shallow C center vs the alloy composition[54].

exchange model the Curie temperature of a $III_{1-x}Mn_xV$ magnetic semiconductor scales as $T_c \propto J_{pd}^2 x/\Omega_{u.c}$ [102],

$$T_c \propto a_{lc}^{-11}(1/|E_{d\uparrow}| + 1/|E_{d\downarrow}|)^2 \tag{1.10}$$

where J_{pd} is kinetic-exchange interaction, $\Omega_{u.c}$ is the volume of the unit cell of the zinc-blende crystal with a lattice constant a_{lc} and $|E_{d\uparrow}|$ and $|E_{d\downarrow}|$) are the distances of the occupied and empty atomic Mn d levels from E_F. The second term in eq.1.10 is compared for GaAs and GaP. T_c strongly depends the first term in eq.1.10 which considering $a_{lc} = 5.653$ A° for GaAs and $a_{lc} = 5.450$ for GaP.

The increasing ionization energy of the Mn acceptor level with the P concentration is a factor that may reduce the formation of interstitial Mn ions [102]; this makes these alloys interesting for high doping studies.

$GaAs_{1-y}P_y$ forms a solid solution over the whole composition range y=0 to y=1. Its structural and electronic properties vary monotonously between those of GaAs and GaP. In fig.1.5, we show the variation of the room temperature lattice constant

a as a function of the alloy composition. We observe a linear variation from 5.65 A° in GaAs to 5.45 A° in GaP corresponding to the Vegard law. The variation of the bandgap is non-linear as it changes from direct band gap for y<0.45 to indirect bandgap for y>0.45 (fig.1.6) [53].The fact that P alloying decreases the lattice constant turns out to be a convenient parameter to control the lattice mismatch between the $Ga_{1-x}Mn_xAs_{1-y}P_y$ epitaxial film and the GaAs substrate. This leads to strong changes in the magneto-crystalline anisotropy as investigated in detail in the following chapter. The spin orbit splitting of the valence band varies equally with the P composition: it decreases linearly from 350 meV in GaAs to 110 meV in GaP (fig.1.7) [56]. The ionization energy of the Mn acceptor varies linearly for $0< y <10$. In fig.1.8, we show its variation determined from low temperature donor-acceptor photoluminescence spectra[54]. The multiple peak structure of this PL band had been interpreted in terms of slightly different ionization energies depending on the nearest neighbour configurations $MnAs_{1-m}P_m$ (m=0...4). In our highly doped sample this distinction will smear out in a broadened band. The ionization energy of 400 meV in GaP determined from Hall effect, DLTS and photoionization measurements shows the variation to be linear over the entire alloying range.

1.5 Manipulation of magnetic properties in ferromagnetic semiconductors

As discussed above, the anisotropic valence band structure, which depends on the direction of the magnetization as well as on the hole concentration and strain, are responsible for the magneto-crystalline anisotropy. The manipulation of the magnetization through modification of the strain and hole concentration have already been investigated.

The manipulation of the magnetic properties of a ferromagnetic semiconductor by applying electric fields is of interest for applications in microelectronic and spintronics devices. Ferromagnetic semiconductors $Ga_{1-x}Mn_xAs$ and related alloys such as $Ga_{1-x}Mn_xAs_{1-y}P_y$ give the opportunity to control the electronic and magnetic properties by applying small voltages. The key issue is the hole concentration dependence of the magnetic anisotropies in diluted ferromagnetic semiconductors.

Chiba et al.[24, 23] demonstrated that electrical manipulation of the magnetic properties in a ferromagnetic semiconductor $Ga_{1-x}Mn_xAs$ with low-hole concentrations is possible. These authors have observed that the uni-axial anisotropy $\mu_0 H_U$

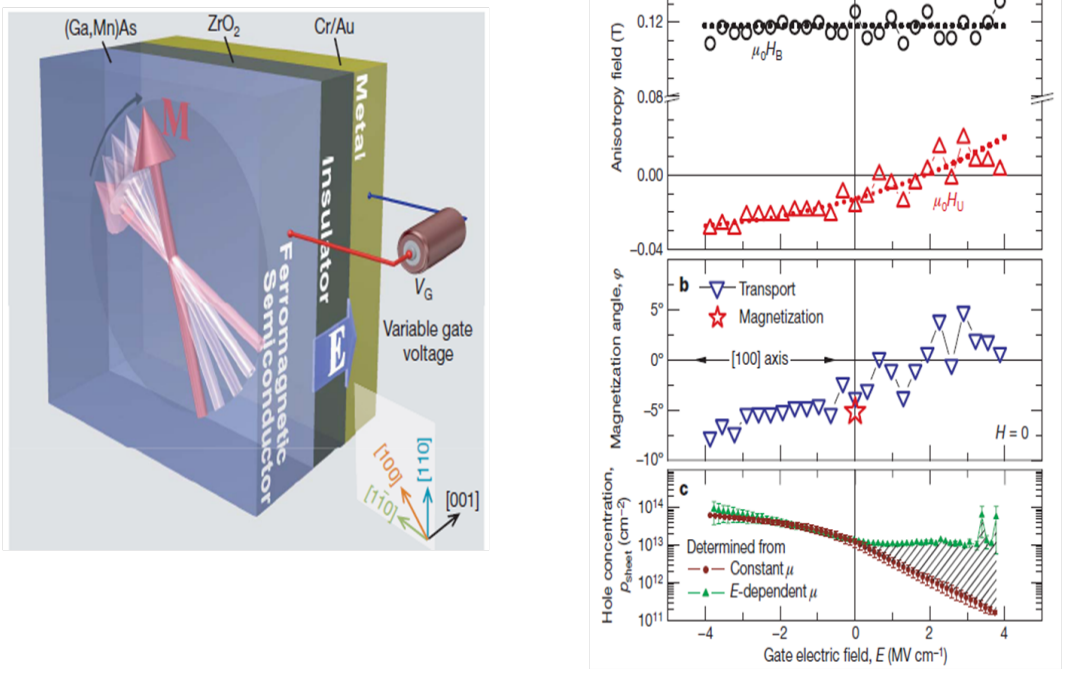

Figure 1.9: (left) The device comprises a metal gate (Cr/Au), an insulating layer (ZrO_2), and a ferromagnetic semiconductor GaMnAs layer. The gate voltage applied between the metal gate and the GaMnAs layer induces an electric field **(E)**, which modifies the hole concentration ,p, in the ferromagnetic semiconductor GaMnAs. The orientation of the magnetization varies as a consequence of the change in the anisotropy constants. (right) **a** Dependence on E of the biaxial($\mu_0 H_B$, open circle) and uni-axial($\mu_0 H_U$,open triangles) anisotropy fields at 2K. **b** The magnetization angle φ at H=0 (triangles) as a function of E, determined from $\mu_0 H_B$ and $\mu_0 H_U$. **c** Dependence on E of the sheet carrier concentration ρ_{sheet}, assuming a constant mobility (filled circles) and an E-dependent mobility (filled triagnles), which give the lower and upper limits of ρ_{sheet}, respectively[23].

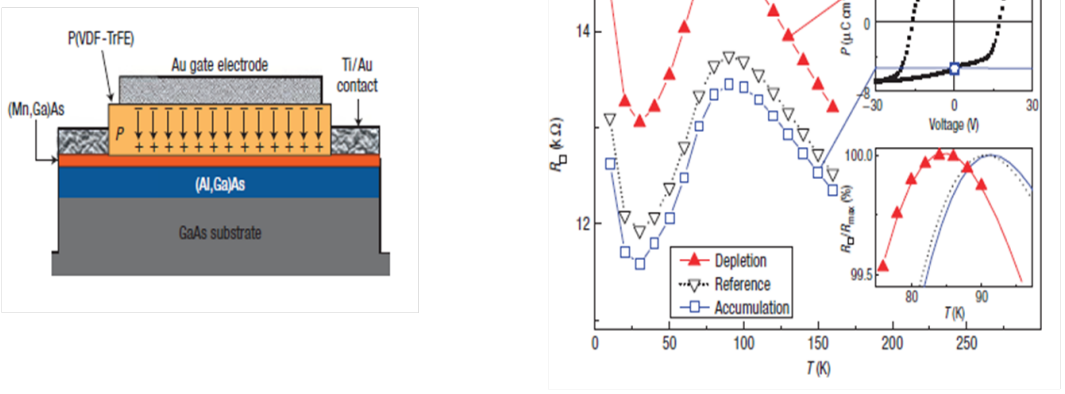

Figure 1.10: (left) A cross-section of the ferroelectric-gate field effect transistor (Fe-FET) structure: the 7 nm Mn-doped layer is separated from the GaAs substrate by a GaAlAs barrier. The top-to-bottom direction of the spontaneous polarization P in the ferroelectric gate corresponds to the depletion state. (right) A polarization reversal in the gate enables a non-volatile switching between accumulation and depletion. Upper and lower inset are the polarization hysteresis loop of the gate driven with 1 kHz triangle pulse and the curves of resistance versus temperature normalized and zoomed in the region around the maximum occurring close to T_c [148].

is the most sensitive parameter to a change of the hole concentration obtained by depletion in a charge space region **E**: the values of the uni-axial anisotropy $\mu_0 H_U$ increases with the electric field **E** and changes sign from negative to positive, whereas the biaxial anisotropy $\mu_0 H_B$ remains almost independent of **E** and the direction of magnetization manipulated by changing **E** (fig.1.9). The variation of the uni-axial anisotropy constant with the hole concentration has been predicted using p-d Zener model Hamiltonian approach [38, 5, 37] and experimentally verified by Khazen thesis [82].

Recently a non volatile control of the ferromagnetism has been demonstrated for hybrid layers composed of a thin $Ga_{1-x}Mn_xAs$ layer with a top ferroelectric gate [148, 129]. The polarization state of the ferroelectric gate leads to an accumulation or depletion of the holes in the underlying $Ga_{1-x}Mn_xAs$ layer near the interface. This significantly modulates the resistivity and the Curie temperature T_c (fig.1.10). The observed small change in T_c is in good agreement with the predicted sub-linear hole concentration dependence T_c(p) [55]. A reduced thickness and even lower low hole concentration in the $Ga_{1-x}Mn_xAs$ layer should allow to amplify this effect.

In a different approach a low-voltage control of the magnetic properties of p-n

junctions with ferromagnetic $Ga_{1-x}Mn_{1-x}As$ being the p-type layer has also been reported [120]. These authors have been able to vary the Curie temperature T_c and Anisotropic Magneto-resistance(AMR) and demonstrated magnetization switching induced by short electric field pulses of a few volts (less than 4V). This concept of the spintronic transistor is distinct from high voltage metal-oxide-semiconductor ferromagnetic field-effect transistors (FETs) [112, 24, 148].

The magnetic properties of ferromagnetic semiconductors can also be controlled by magneto-elastic effects. The magnetization control by strain has been achieved through epitaxial growth. The strain induced by the lattice mismatch between the $Ga_{1-x}Mn_xAs$ layer and substrate has a huge effect on the orientation of the magnetic easy axis [37]. In case of $Ga_{1-x}Mn_xAs$ epitaxial films with typical Mn concentrations of 7 % a GaAs substrate provides compressive strain with an associated in-plane magnetic easy axis whereas an GaInAs substrate gives rise to a tensile strain, leading to perpendicular-to-plane magnetic easy axis. More recently, strain-induced magnetization control by alloying Phosphorous in $Ga_{1-x}Mn_xAs_{1-y}P_y$ has been been investigated [31, 32, 91, 132]. More details are given in chapters 3 and 4. In addition, the control of ferromagnetism with hybrid piezoelectric-ferromagnetic $Ga_{1-x}Mn_xAs$ devices has been demonstrated in [131, 119, 10]. All those results of strain-induced magnetization manipulation have been obtained in the static regime.

For a dynamical control of the magnetization, acoustic surface waves should be one point research for DMS $Ga_{1-x}Mn_xAs$ [159]. The interaction of acoustic waves with magnetic excitations in ferromagnetic, ferrimagnetic or antiferromagnetic solids has been investigated both theoretically and experimentally [87, 4]. The main interaction results from the coupling of acoustic waves (phonons) to spin waves (magnons) through the strain induced modulation of the exchange interaction. It leads to acoustic wave attenuation and velocity variations with both temperature and magnetic field, from which fundamental information can then be derived. Qi et al.[128] have recently been performed standard laser ultrasonic experiments in $Ga_{1-x}Mn_xAs$.

Studies applying ultra-fast (ps) light pulses have also be reported in $Ga_{1-x}Mn_xAs$ [130, 51, 164]. They appear to be a powerful tool to manipulate the magnetization and measure its evolution at very short time scales.

Chapter 2

Experimental techniques

We have used several complementary experimental techniques to investigate the magnetic, transport and structural properties of the samples. Our principal technique is Ferromagnetic Resonance spectroscopy (FMR) but in addition SQUID magnetization measurements were required for the interpretation of the FMR results as well as for the determination of the coercive fields and critical temperatures. Hall-Effect measurements were also performed and showed their importance in the distinction between the different conductivity regimes. X-Ray diffraction measurements allowed us to determine the uniaxial strain in our layers, a fundamental property for the interpretation of the magnetic anisotropy. The Hall-Effect and X-Ray difraction measurements have been performed by the "Laboratoire de Photonique et de Nanostructures" laboratory in Marcoussis. Magneto-optical Kerr spectroscopy was performed on the same samples as those used for FMR by the group of C. Gourdon of our laboratory. For the determination of the absolute phosphorous concentrations in the $Ga_{1-x}Mn_xAs_{1-y}P_y$ samples we have performed Rutherford BackScattering (RBS) experiments with I. Vickridge. In this chapter I present the theoretical background and experimental details of FMR and SQUID spectroscopy the techniques which I have mainly used in this work.

2.1 Superconducting Quantum Interference Device Magnetometry (SQUID)

The SQUID magnetometer (Superconducting Quantum Interference Device) is an extremely sensitive technique well adapted for the measurement of weak magnetizations such as encountered in nm thin layers of DMS materials. It consists of one

or more Josephson junction(s) placed in a vertical magnetic field. This device is a very sensitive instrument for detecting very small changes of the magnetic flux. A Josephson junction is made up of two superconductors separated by an insulating layer. It has unique properties called the DC and AC Josephson effects, based on the tunneling of Cooper pairs through the junction.

In the DC Josephson effect, the current is proportional to the phase difference of the wave functions which can flow through the junction in the absence of a voltage. In the AC Josephson effect, electrons will oscillate with a characteristic frequency. The frequency is proportional to the voltage across the junction [173, 3].

In this thesis we have used a Quantum Design MPMS-DC SQUID magnetometer. This magnetometer can be used in the temperature range 1.8 K to 400 K and in magnetic field of up to 7 Tesla. It measures correctly magnetization down to 10^{-6} emu. The raw signal given by the SQUID [emu] is then normalized on the volume of the magnetic layer to obtain the magnetization in emu/cm^3.

The saturation magnetizations and Curie temperature of all samples were determined from the SQUID measurements. The hysteresis cycle measured for different orientations of the sample relative to the vertical magnetic field gives also access to the magneto-crystalline anisotropy of the samples which can be determined in more detail by the FMR spectroscopy.

In the case of the multi layer structures we have also investigated the exchange bias between two ferromagnetic layers by this technique. The major and minor hysteresis loops can be determined by adequate magnetic field sweeps.

2.2 Ferromagnetic Resonance (FMR) Spectroscopy

The ferromagnetic resonance (FMR) spectroscopy is one of the most powerful techniques to investigate the magnetic properties of ferromagnetic thin films. Associated with SQUID measurements, it can determine important parameters such as the magneto-crystalline anisotropy constants, the Curie temperature, the g-factor, the Gilbert damping factor, the homogeneities of the magnetic layers and the spin stiffness via spin-wave excitation detection. FMR has been also applied with success to the study of exchange bias, ferro and anti-ferromagnetic coupling in metallic or semiconductor multi-layers [29, 110, 42, 43]. In addition, its high sensibility and high resolution allows even the investigation of ultra thin films, such as one monolayer of Fe for example.

FMR spectroscopy is based on the precessional motion of the magnetization in a magnetic field. An applied static magnetic field causes the total magnetic moment to precess around the effective magnetic field H_{eff}. The motion of the magnetization in the presence of a magnetic field is described by the Landau-Lifshitz-Gilbert equation (LLG)[57]:

$$\frac{1}{\gamma}\frac{\partial \vec{M}}{\partial t} = -\left[\vec{M} \times \vec{H_{eff}}\right] + \frac{\alpha}{\gamma M_s}\left(\vec{M} \times \frac{\partial \vec{M}}{\partial t}\right) \tag{2.1}$$

The first term on the right hand represents the precessional torque. The second one, called Gilbert damping term, is phenomenological and is introduced to describe the relaxation process of the magnetization. $\gamma = g\frac{\mu_B}{\hbar}$ is the gyromagnetic ratio where g is the Landé factor (g-factor), H_{eff} is the effective field, sum of the external and internal fields, α is the damping factor and M_s is the saturation magnetization.

Note that, the different contributions of the H_{eff} can be linked to the free energy F of the system:

$$\partial F = \vec{H_{eff}} \,.\partial\, \vec{M} \tag{2.2}$$

The precession of the magnetization is perturbed by a small magnetic field oscillating at a constant frequency, generating the so called resonance phenomenon when this frequency is equal to the Larmor frequency. Considering external magnetic fields of the order of 0.3 T, the frequencies at which this phenomenon appears are of the order of 10^{10} Hz for g factors close to 2. It is the magnetic component of the microwave which is absorbed by the spin system in the resonance conditions. The resonance equation can be obtained by solving the LLG equation.

To determine the resonance field H_{res} we used the free energy approach developed by Smit-Beljers. This approach neglects the damping effect and assumes that the sample is homogeneously magnetized (absence of magnetic domains). The precession of the total magnetic moment with a free energy F occurs at a frequency f=$\omega/2\pi$ given by the Smit-Beljers equation [57, 168]:

$$\left(\frac{\omega}{\gamma}\right)^2 = \frac{1}{M_S^2 sin^2\Theta}\left[\frac{\partial^2 F}{\partial\Theta^2}\frac{\partial^2 F}{\partial\Phi^2} - \left(\frac{\partial^2 F}{\partial\Theta\partial\Phi}\right)^2\right] \tag{2.3}$$

where ω is the angular frequency of the microwave field. The equilibrium position of the magnetization in a steady applied field is obtained from condition that the free energy density first derivatives are zero:

$$F_\theta = \frac{\partial F}{\partial \theta} \mid_{eq} = 0 \tag{2.4}$$

$$F_\phi = \frac{\partial F}{\partial \phi} \mid_{eq} = 0 \tag{2.5}$$

In a standard FMR experiment, the microwave frequency ω_m is kept constant (required by the use of resonant cavities) and the external magnetic field is swept slowly over the field range (0...1.78 T). To increase the sensitivity we superpose a small amplitude oscillating field on the quasi static field in order to allow a phase sensitive detection. Typical values are a 100 kHz modulation with an amplitude of 10 Oe. Under these conditions the resonance spectrum will be the first derivative of a Lorentzian line shape. Computer simulations allow to determine the resonance field and the linewidth with a precision of < 1 Oe. The area under the absorption curve which is obtained by a double integration of the experimental spectrum is proportional to the static magnetization of the sample.

When the magnetic field is oriented along an easy direction of magnetization (i.e. free energy minimum) the H_{res} minimal and when the magnetization is oriented along the hard axis (i.e. free energy maximum) the H_{res} has a maximum value.

2.2.1 The free Energy Density, FMR measurement

The free energy density of the system depends on the respective orientation of the magnetization relative to the crystallographic directions. This is related to the magneto-crystalline anisotropy which depends on the crystal structure of the material and the epitaxy related strains. In this section we discuss the free energy densities for $Ga_{1-x}Mn_xAs$ or $Ga_{1-x}Mn_xAs_{1-y}P_y$ thin films on GaAs.

The magneto-crystalline anisotropy of the $Ga_{1-x}Mn_xAs$ films reflects the anisotropy of the valence band. The spin-orbit coupling splits the six fold degenerate valence band in a upper HH/LH degenerate Γ_8 and a lower Γ_7 band. The exchange interaction will further lift the degeneracy of the HH and LH bands which are the only ones occupied for Mn doping concentrations of some at %. The valence band splitting and the Fermi level position are two essential parameters to determine the contribution of each band (HH and LH) to the magnetic anisotropies. Many experiments have been performed to investigate the relationship of the magnetic anisotropy with the hole density, temperature and strain of the films

For a film of zinc-blende crystal structure such as $Ga_{1-x}Mn_xAs$, the Free Energy

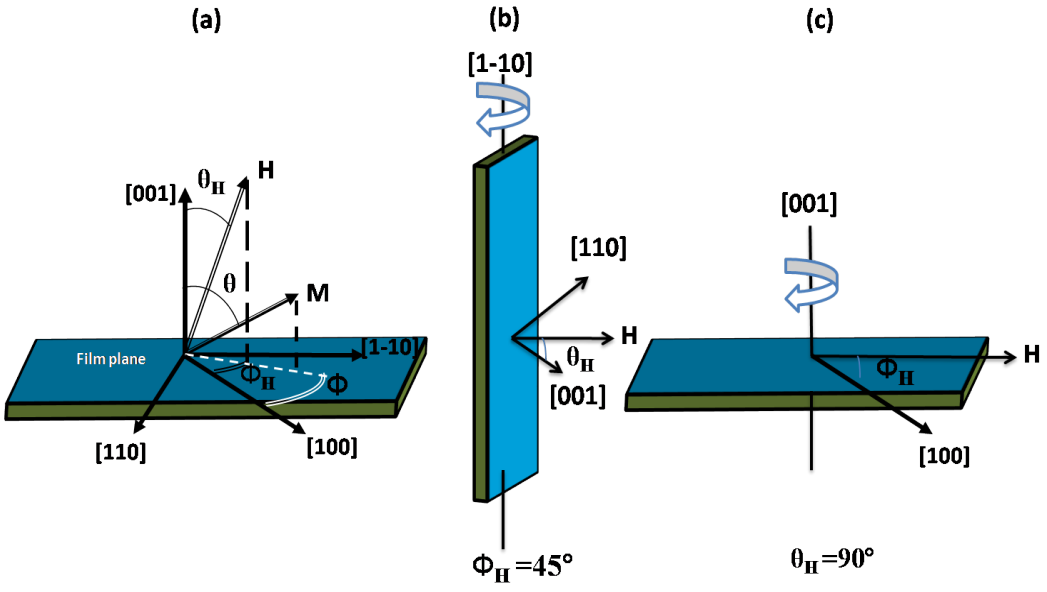

Figure 2.1: (a) Coordinate system of $Ga_{1-x}Mn_xAs$ used in this thesis; the different polar angle (Θ, Φ) and (Θ_H, Φ_H) represent the orientation of the magnetization M and the applied magnetic field H respectively to the film normal. The experimental configuration; (b) out-of plane and (c) in-plane.

density F can be parametrized by second ($H_{2\perp}$,$H_{2\parallel}$) and fourth order ($H_{4\perp}$,$H_{4\parallel}$) anisotropy fields as given here:

$$F = \frac{1}{2}M[-2H[cos\Theta cos\Theta_H + sin\Theta sin\Theta_H cos(\Phi - \Phi_H)] + 4\pi M cos^2\Theta - H_{2\perp}cos^2\Theta$$

$$-\frac{1}{2}H_{4\perp}cos^4\Theta - \frac{1}{2}H_{4\parallel}\frac{1}{4}(3 + cos4\Phi)sin^4\Theta - H_{2\parallel}sin^2\Theta sin^2(\Phi - \tfrac{\pi}{4})] \tag{2.6}$$

The first term in eq.2.6 describes the Zeeman energy; the second term is the demagnetization energy (shape anisotropy); and the last two term represent the magnetic anisotropy energy, where $H_{2\perp}$ and $H_{4\perp}$ are the perpendicular uni-axial and perpendicular cubic anisotropy fields, respectively. $H_{2\parallel}$ and $H_{4\parallel}$ represent the in-plane uni-axial and in-plane cubic anisotropy fields, respectively. The different polar angles represent the respective orientation of the magnetization M(Θ,Φ) and the applied field H(Θ_H,Φ_H); they are defined in fig.2.1(a). The anisotropy field H_i are defined in terms of the magneto-crystalline anisotropy constants K_i as H_i=$2K_i$/M. The perpendicular uni-axial anisotropy $K_{2\perp}$ originates from the lattice mismatch-driven biaxial strain in the $Ga_{1-x}Mn_xAs$ film; it reflects the difference in energy for a magnetization perpendicular to the film plane and in-plane. The sign of $K_{2\perp}$

will be negative for compression and positive for tensile strains. $K_{4\perp}$ and $K_{4\parallel}$ are the cubic anisotropies for [100] and [110] directions. They should of course be equal in the case of a truly cubic system, however the presence of the biaxial distortion induces a slight difference between $K_{4\perp}$ and $K_{4\parallel}$. The in-plane uni-axial anisotropy constant $K_{2\parallel}$ indicates the inequivalence of the [110] and [1-10] directions as observed in numerous cases [154, 161], it is probably due to the influence of the substrate surface reconstruction at the beginning of the growth [171].

In the FMR measurement, we studied systematically two different configurations of the sample: out-of plane configuration (defined in fig. 2.1(b)) and in-plane configuration (defined in fig.2.1(c)). Considering Smit-Beljers (eq. 2.3) and Free energy density (eq. 2.6) the value of the applied field corresponding to the resonance can be written as:

$$\left(\frac{\omega}{\gamma}\right)^2 = \{H_{res}(\Theta_H - \Theta) + \left(-4\pi M + H_{2\perp} + \frac{H_{4\perp}}{2} - \frac{H_{4\parallel}}{4}\right) cos2\theta + \left(\frac{H_{4\perp}}{2} + \frac{H_{4\parallel}}{4}\right) cos4\Theta\}\times$$

$$\{H_{res}cos(\Theta_H - \Theta) + (-4\pi M + H_{2\perp} + \frac{H_{4\parallel}}{2})cos^2\Theta + \left(H_{4\perp} + \frac{H_{4\parallel}}{2}\right) cos^4\Theta - H_{4\parallel} - H_{2\parallel}\}, \tag{2.7}$$

$$\left(\frac{\omega}{\gamma}\right)^2 = \{H_{res}cos(\Phi - \Phi_H) + 4\pi M - H_{2\perp} + H_{4\parallel}\frac{3+cos4\Phi}{4} + H_{2\parallel}sin^2\left(\Phi - \tfrac{\pi}{4}\right)\}\times$$

$$\{H_{res}cos(\Phi - \Phi_H) + H_{4\parallel}cos\left(2\Phi - \frac{\pi}{2}\right)\} \tag{2.8}$$

for the (1-10) plane rotation (out-of plane configuration, i.e. $\Phi = \Phi_H$=45°) and for the (001) plane rotation (in-plane configuration, i.e. $\Theta = \Theta_H$=90°) respectively. In the case where the magnetic field and magnetization are along one of the four high symmetry axes orientation the equations 2.7, 2.8 can be simplified as:

$$\left(\frac{\omega}{\gamma}\right)^2 = \left(H_{res} - 4\pi M + \frac{2K_{2\perp}}{M} + \frac{4K_{2\perp}}{M}\right)\left(H_{res} - 4\pi M + \frac{2K_{2\perp}}{M} + \frac{4K_{2\perp}}{M} - \frac{2K_{2\parallel}}{M}\right) \tag{2.9}$$

$$\left(\frac{\omega}{\gamma}\right)^2 = \left(H_{res} + \frac{2K_{4\parallel}}{M}\right)\left(H_{res} + 4\pi M - \frac{2K_{2\perp}}{M} + \frac{2K_{4\parallel}}{M} + \frac{K_{2\parallel}}{M}\right) \tag{2.10}$$

$$\left(\frac{\omega}{\gamma}\right)^2 = \left(H_{res} - \frac{2K_{4\parallel}}{M} - \frac{2K_{2\parallel}}{M}\right)\left(H_{res} + 4\pi M - \frac{2K_{2\perp}}{M} + \frac{K_{4\parallel}}{M}\right) \tag{2.11}$$

$$\left(\frac{\omega}{\gamma}\right)^2 = \left(H_{res} - \frac{2K_{4\parallel}}{M} + \frac{2K_{2\parallel}}{M}\right)\left(H_{res} + 4\pi M - \frac{2K_{2\perp}}{M} + \frac{K_{4\parallel}}{M} + \frac{2K_{2\parallel}}{M}\right) \quad (2.12)$$

for applied field H $\parallel$ [001], [100], [110] and [1-10] respectively.

The four magneto-crystalline anisotropy constants can be determined from the Smit-Beljers equations from the resonance fields for the four high symmetry directions (equations 2.9-2.12). The knowledge of the value of the saturation magnetization M under the FMR experiment conditions (magnetic field, temperature) is also required. This value was determined by SQUID magnetometry. We have also determined the g-factor in $Ga_{1-x}Mn_xAs$ from the fit of the angular variation of the out-of plane resonance field by eq.2.7. It is generally assumed to be 2.00 but this is not correct due to the contribution from the holes.

For FMR experiments performed at 9.5 GHz frequency with $Ga_{1-x}Mn_xAs$ on GaAs layers, the magnetization of the sample is always saturated at the resonance field in the four high symmetry directions as the coercive fields of $Ga_{1-x}Mn_xAs$ are very small ($<$ 1000 Oe).

2.2.2 Experimental detail of FMR

In the FMR measurements the magnetic sample is glued on a quartz rod and placed at the center of a microwave cavity. We dispose of two microwave bridges of 9.5 GHz (X-Band) and 35 GHz (Q-band) with 200 mW output power. The microwave cavities are rectangular (TE_{102}) and cylindrical (TE_{011}) for the X-Band and Q-Band measurements respectively. For the variable temperature measurements (4K to 300K) the sample is placed a He flow cryostat (X-band) or directly in the a He bath cryostat (Q-band). Fig. 2.2 shows a picture of the FMR set-up used.

The FMR signal is measured by monitoring the microwave energy losses as a function of the external dc magnetic field. The microwave losses are detected by a diode detector. To improve the signal to noise ratio of the experiment, the FMR measurement are performed using a modulation field at 100 kHz and a lock-in detection. Consequently, the measured FMR signal is proportional to the first derivative of the imaginary part of the susceptibility ($d\chi''/H$). The resonance field H_{res} and linewidth Δ H can be determined from the zero crossing of $d\chi''/H$ and the field interval between the extrema of $d\chi''/H$ respectively [71].

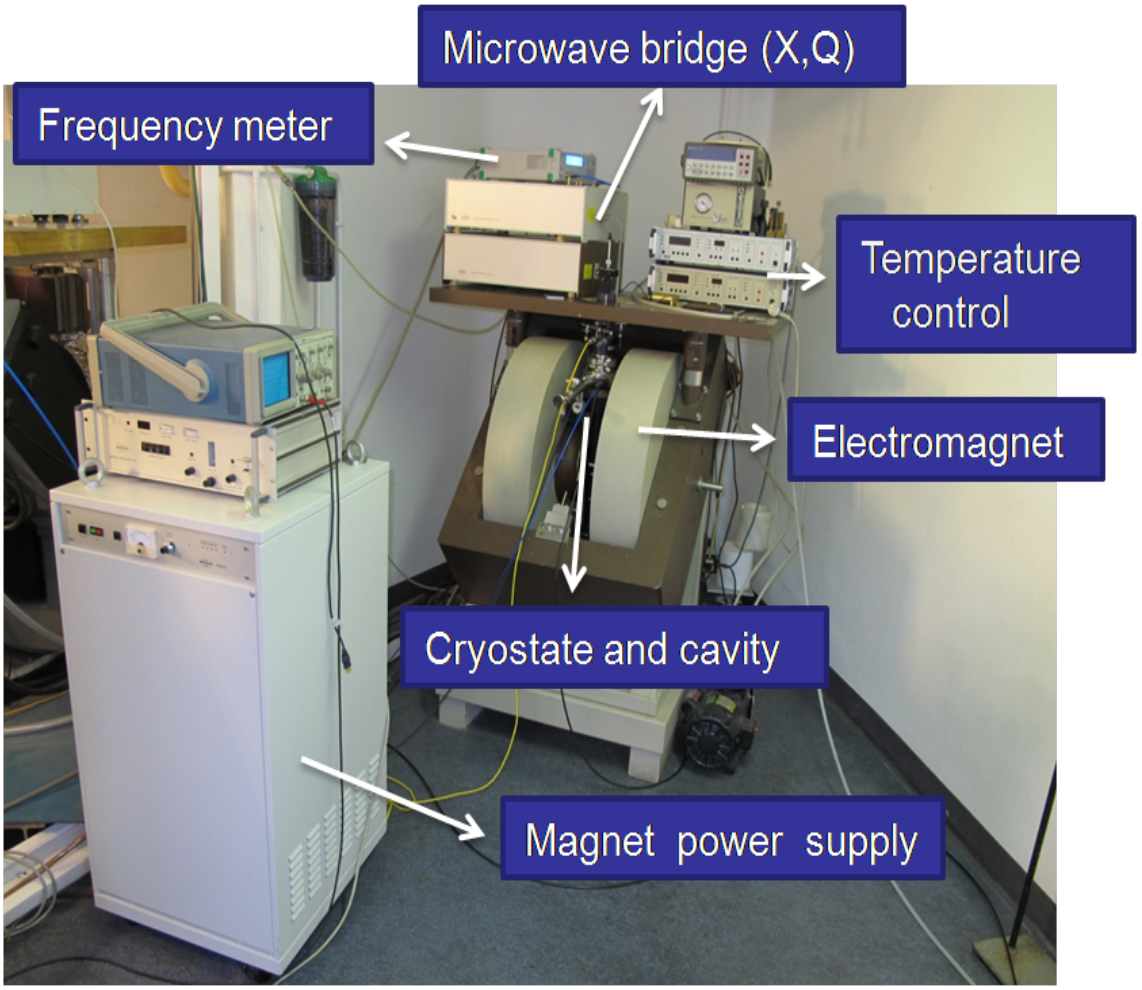

Figure 2.2: The FMR set-up used

Chapter 3

Adjustable Anisotropy in Ferromagnetic $Ga_{1-x}Mn_xAs_{1-y}P_y$

3.1 Introduction

Diluted ferromagnetic (III,Mn)V semiconductors such as $Ga_{1-x}Mn_xAs$ have the unique property that contrary to conventional metallic ferromagnets the shape anisotropy fields are weak as compared to the uni-axial strain induced anisotropy fields. Furthermore, the concentrations of the free carriers, mediating the ferromagnetic interactions, are much lower (in the $10^{20}cm^{-3}$ range) which allows to manipulate them significantly by external perturbations. This gives the opportunity to tailor the ferromagnetism of thin layers to widely different anisotropies.

The change of anisotropy and a reorientation of the magnetization with the strain, densities of carriers and manganese concentration have been satisfactorily modelled by mean field theory by Dietl et al.[37]. Examples of such calculations are shown in fig.3.1.

Due to strain induced by the lattice mismatch between the $Ga_{1-x}Mn_xAs$ epitaxial film and the underlying substrate, anisotropy fields of several kOe are encountered [114, 168, 64, 171]. Generally, $Ga_{1-x}Mn_xAs$ films are grown by low temperature molecular beam epitaxy on GaAs(001) substrates. Mn doping concentrations x>0.05, required to obtain critical temperatures above 120 K, give rise to compressive uni-axial strain both in as-grown and annealed layers. More complex substrate orientations like (311)GaAs [165] have also been investigated. In this case the magnetization has components in the film plane and perpendicular to the plane. By using GaInAs substrates, it is possible to inverse the strain to tensile [64].

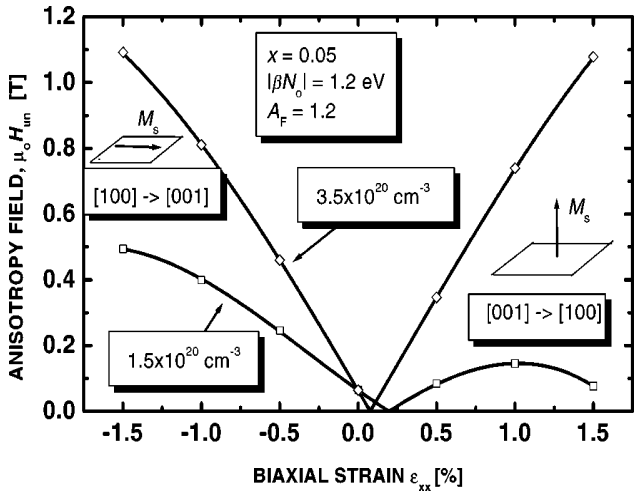

Figure 3.1: The mean field predictions of the anisotropy field H_{un} in $Ga_{1-x}Mn_xAs$ as a function of biaxial strain for two values of the hole concentration. The symbol $[100] \rightarrow [001]$ indicates that the easy axis is along [100], H_{un} is applied along [001][37].

Fig.3.2(a) shows that the uni-axial out-of plane anisotropy field B_{001}=$B_{2\perp}$+B_d for as-grown and annealed samples as a function of the uni-axial strain ϵ_{zz}; its linear variation is in good agreement with the micromagnetic model calculations. The slope depends on the exchange splitting B_G (fig.3.2(b)) and the hole concentration (fig.3.2(c)). However for layers grown on GaInAs buffers, dislocations are created at the InGaAs/GaAs(001)interface, which glide along the plan (111) to emerge on the surface or edge of the layer. This gives rise to important magnetic inhomogeneity and concomitant large linewidths in the FMR spectra.

Recently Stone et al. have shown that it is possible to obtain ferromagnetic $Ga_{1-x}Mn_xAs$ layers also by a different approach: direct ion implantation in a GaAs substrate followed by pulsed laser melting IPLPM [149, 126]. However the structural and magnetic properties of the LT-MBE and IPPLM grown samples are quite different; IPPLM samples are characterized by an intrinsic depth inhomogeneity, residual electrical compensation, inhomogeneous dopant distribution and potentially by second phase inclusions.

For device application it is interesting to control the magnetic anisotropy and create conditions for easy switching of the magnetization by applied electrical or magnetic fields or by spin currents. Various techniques have been proposed to manipulate the anisotropy independently of the Mn doping concentration. Examples are carrier depletion in reverse biased diode structures or by the application of an

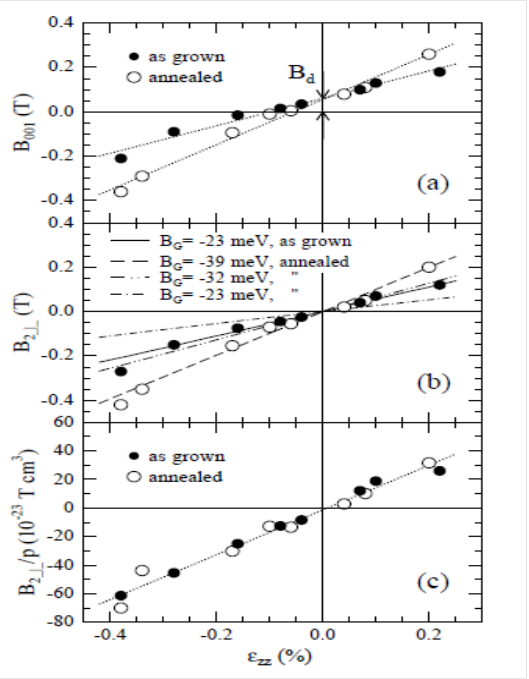

Figure 3.2: (a) Variation of the uni-axial out-of plane anisotropy field B_{001}=$B_{2\perp}$+B_d with the uni-axial strain ϵ_{zz} for as-grown (solid circles) and annealed samples (open circles). The extrinsic parameter $B_d \approx 60$mT is inferred from the intersections between the regression lines (dotted lines) and the vertical axis. (b) Anisotropy field $B_{2\perp}$=B_{001}-B_d show as a function of the ϵ_{zz}. The lines are calculated from the microscopic theory using different exchange splittings B_G and hole densities p. (c) Anisotropy field $B_{2\perp}$ normalised to the hole density p. The linear variation of $B_{2\perp}/p$ with ϵ_{zz} is obtained for both as-grown and annealed samples[64].

external electric field to deplete a channel region[23] or the use of hybride structures composed of $Ga_{1-x}Mn_xAs$ and piezoelectric[118] or ferroelectric top layers[148]. The modifications of the critical temperatures or the magnetization orientation obtained in these conditions are still small. They would be more effective if layers with smaller anisotropy fields and lower carrier concentrations could be engineered. In the following chapter we show that it is possible to overcome this bottleneck by alloying $Ga_{1-x}Mn_xAs$ with phosphorous. First results concerning the growth of $Ga_{1-x}Mn_xAs_{1-y}P_y$ layers have been reported very recently[149, 126, 91, 132]. These quaternary layers should have additional interesting properties. For example, it has been predicted that the Curie temperature will be higher than in similarly Mn doped $Ga_{1-x}Mn_xAs$ films due to the reduced lattice constants of $Ga_{1-x}Mn_xAs_{1-y}P_y$ [102].

In this chapter, we report an extensive study of the strain, electrical and magnetic

properties of LT-MBE grown $Ga_{1-x}Mn_xAs_{1-y}P_y$ quaternary thin films [32, 33] with a Mn concentration of x=0.07 or x=0.104 and different P concentration, ranging from y=0 up to y≈0.19.

3.2 Samples Presentations

Two series of 50-nm $Ga_{1-x}Mn_xAs_{1-y}P_y$ films were grown by LT-MBE on GaAs(001) substrates by Aristîde Lemaître from the LPN laboratory. The growth temperature was set to 250 °C for the magnetic layer growth while the GaAs buffer was grown at 600 °C. The concentration of phosphorous was varied from y=0 to y≈0.19 and the Mn concentration was set to x=0.07 or x=0.104 respectively. During the growth of a series of samples, the Mn cell temperature remains fixed. Only the P cell temperature is varied for each sample of the two series. The Mn and P concentrations were calibrated using Vegard's law, based on the lattice constants of a series of $GaAs_{1-y}P_y$ reference samples grown under the same conditions. After growth, the samples were systematically annealed under N_2 atmosphere at 250°C for 1h [91].

3.2.1 RBS measurements: Determination of the P concentration

In order to check the calibration of the phosphorous concentration and additionally verify the site distribution in these $Ga_{1-x}Mn_xAs_{1-y}P_y$ layers, Rutherford back-scattering (RBS) measurements in random and channelling configurations were performed on the most highly P doped one. For this task we had to choose the sample with the highest P concentration as the quantitative measurement of a element (P) lighter than the lattice atoms (Ga,As) suffers from sensitivity problems. RBS measurements can also provide information on a possible Mn concentration gradient. The distribution between substitutional and interstitial lattice sites can be obtained by channelling RBS. First we have optimized the RBS conditions for the measurement of the total P concentration in random configuration. The RBS spectra were taken with $^4He^+$ particles of 1.8 MeV energy. Care was taken to avoid sample damage under these conditions.

The calibration of the RBS spectrum in absolute units (atoms/cm^2) is obtained from the comparison with a standard sample -Si:Bi in our case- which is measured under identical experimental conditions. The areal density of the Bi atoms which were implanted in the Si wafer are known with 2 % precision [30]; thus one obtains

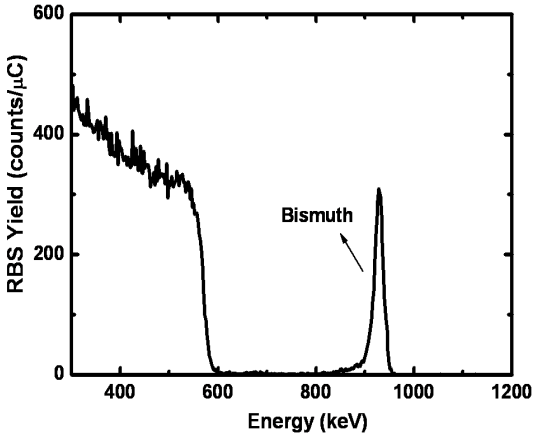

Figure 3.3: Random RBS spectrum of the Si:Bi reference sample with a $^4He^+$ beam of energy of 1.8 MeV, scattering angle of 165°.

for sufficiently high counting statistics a precision of 2 % for the absolute areal concentration of the P atoms and about 1 % precision for their relative fraction [142]. In fig.3.3, we show the RBS spectra from the Bismuth reference sample, measured with 1.8 Mev $^4He^+$ and detected at an angle θ=165°.

The areal density of Phosphorous {P} is given by:

$$\{P\} = \{Bi\}.\frac{D_{Bi}}{D_P}\frac{A_P}{A_{Bi}}\frac{Z_{Bi}^2}{Z_P^2} \tag{3.1}$$

where {Bi} is the areal density of Bi, A_P and A_{Bi} are the area of the P and Bi spectra respectively, Z_{Bi} and Z_P are the atomic numbers of Bismuth and Phosphorous respectively.

The areal density of P deduced from the eq. 3.1 is 18x10^{15} atom/cm^2. Assuming the elemental composition of $Ga_{0.896}Mn_{0.104}As_{1-y}P_y$ layer and the atomic density GaAs (4.5x10^{22}/cm^3), the y value is evaluated to 0.166$\mp$2.0 which is good agreement the value y=0.186 determined from the calibration by Vegard's law.

Note that, in the following chapters we use the P concentration for all samples which we have determined from Vegard's law.

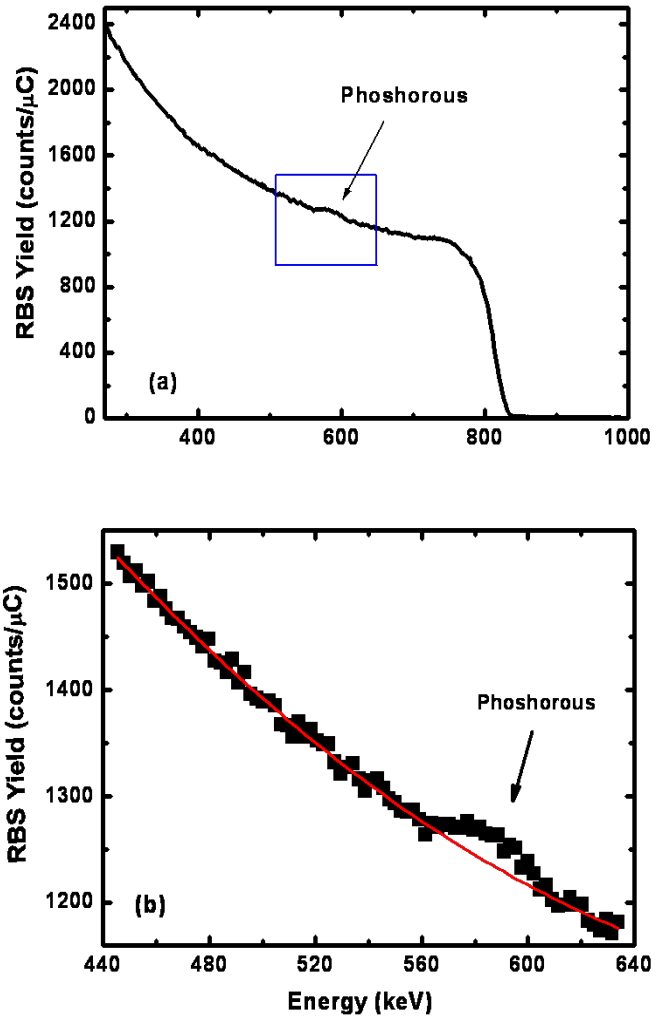

Figure 3.4: (a) Experimental random RBS spectrum obtained from a sample $Ga_{0.896}Mn_{0.104}As_{1-y}P_y$ with a $^4He^+$ beam of energy of 1.8 MeV, scattering angle of 165°. (b) Zoomed in the region around Phosphorous spectra (squares,black) and the polynomial fit (lines,red).

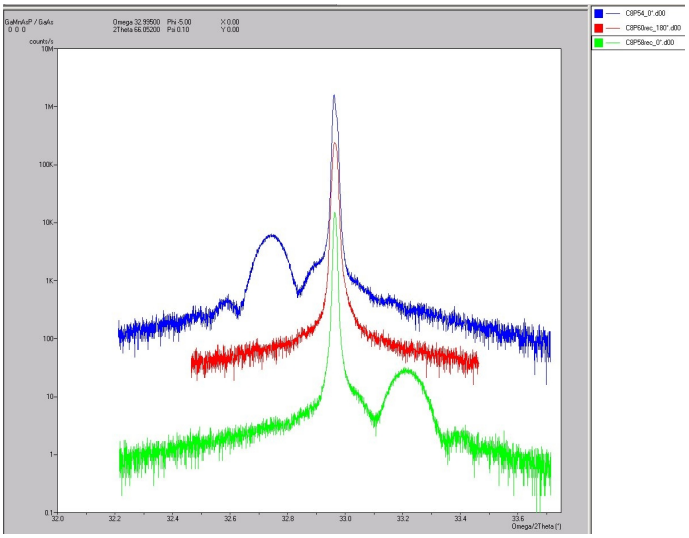

Figure 3.5: High resolution X-ray ω-2Θ curves around the (004) reflexion for $Ga_{0.093}Mn_{0.07}As_{1-y}P_y$ layers with y=0 (blue) y=0.043 (red) and y=0.113 (green).

3.3 Strain measurements by high resolution X-ray diffraction

The uni-axial strain ϵ_{zz} was determined by high resolution X-ray diffraction. The diffraction from the (004) and (002) of planes was used to measure the perpendicular lattice parameter $a_\perp$. The associated uni-axial strain ϵ_{zz} can be calculated from the relation:

$$\epsilon_{zz} = (a_\perp - a_{rel})/a_{rel} \tag{3.2}$$

where the relaxed lattice parameter a_{rel} is obtained from the relation:

$$a_{rel} = \frac{2C_{12}}{C_{11}+2C_{12}}a_\parallel + \frac{C_{11}}{C_{11}+2C_{12}}a_\perp \tag{3.3}$$

C_{11} and C_{12} are the elastic constants of $Ga_{1-x}Mn_xAs_{1-y}P_y$ assumed to be equal to those of GaAs. We used the following value for the ratio of the elastic moduli C_{12}/C_{11}=0.453.

In standard convention, we assume also that the in-plane lattice parameter $a_\parallel$ of the epitaxial layer is equal to the one of the substrate.

The high resolution X-ray rocking curves around the (004) reflection are shown in fig.3.5 for different samples $Ga_{0.093}Mn_{0.07}As_{1-y}P_y$ with y=0 (as-grown), y=0.034 (annealed) and y=0.113 (annealed). The sharp peak at 33.1° corresponds to the diffraction of the GaAs substrate. The $Ga_{0.093}Mn_{0.07}As$ diffraction peak appears at

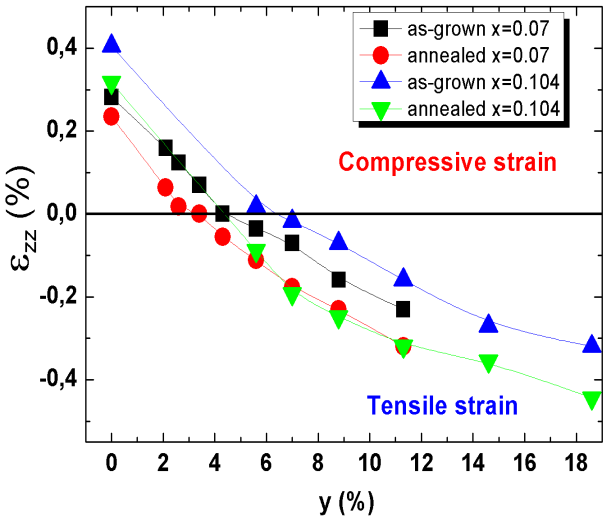

Figure 3.6: Uni-axial strain ϵ_{zz} (symbols) of the $Ga_{1-x}Mn_xAs_{1-y}P_y$ layers plotted as a function the y for as-grown and annealed samples with x=0.07 and x=0.104. The lines are guides for the eyes.

lower angles as compared to the one of GaAs as $a_\perp$ is larger than a_{sub}; this indicates that the $Ga_{0.093}Mn_{0.07}As$ layer is under compressive strain. In this sample ϵ_{zz}=0.3 %. The origin of the lattice mismatch is attributed to the fact that a fraction of the Mn atoms still occupies interstitial lattice sites in spite of the thermal annealing. On the contrary, in the case of $Ga_{0.093}Mn_{0.07}As_{0.887}P_{0.113}$, this peak is located at higher angles, which indicates that the layer is under tensile strain with ϵ_{zz}=- 0.23 %. The diffraction peak of the $Ga_{0.093}Mn_{0.07}As_{0.966}P_{0.034}$ layer is superposed on the GaAs peak which indicates that ϵ_{zz} is close to zero. ϵ_{zz} was measured for all the samples and the results are reported in fig.3.6 as a function of P concentration. The uni-axial strain varies monotonically with P, decreasing from +0.4 % to -0.4 %. This indicates that, in the range of P concentrations that we have chosen, the sign of the uni-axial strain can be controlled continuously or even be made close to zero by adequate P doping. Our results show further that the uni-axial strain for the higher Mn doped (x=0.104) samples is increased relative to the lower Mn doped (x=0.07) one as one would expect. The variation of the lattice constants as a function of Mn concentration has been investigated by Zhao et al.[172] for $Ga_{1-x}Mn_xAs$.

We have also investigated the effect of thermal annealing: as expected the uni-axial strain decreases in the annealed samples due to the partial out diffusion of the Mn interstitials. In the following all results were obtained on annealed samples.

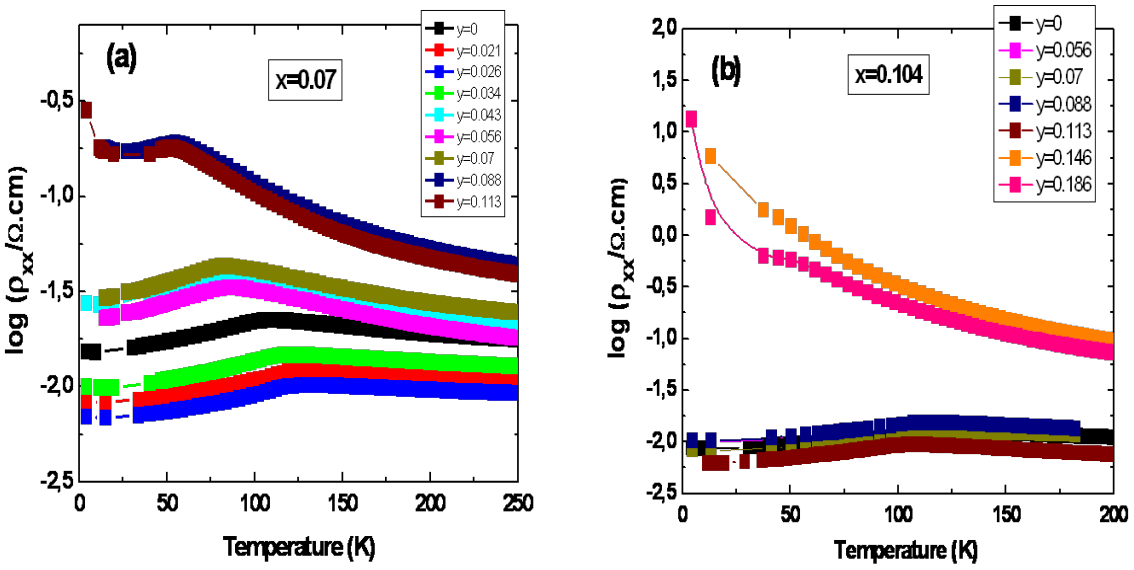

Figure 3.7: The temperature dependence of the resistivity (logarithmic scale) $\log\rho_{xx}$ for $Ga_{0.093}Mn_{0.07}As_{1-y}P_y$ (a) and for $Ga_{0.896}Mn_{0.104}As_{1-y}P_y$ (b) layers as a function of P concentration.

3.4 Transport Measurements

The electrical properties of the layers were determined from Hall effect measurements. The measurement was done in zero magnetic field in the 4 K to 300 K temperature range. Fig. 3.7 shows the evolution of the resistivity of $Ga_{0.093}Mn_{0.07}As_{1-y}P_y$ (a) and $Ga_{0.896}Mn_{0.104}As_{1-y}P_y$ (b) layers. The results are plotted on a logarithmic scale log ρ_{xx} as a function of temperature, for different values of y. For the $Ga_{0.093}Mn_{0.07}As_{1-y}P_y$ layers, the conductivity of the low P doped (y<0.088) is metallic and varies from 0.0007 Ω.cm to 0.003 Ω.cm at low temperature. The resistivity is lower than the one of the $Ga_{0.093}Mn_{0.07}As$ reference sample for y between 0.021 and 0.034 but the resistivity increases for higher P doping (fig.3.7(a)). In the case of $Ga_{0.0896}Mn_{0.104}As_{1-y}P_y$ layers, for y<0.146, the variation of the resistivity with y is similar to the one of the reference sample (fig.3.7(b)) but the resistivity is smaller than the one of $Ga_{0.93}Mn_{0.07}As_{1-y}P_y$ for comparable y value, due to higher carrier densities. These resistivity values are similar to the one's measured for ternary $Ga_{1-x}Mn_xAs$ films and seem not be influenced by the P alloying at least at these P concentrations. This observation is quite different from the one reported by Stone et al.[126] for $Ga_{1-x}Mn_xAs_{1-y}P_y$ layers prepared by ion implantation.

3.4.1 Metallic/Impurity Band Conduction

As the ferromagnetism in these layers is mediated by the hole carriers the conductivity regime is of high importance for the magnetic properties. In fact the issue whether the carriers are free holes in the valence band or carriers in a separated impurity band has been controversially debated for some time now [16, 78]. In $Ga_{1-x}Mn_xAs$ this problem has not really been solved due to controversial interpretation of experimental results of infrared interband absorption measurements. P alloying shines a new light on this issue as different conductivity regimes have been clearly observed depending on the P concentration.

For low P concentrations (y<0.08) the $Ga_{1-x}Mn_xAs_{1-y}P_y$ layers display the well known metallic conductivity behavior with a nearly temperature independent conductivity. However, for high P concentrations: y>0.088 in $Ga_{0.093}Mn_{0.07}As_{1-y}P_y$ and y>0.146 in $Ga_{0.896}Mn_{0.104}As_{1-y}P_y$, we observe a drastic change in the electrical conductivity. The conductivity decreases abruptly at low temperature indicating that the carriers become localized. Such a behavior is expected in the impurity band conduction regime. A critical P concentration for which the conductivity regime should change can be expected for following reasons: the Mn acceptor level becomes increasingly deeper in the band gap with P alloying and the localisation of holes around the Mn acceptors is more important in GaP than in GaAs. Both parameters change continuously with the alloying concentration. We observe also that the transition from metallic to impurity band conduction depends on the Mn dopant concentration. Burch et al.[17] have studied in $Ga_{1-x}Mn_xAs$ the effect of the Mn doping concentration on the impurity band width and the Fermi level E_f position.

To interpret our observation of a thermally activated conductivity in highly P doped layers we have considered two models. In the past such thermally activated conductivity has been interpreted depending on the sample structure (disordered/crystalline) either by the Mott variable range hopping model (VRH) or a simple Arrhenius type model. A VRH model has been previously applied to the case of low doped $Ga_{1-x}Mn_xAs$ layers [144]. In our case the $\rho(T)$ results could not be fitted by the VRH model which predicts a $T^{-1/4}$ variation but are well described by the Arrhenius model which predicts a $exp^{-E_A/kT}$ like variation. The 1/T dependence of the resistivity is reported in fig.3.8(a),(b) at low temperature for the $Ga_{0.093}Mn_{0.07}As_{0.887}P_{0.113}$ and $Ga_{0.896}Mn_{0.104}As_{0.814}P_{0.186}$ samples respectively. We deduced from these plots the following activation energies E_A :

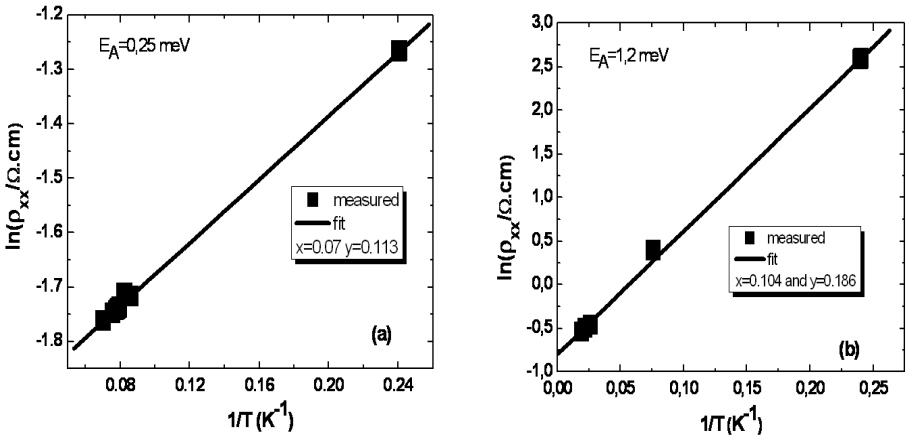

Figure 3.8: The resistivity of $Ga_{0.093}Mn_{0.07}As_{0.887}P_{0.113}$ (a) and $Ga_{0.896}Mn_{0.104}As_{0.814}P_{0.186}$ (b) layer as a function of the inverse of temperature. Solid lines represent fits to the data according to the Arrhenius model.

$$\rho = \rho_0 exp^{-E_A/kT} \tag{3.4}$$

We have determined E_A=0.25 meV and E_A=1.2 meV for the $Ga_{0.093}Mn_{0.07}As_{0.887}P_{0.113}$ and $Ga_{0.896}Mn_{0.104}As_{0.814}P_{0.186}$ samples respectively. Such small activation energies are characteristic for impurity band conduction.

3.4.2 Determination of the Curie temperatures

For all the samples studied, the resistivity vs temperature curves (fig.3.7) present a maximum attributed to the ferromagnetic/paramagnetic phase transition [44, 124]. Near the Curie temperature spatial fluctuations of the spins become more important, leading to a larger carrier scattering and therefore an increase in the resistivity [6]. Whereas previously this maximum has been used to determine the critical temperature, Novak et al.[111] have recently recalled that this is incorrect. The Curie temperature should instead be deduced from the singularity in the dρ/dT curve. In fig. 3.9 we present the Curie temperature of $Ga_{0.093}Mn_{0.07}As_{1-y}P_y$ and $Ga_{0.0896}Mn_{0.104}As_{1-y}P_y$ layers as a function of y, determined from this singularity. For $Ga_{0.093}Mn_{0.07}As_{1-y}P_y$ layers the Curie temperature first increases from 92 K to 116 K when y increases up to 0.021 and then it decreases slightly with increasing y in the metallic regime. We consider these slight variations as non systematic as standard, constant annealing conditions have been applied. For y=0.13, the low

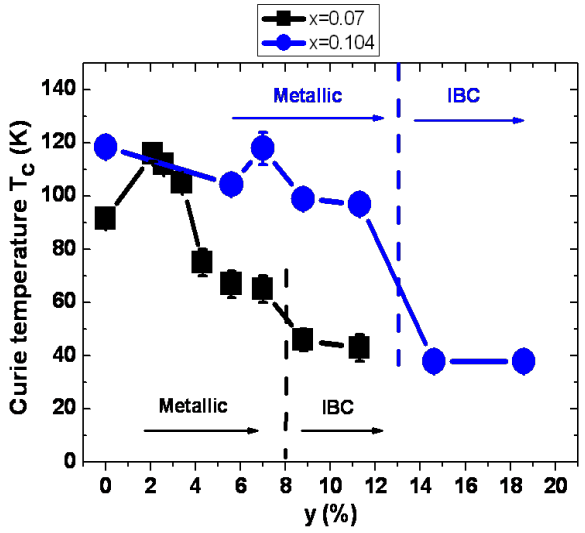

Figure 3.9: Dependence of Curie temperature T_c on y, obtained from the maximum of dρ/dT for $Ga_{0.093}Mn_{0.07}As_{1-y}P_y$ (squares,black) and $Ga_{0.896}Mn_{0.104}As_{1-y}P_y$ (circles, blue). The dashed line represents the value of y for which the metallic/IBC transition occurs for $Ga_{0.93}Mn_{0.07}As_{1-y}P_y$ (black) and $Ga_{0.896}Mn_{0.104}As_{1-y}P_y$ (blue).

temperature behaviour of the conductivity changes drastically as the impurity band conduction regime is reached. In samples which display this behaviour the critical temperature changes abruptly: for y>0.13 the critical temperature decreases to 43 K. For $Ga_{0.896}Mn_{0.104}As_{1-y}P_y$ layers the Curie temperature which varies only slightly between 118 K and 100 K in samples with the metallic conductivity regime it decreases again abruptly to T<40K for the one's with a thermally activated low temperature conductivity regime (y>0.12). The dashed lines in the figures indicate the phosphorous concentration for which the conduction regimes change.

3.4.3 Hall effect measurements and hysteresis cycles

Fig.3.10(a) presents hysteresis cycles obtained from Hall effect measurements for $Ga_{0.093}Mn_{0.07}As_{1-y}P_y$ layers with different values of y for an applied magnetic field oriented parallel to the [001] axis. For low P doped samples the [001] axis is a hard axis for magnetization. However, for higher P doping (y>0.07) the hysteresis cycles become square shaped and the easy axis is now parallel to [001]. With increasing temperature the coercive field decreases due to an increase of the thermal fluctuations (fig.3.10(b)). We have also studied the hysteresis cycle for

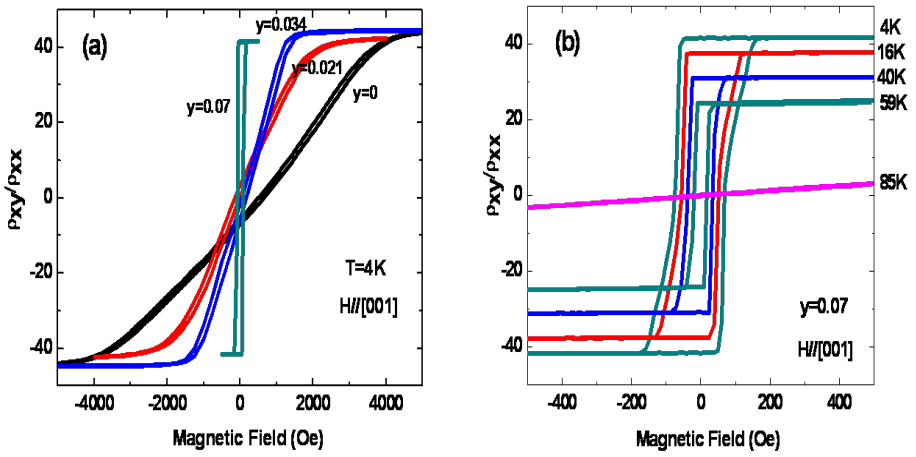

Figure 3.10: (a) Hysteresis cycles at 4K were obtained from Hall effect measurements, with the magnetic field applied perpendicular to the $Ga_{0.093}Mn_{0.07}As_{1-y}P_y$ layers for different values of y. (b) Hysteresis cycle at several temperatures for sample with y=0.07.

$Ga_{0.896}Mn_{0.104}As_{1-y}P_y$ layers and the results are similar to the one discussed above.

3.5 SQUID Magnetization measurement

The magnetization of the samples was measured by a superconducting quantum interference device (SQUID). In fig. 3.11, we show the temperature dependence of the magnetization for $Ga_{0.093}Mn_{0.07}As_{1-y}P_y$ (a) and $Ga_{0.0896}Mn_{0.104}As_{1-y}P_y$ (b) layers. They were measured with an applied field of H=1000 Oe oriented along the easy axis direction. The saturation magnetization of ≈40 and ≈52 emu/cm^3 correspond to an effective Mn concentrations of x_{eff}=0.04 and x_{eff}=0.05 for $Ga_{0.093}Mn_{0.07}As_{1-y}P_y$ and $Ga_{0.0896}Mn_{0.104}As_{1-y}P_y$ layers respectively. As already observed in the Hall measurements, a transition from the metallic to impurity band type conduction results in a reduction of the saturation magnetization which decreases to 36 emu/cm^3. The Curie temperatures were also deduced from the magnetization curves by the determination of the temperature where the slope of the M(T) curve changes sign (fig.3.11(d)). Theses values are in good agreement with the ones determined by the transport measurements (fig.3.9).

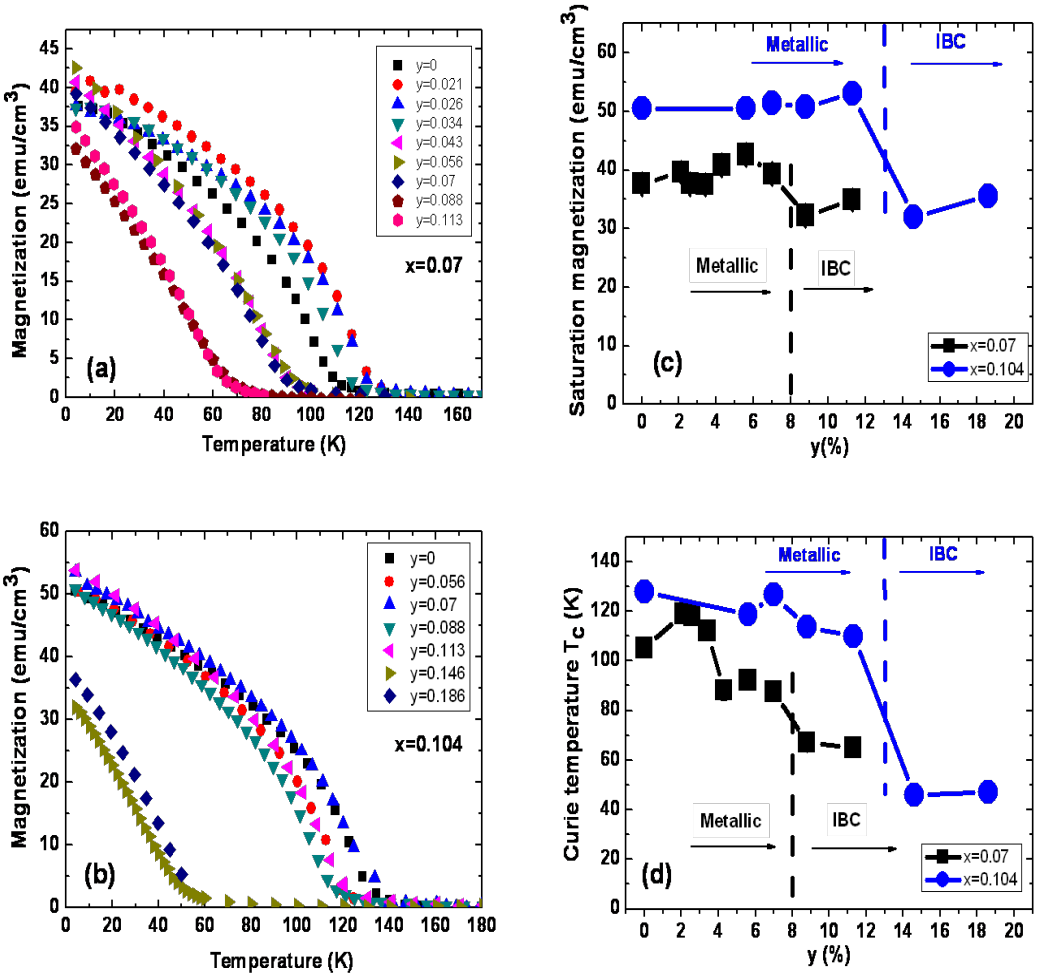

Figure 3.11: Magnetization as a function of temperature for $Ga_{0.093}Mn_{0.07}As_{1-y}P_y$ (a) and $Ga_{0.09}Mn_{0.10}As_{1-y}P_y$(b) layers with an applied field of 1000 Oe, oriented parallel to the easy axes. For all samples, the easy axes were determined by FMR measurements. The dependence of the saturation magnetization (c) and Curie temperature (d) as a function of y. The dashed lines represent the range of y in which the metallic/IBC occurs for $Ga_{0.093}Mn_{0.07}As_{1-y}P_y$ (black) and $Ga_{0.896}Mn_{0.104}As_{1-y}P_y$ (blue). The lines are guides for the eyes.

3.5.1 Critical exponent of the magnetization curve and intrinsically limited Curie temperatures

The critical temperature T_c of $Ga_{1-x}Mn_xAs$ layers is according to the mean-field model [77] given by:

$$T_c = \frac{N_{Mn}S(S+1)}{3k_B} \cdot \frac{J_{pd}^2 \chi_f}{(g\mu_B)^2} \tag{3.5}$$

where N_{Mn} is the Mn density, J_{pd} the p-d exchange integral, χ_f is the free carrier susceptibility. For a concentration of x=0.05 it predicts a critical temperature of 120 K which is in good agreement with the experimental results. Different groups [111, 22, 101] have successfully grown higher doped layers with x up to 0.20 in order to obtain higher critical temperatures. However, the Curie temperature of these layers did not increase proportionally with the doping but stated in all cases below 180 K. In fact, the highest critical temperature has been observed by Novak et al. [111]: T_c=180 K for a sample with a total Mn concentration of x=0.120. As the effective Mn concentration in all these highly doped $Ga_{1-x}Mn_xAs$ layers remained limited at x<0.07 they are not suited to test these mean field predictions in which of course the effective and not the total Mn doping level should be used. The effective doping level can be obtained from the value of the saturation magnetization. Khazen et al.[85] have shown very recently that the analysis of the critical exponents of the magnetization in the temperature range close to the Curie temperature might provide a clue for an intrinsic limitation of the Curie temperature which is not included in the mean field model. Within this model a critical exponent of β=0.5 would be expected. The observation of a lower value of 0.40 is in agreement with the theoretical predictions that the critical behaviour of such ferromagnets should belong to the class of universality of 3D Heisenberg systems with a critical exponent of 0.38 [61]. The slight enhancement is characteristic of disordered ferromagnets like $(Fe_{O.4}Ni_{0.6})_{75}\ P_{16}B_6Al_3$ where β=0.40 [9, 170].

In the spirit of this paper we have analysed also some of our $Ga_{1-x}Mn_xAs_{1-y}P_y$ layers. The magnetization M(T) curves of the samples $Ga_{0.896}Mn_{0.104}As_{1-y}P_y$ with y=0, y=0.113 and y=0.186 measured at zero applied magnetic field after saturation along the easy axis are shown in fig.3.12(a). The effective Mn concentration determined from M_s at T=4K are x_{eff}=0.05 and x_{eff}=0.036 for $Ga_{0.896}Mn_{0.104}As_{1-y}P_y$ with y=0, y=0.113 and y=0.186 respectively. Note that the sample with y=0.118 is not metallic but in the impurity band conduction regime. The Curie temperatures are 121 K, 106 K and 44 K respectively. The magnetization M(T) in the critical

regime (below T_c) is proportional to t^β, where t=(1-T/T_c) is the reduced temperature. We show in fig.3.12(b) logM(T) as a function of log(t). We determined the Ginzburg temperature: t_g=0.12, t_g=0.15 and t_g=0.2 for the $Ga_{0.896}Mn_{0.104}As_{1-y}P_y$ samples with y=0, y=0.113 and y=0.186 respectively. The critical exponents have been determined β=0.40, β=0.39 and β=0.5 for $Ga_{0.896}Mn_{0.104}As_{1-y}P_y$ with y=0, y=0.113 and y=0.186 respectively. For the samples in the metallic regime, we obtain values close to those obtained by Khazen et al.[85] for highly doped $Ga_{1-x}Mn_xAs$ layers with an effective Mn concentration of x=0.10 whereas the sample with thermally activated conductivity shows the value expected from the mean field model. A value of β intermediate between the mean-field exponent and that of the 3D Heisenberg model has been linked to the short range of the ferromagnetic interactions.

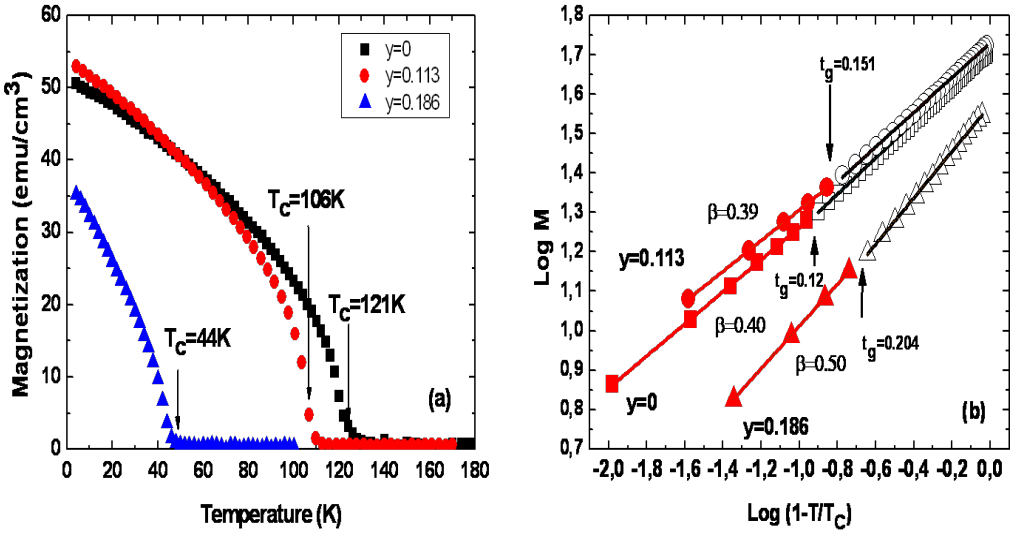

Figure 3.12: (a) Magnetization curves M(T) of the samples $Ga_{0.896}Mn_{0.104}As_{1-y}P_y$ with y=0, y=0.113 and y=0.186 at zero applied magnetic field after saturation along the easy axis. (b) Magnetization as a function of the reduced temperature t plotted in logarithmic scale. The red line corresponds to the best fit of the experimental data with the critical exponent β.

3.5.2 Coercitivity determined from SQUID measurements

The magnetization curves of the $Ga_{0.093}Mn_{0.07}As_{0.0974}P_{0.026}$ layer as a function of applied field and different temperatures are shown in fig.3.13 (a) for the H||[100]. The magnetization for the magnetic field parallel to the easy axis presents a square

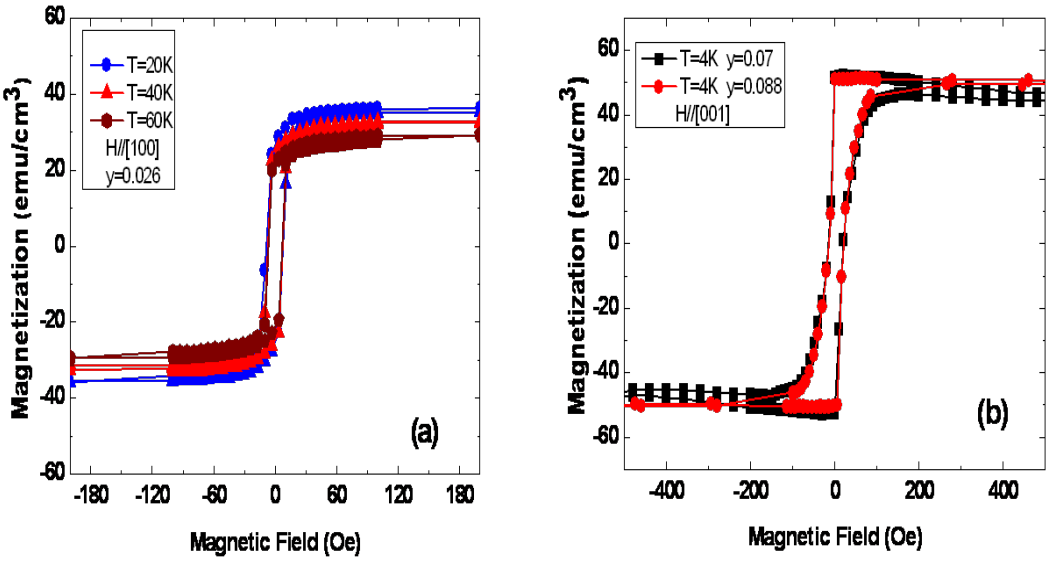

Figure 3.13: (a) $Ga_{0.093}Mn_{0.07}As_{0.0974}P_{0.06}$ sample magnetization as a function of applied field parallel to the [100] axis for several temperatures. (b) Magnetization at T=4K of $Ga_{0.09}Mn_{0.10}As_{1-y}P_y$ layers with y=0.07 (black) and y=0.08(red) as a function of applied field parallel to [001] direction.

shaped hysteresis cycle with a coercive field of $\approx$ 7 Oe in agreement with the results shown in fig.3.10(a). However for the $Ga_{0.896}Mn_{0.104}As_{1-y}P_y$ layers with y=0.07 and y=0.088 we observe square hysteresis cycles with a coercive field of $\approx$15 Oe when the applied field is oriented along the direction perpendicular to the film plane(fig.3.13 (b)).

3.6 FMR study of $Ga_{1-x}Mn_xAs_{1-y}P_y$ layers with different P concentrations

In this section, we will present the results of the FMR measurements for the two series of $Ga_{1-x}Mn_xAs_{1-y}P_y$ samples. We will also present results for samples in the impurity band conduction regime. The FMR measurements were performed with a standard X-band spectrometer with a 9 Ghz microwave source and first derivative detection. The angular dependence of the FMR spectra were measured rotating the static magnetic field in two crystallographic planes: (110) and (001) named "out-of plane" and "in-plane configuration" respectively. These two sets of angular

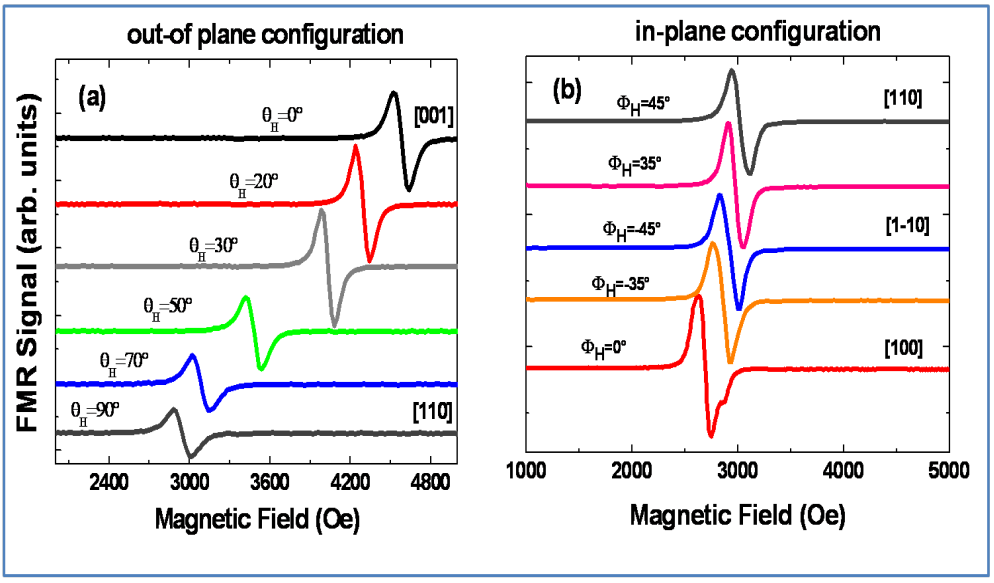

Figure 3.14: Typical FMR spectra at 4K of $Ga_{0.093}Mn_{0.07}As_{0.966}P_{0.034}$ sample for an out-of plane and in-plane variation of the applied field.

variations of the resonance fields enable us to determine the anisotropy constants and the Landé g-factor in a standard procedure [168].

3.6.1 FMR spectra

In fig.3.14, we show typical low temperature (T=4K) FMR spectra of the $Ga_{0.093}Mn_{0.07}As_{0.966}P_{0.034}$ layer for out-of plane and in-plane orientations. The FMR spectra indicate an easy axis along H||[100] with a minimum resonance field at H=2928 Oe and a hard axis along the [001] direction with a highest field at H=4581 Oe. These easy/hard axes orientations are in good agreement with the SQUID and transport measurements. In this case the films are compressively strained. The small line-width of the FMR spectra of about 100 Oe for [001] demonstrates a high magnetic homogeneity of this sample. In the following the variation of the linewidth with the P concentration will be discussed in more detail.

The FMR spectra for all samples were measured as a function of temperature between 4K up to the Curie temperature. The evolution of the hard axes FMR spectra for $Ga_{0.093}Mn_{0.07}As_{0.966}P_{0.034}$ as a function temperature are shown in fig.3.15. We observe a monotonous shift of the resonance field with increasing temperature. This reflects the well known temperature dependence of the anisotropy constants. We observe a change in the orientation of the easy axis from [100] for T<80K to [1-

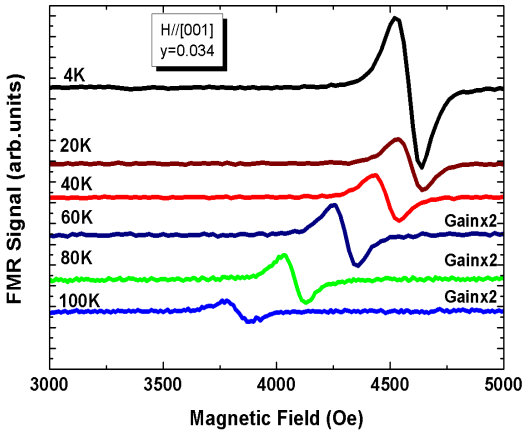

Figure 3.15: FMR spectra of the $Ga_{0.093}Mn_{0.07}As_{0.966}P_{0.034}$ as a function of temperature for H||[001] direction

10] for T≈100K. From the variation of the intensity of the FMR spectrum with the temperature, the Curie temperature can equally be estimated; the value found, close to 125 K, is slightly higher than the value determined from transport and SQUID measurements. We attribute this increase in the apparent Curie temperature to the non zero value of the applied magnetic field required for FMR measurements.

In figs.3.16(a)-(b), we present the spectra obtained for $Ga_{0.093}Mn_{0.07}As_{0.93}P_{0.07}$ and $Ga_{0.896}Mn_{0.104}As_{0.93}P_{0.07}$ samples respectively in the out-of plane and in-plane configurations for the four high symmetry orientations at 4K. For y=0.07, the spectra present clearly an easy axis along [001] and a hard axis along the [110]. On the other hand, for higher concentration of P (y>0.07) we observe an easy axis of magnetization along [001] i.e., perpendicular to the film plane. The spectra for H||[001] and [100] directions are composed of one main resonance line and additional resonances of lower intensity. The resonances with the highest intensity at ≈ 2440 Oe and 3160 Oe correspond to the FMR uniform mode of this film for H||[001] and H||[100] respectively.

In fig.3.17, we present the FMR spectra for the four high symmetry orientations at 4K (a) and 40K (b) for sample $Ga_{0.896}Mn_{0.104}As_{0.882}P_{0.118}$. This sample is in the impurity band conductivity regime. Due to the high P doping level the easy axis is perpendicular to the film plane. As compared to the samples with metallic conduction the line-widths are increased.

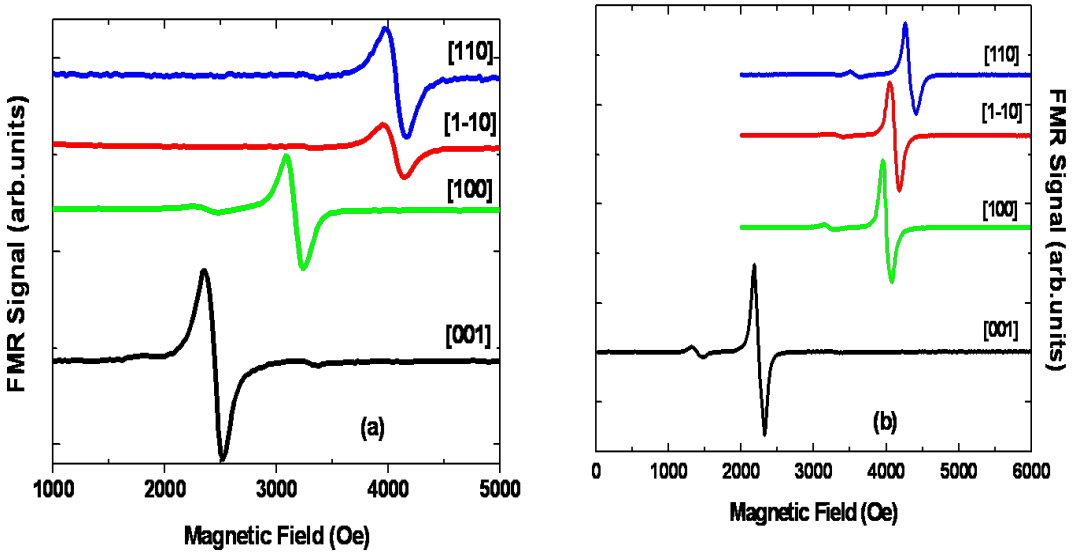

Figure 3.16: FMR spectra at 4K of $Ga_{0.93}Mn_{0.07}As_{0.93}P_{0.07}$(a) and $Ga_{0.896}Mn_{0.104}As_{0.93}P_{0.07}$(b) for four high symmetry axes.

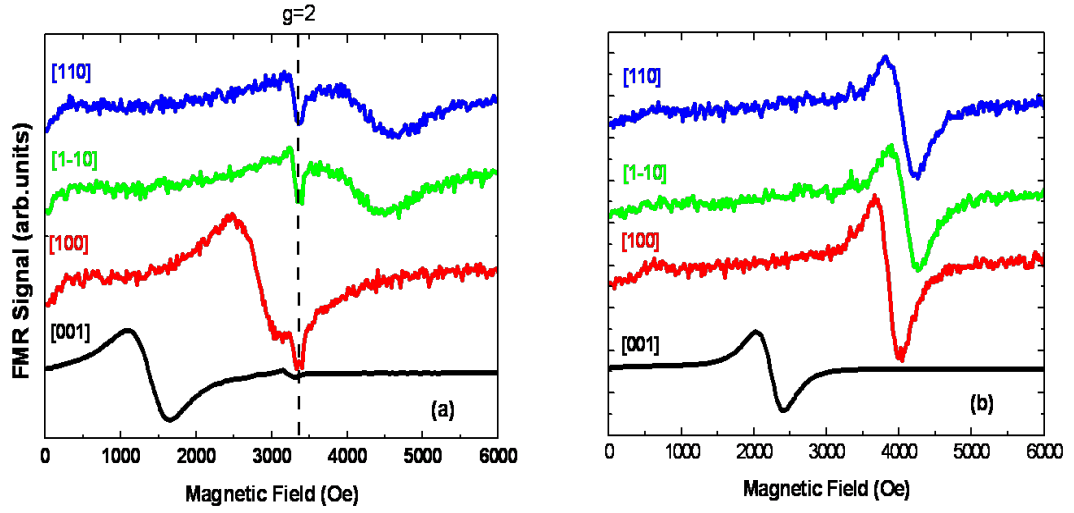

Figure 3.17: FMR spectra at 4K(a) and 40K(b) of $Ga_{0.896}Mn_{0.104}As_{0.882}P_{0.118}$ for four high symmetry axes.

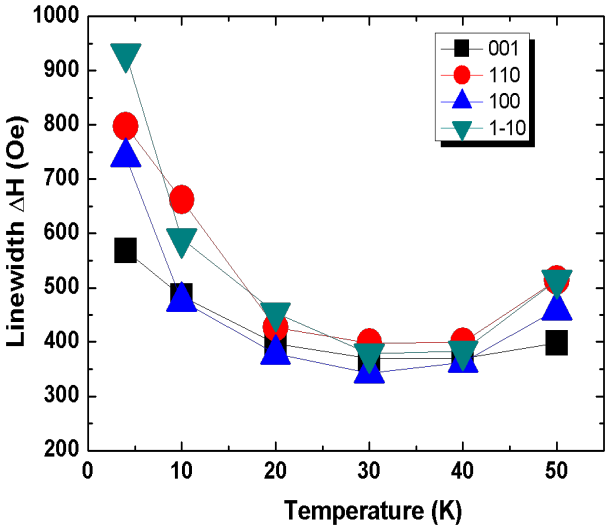

Figure 3.18: FMR linewidth (symbols) of $Ga_{0.896}Mn_{0.104}As_{0.882}P_{0.118}$ as a function of temperature for the four high symmetry orientations of the applied field. The lines are guides for the eyes

.

3.6.2 FMR linewidth

We have observed in this series of samples that the FMR linewidth depend on the P concentration, the orientation of the applied field and the temperature. In fig. 3.18, we show the temperature variation of the linewidth for sample $Ga_{0.896}Mn_{0.104}As_{0.882}P_{0.118}$ which is in the impurity band conduction regime. The linewidths are approximately isotropic at temperatures close to T_c but increase strongly at low temperature up to 1000 Oe with significant anisotropy.

The linewidth at 4K as a function P concentration are shown in fig.3.19. We observe a dramatic increase of the linewidth in the IBC regime. The linewidth of the uniform mode FMR spectra depends on multiple parameters such as the damping factor, the magnetic inhomogeneities and the hole concentration[83, 84]. It is not possible in this case to separate the different contributions.

3.6.3 Magnetocrystalline anisotropy constants

In figs. 3.20 and 3.21, we show the experimental angular variations of the resonance fields of $Ga_{0.093}Mn_{0.07}As_{1-y}P_y$ and $Ga_{0.896}Mn_{0.104}As_{1-y}P_y$ layers respectively and their simulation with the Smit-Beljers equation. The simulation parameters

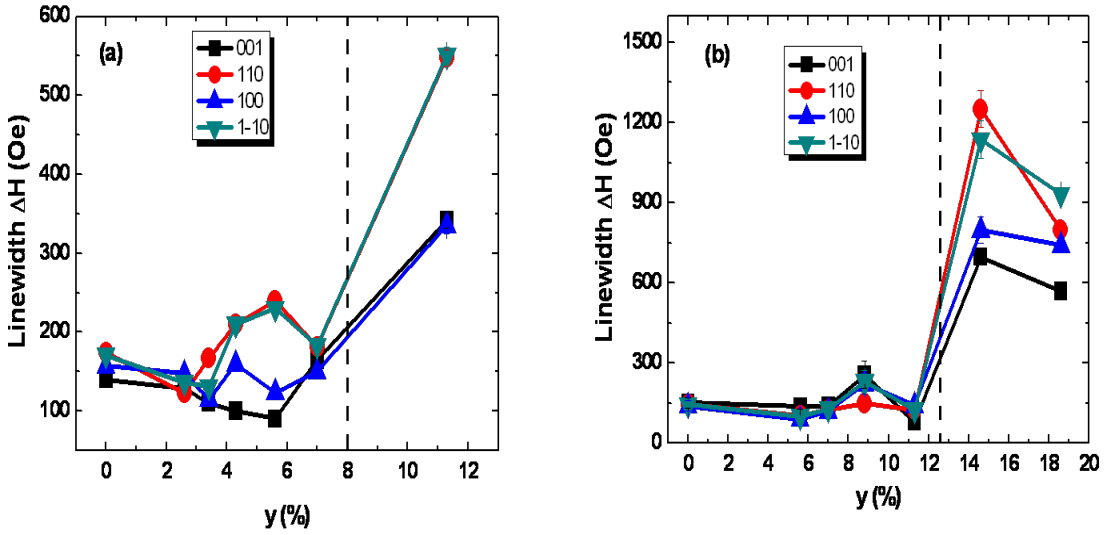

Figure 3.19: FMR linewidth for $Ga_{0.093}Mn_{0.07}As_{1-y}P_y$(a) and $Ga_{0.896}Mn_{0.104}As_{1-y}P_y$(b) layers at 4K as a function of the y for four orientations of the applied field. The lines are a guide for the eyes. The dashed line represents the range of y in which the metallic/IBC transition occurs for $Ga_{0.093}Mn_{0.07}As_{1-y}P_y$ and $Ga_{0.896}Mn_{0.104}As_{1-y}P_y$ layers.

are the four magnetic anisotropy constants, the static magnetization M and the effective g-factor. We obtain a good agreement between the measured resonance fields and the simulated ones. We see that the P alloying allows to engineer in-plane or out-of-plane configurations for the easy axis of magnetization. For the $Ga_{0.093}Mn_{0.07}As_{1-y}P_y$ layers with y=0, the resonance fields are very anisotropic with values of 8000 Oe and 1600 Oe for H$\|$[001] and H$\|$[100] respectively but with increasing P alloying is reduced and finally reversed.

The four magnetic anisotropy constants $K_{2\perp}$, $K_{2\|}$,$K_{4\perp}$ and $K_{4\|}$ which describe the biaxial and cubic anisotropies have been obtained by solving the resonance equations for the four high symmetry orientations of the applied magnetic field taking into account the minimization of the free energy for the equilibrium states of the magnetization. It was shown previously that the dominant anisotropy constant for $Ga_{1-x}Mn_xAs$ layers on GaAs or GaInAs substrates with typical Mn concentrations of x=0.07 is $K_{2\perp}$; it is proportional to the uni-axial strain induced by the lattice mismatch [168]. In fig.3.22 and 3.23, we show the magnetic anisotropy constants as a function of temperature for the samples $Ga_{0.093}Mn_{0.07}As_{1-y}P_y$ and $Ga_{0.896}Mn_{0.104}As_{1-y}P_y$. Callen et al.[18] have calculated the temperature depen-

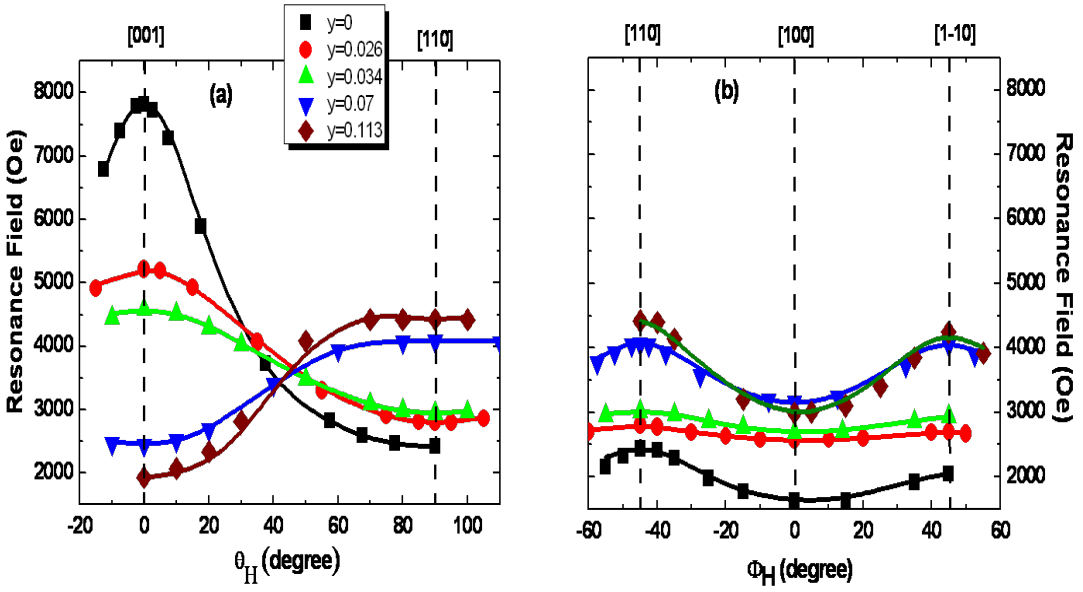

Figure 3.20: Angular dependence of the FMR resonance fields at 4K (symbols) and the simulated angular variations (lines) out-of plane configuration(a) and in-plane configuration(b) for $Ga_{0.093}Mn_{0.07}As_{1-y}P_y$ samples with variable y.

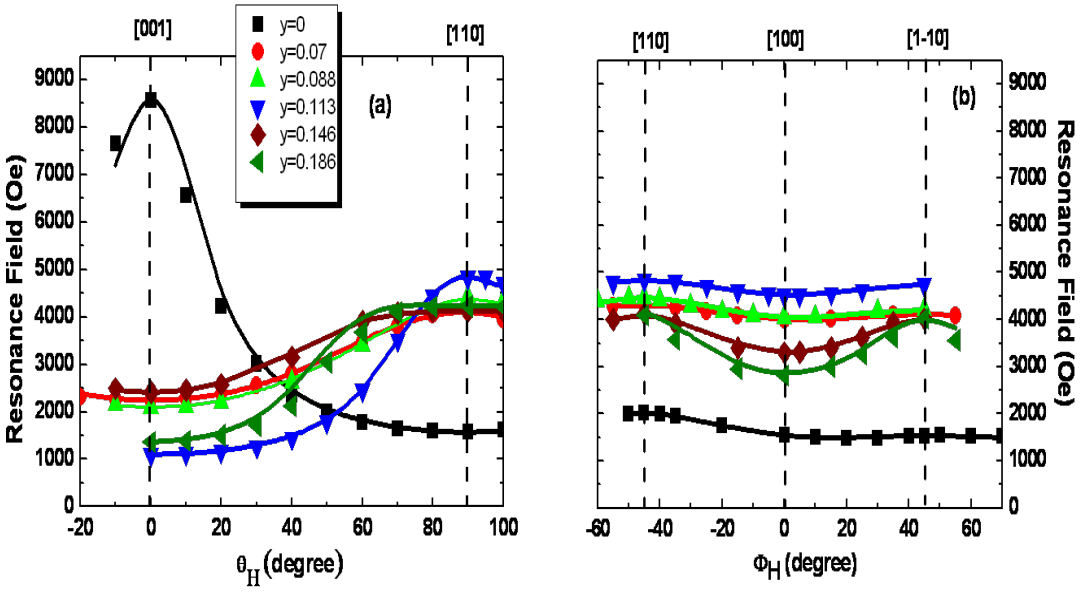

Figure 3.21: Angular dependence of the FMR resonance field (squares) and the simulated angular variation (lines) out-of plane configuration(a) and in-plane configuration(b) for $Ga_{0.896}Mn_{0.104}As_{1-y}P_y$ samples with variable y

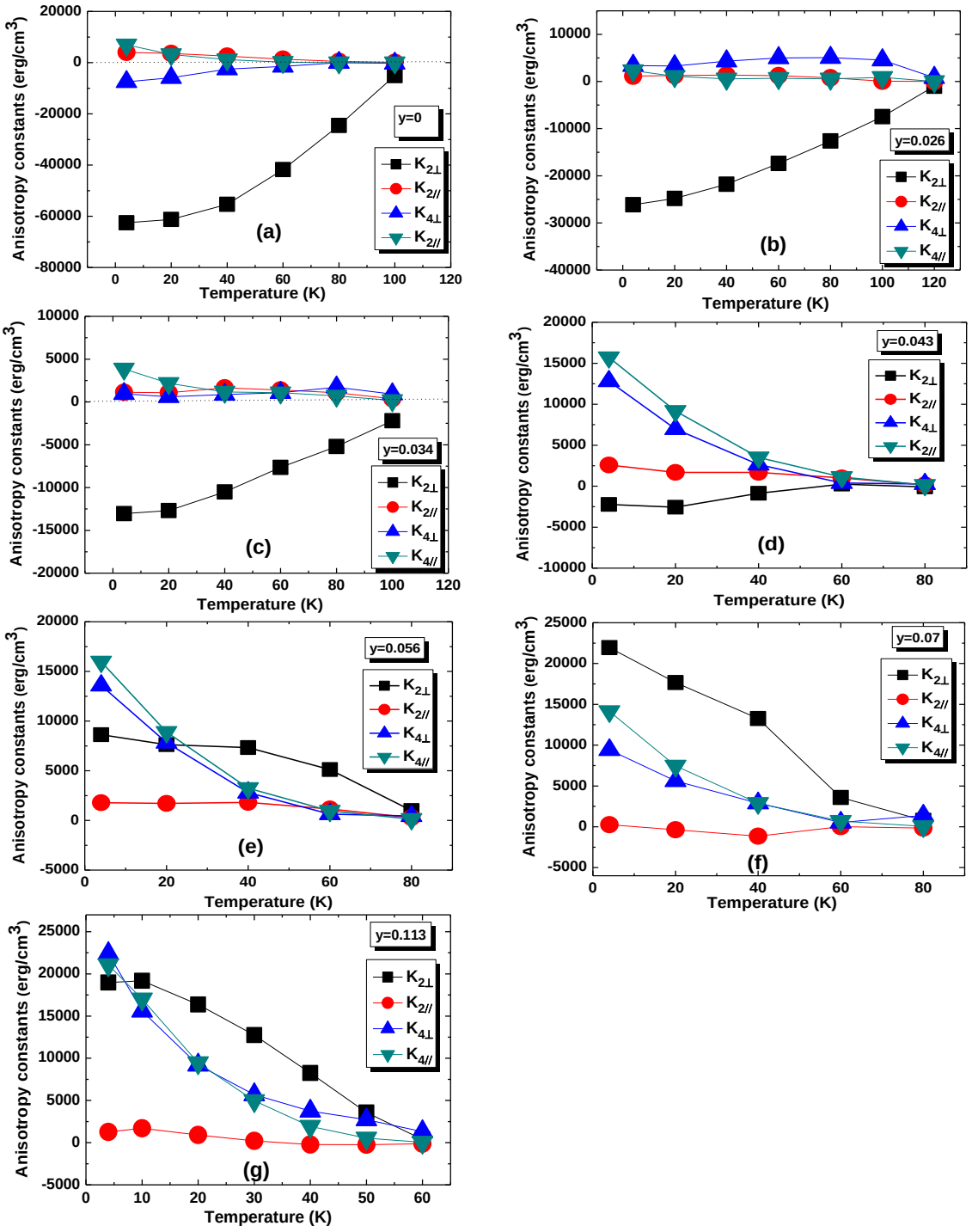

Figure 3.22: Variation of the four magnetocrystalline anisotropy constants $K_{2\perp}$(black), $K_{2\parallel}$ (red), $K_{4\perp}$ (bleu) and $K_{4\parallel}$ (green) (symbols) as a function of temperature for the $Ga_{0.093}Mn_{0.07}As_{1-y}P_y$ y=0 (a), y=0.026 (b), y=0.034 (c), y=0.043 (d), y=0.0.056 (e), y=0.07 (f) and y=0.113 (g). Symbols: experimental results, lines are guide for the eyes.

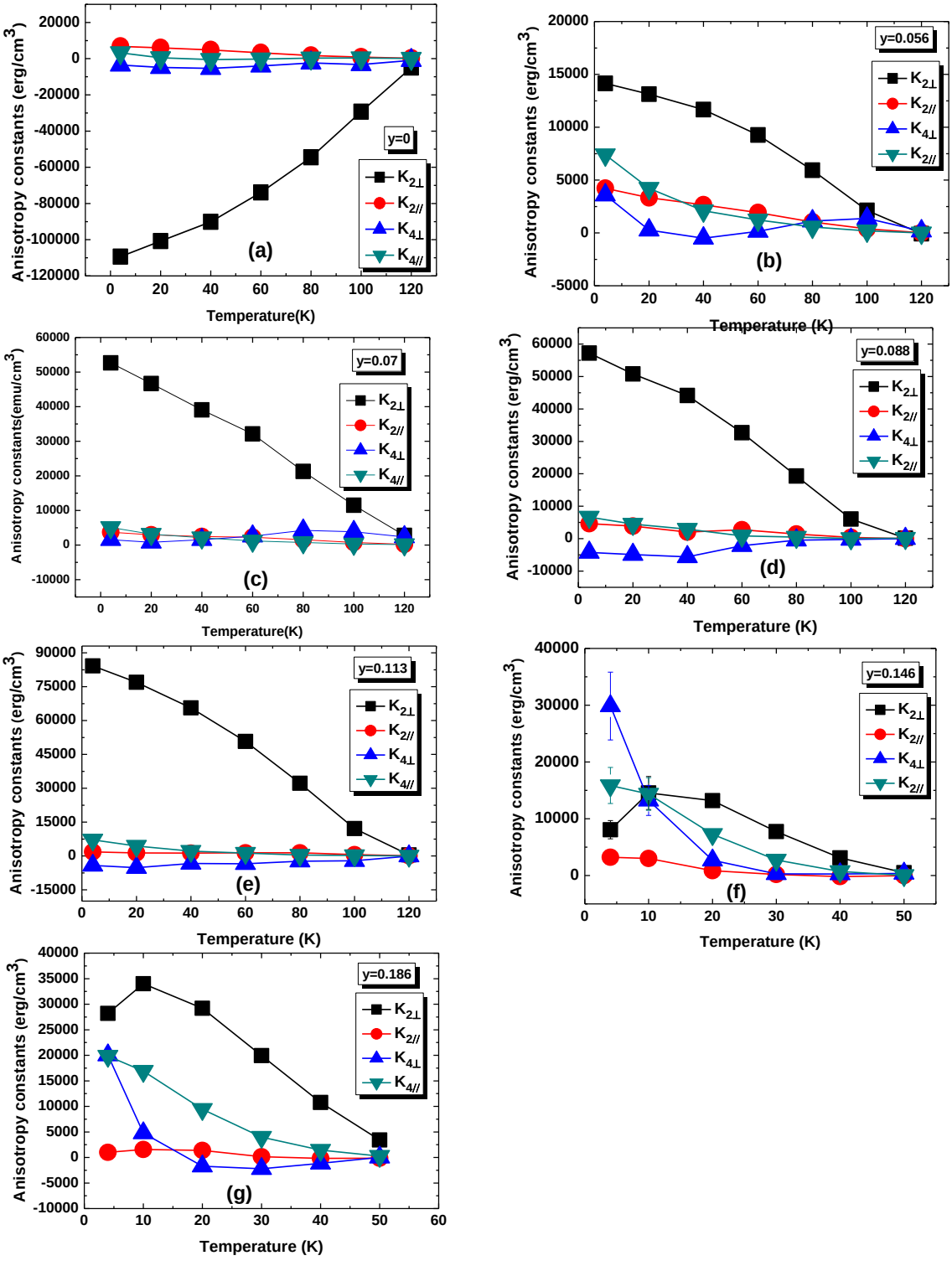

Figure 3.23: Variation of the four magnetocrystalline anisotropy constants $K_{2\perp}$ (black), $K_{2\parallel}$ (red), $K_{4\perp}$ (bleu) and $K_{4\parallel}$ (green) (symbols) as a function of temperature for the $Ga_{0.896}Mn_{0.104}As_{1-y}P_y$ y=0 (a), y=0.056 (b), y=0.007 (c), y=0.088 (d) y=0.113 (e), y=0.146 (f) and y=0.186 (g). Symbols: experimental results, lines are guide for the eyes.

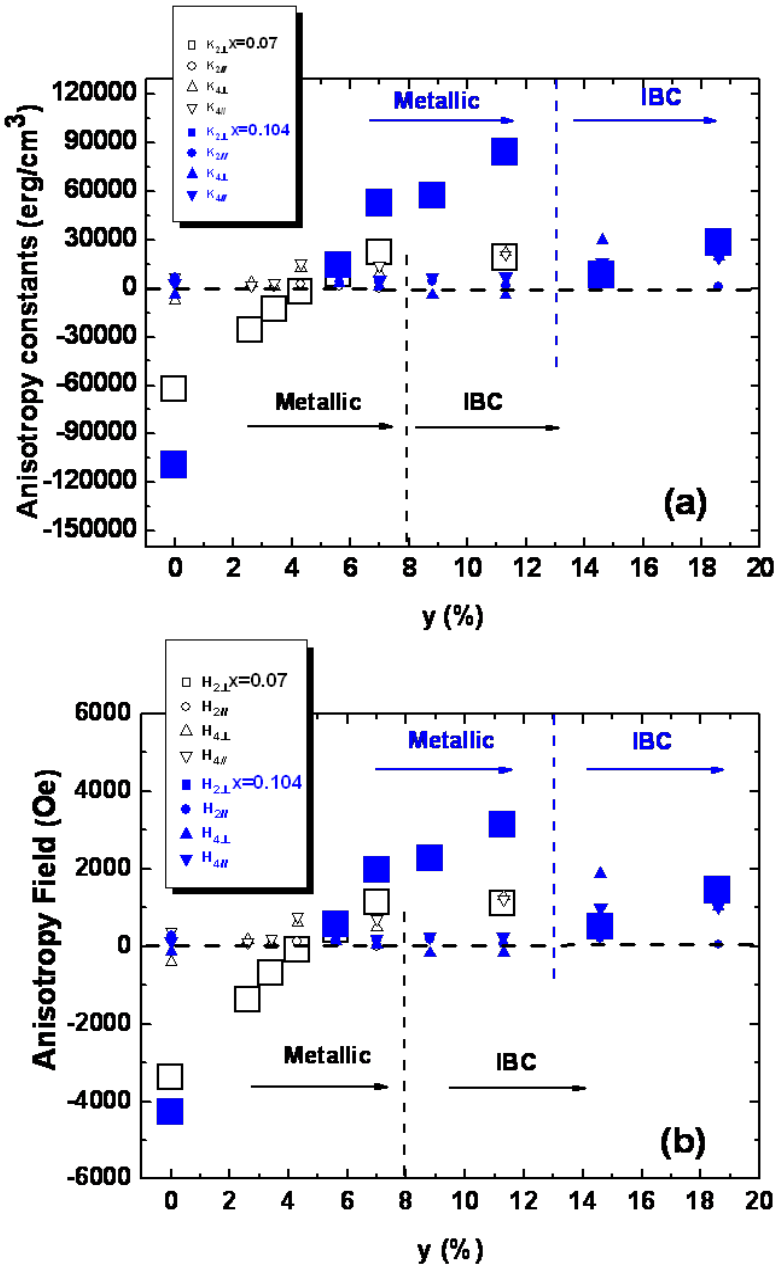

Figure 3.24: Variation of the magnetocrystalline anisotropy constants (K_i) (a) and the magnetic anisotropy fields $2K_i/M$ (b) at 4K as a function of y. The dashed lines represent the value of y for which the metallic/IBC transition occurs for $Ga_{0.093}Mn_{0.07}As_{1-y}P_y$ (black) and $Ga_{0.09}Mn_{0.10}As_{1-y}P_y$ (blue) layers.

dence of the magnetocrytalline anisotropy constants at low and high temperature; this behaviour was studied in more detail by Khazen et al. [83]. For the y=0 sample, the $K_{2\perp}$ constants at T=4K has a negative value of -6.10^4 erg/cm^3 and -11.10^4 erg/cm^3 for x=0.07, x=0.104 respectively; with increasing P doping level its value increases monotonously and passes though zero for y=0.056. In this range of phosphorous concentration the four anisotropy constants are small and of comparable numerical values. With further increase in y, $K_{2\perp}$ becomes positive and the easy axis of magnetization switches to out-of plane. The other three constants do not vary with y. For high P concentrations: y>0.088 and y>0.113 for $Ga_{0.093}Mn_{0.07}As_{1-y}P_y$, $Ga_{0.896}Mn_{0.104}As_{1-y}P_y$ respectively, we observe a drastic reduction of the $K_{2\perp}$ anisotropy constants.

In fig.3.24 we show the four anisotropy constants (a) and anisotropy fields $2K_i/M$ (b) as a function of phosphorous concentration. To correct the numerical values of the anisotropy constants for the slightly different magnetization values of the samples we have normalized their value for a constant M. The samples differ in the magnetization values as the Mn incorporation is influenced by the P alloying.

3.6.4 Comparison to mean field predictions

In the framework of the mean field model [37] of ferromagnetism in zinc-blende diluted magnetic semiconductor, the value of the constant $K_{2\perp}$ normalized to a constant hole concentration, is expected to vary linearly with the strain. In previous works, both theoretical and experimental studies confirmed that $K_{2\perp}$ constant depends linearly on the carrier concentration and the uni-axial strain [83, 64]. Fig. 3.25 (a) shows the values of the magnetic anisotropy constant $K_{2\perp}$ at 4K for both series $Ga_{0.093}Mn_{0.07}As_{1-y}P_y$ and $Ga_{0.0896}Mn_{0.104}As_{1-y}P_y$ layers as a function of the uniaxial strain ε_{zz}. In the metallic conduction regime for both layers a linear dependence on ε_{zz} is evidenced. However we observe a drastic reduction of the $K_{2\perp}$ anisotropy constant when entering in the impurity band conduction (IBC) regime. Assuming that the mobility is similar for the samples in the metallic state we then expect a linear variation of the anisotropy constant $K_{2\perp}$ normalized to a constant hole concentration with the uni-axial strain. Indeed, this is observed in the fig.3.25(b). In this figure the anisotropy constant $K_{2\perp}$ at 4K and its normalized value ($K_{2\perp}.\rho_{xx}$) are plotted as a function of the uni-axial deformation ε_{zz}. The linear variation is in good agreement with the mean field model prediction, as previously found in the case of $Ga_{1-x}Mn_xAs$ [83]. The experimental data can be fitted by the following

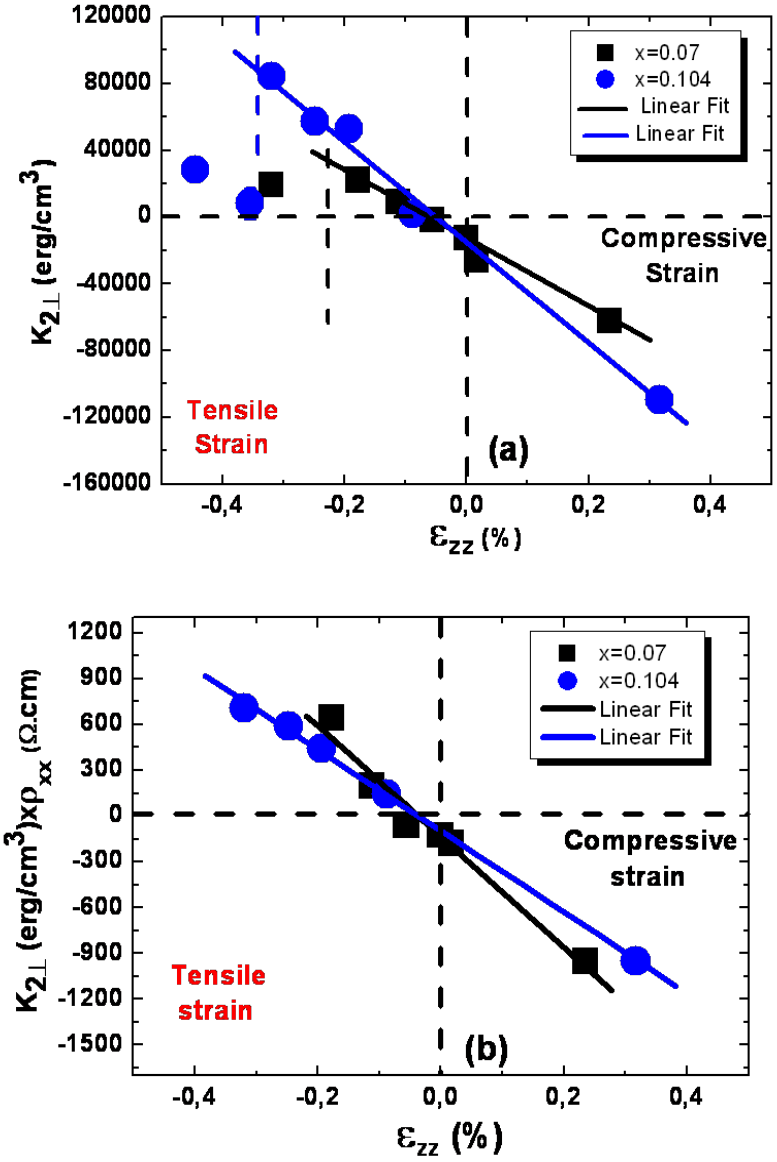

Figure 3.25: The magnetic anisotropy constant $K_{2\perp}$ at 4K for $Ga_{0.093}Mn_{0.07}As_{1-y}P_y$ (squares,black) and $Ga_{0.0896}Mn_{0.104}As_{1-y}P_y$ (circle, blue) before (a) and after normalization (b) for a constant hole concentration as a function of strain ε_{zz}. The dashed lines represent the range of y in which the metallic/IBC transition occurs for $Ga_{0.093}Mn_{0.07}As_{1-y}P_y$ (black) and $Ga_{0.896}Mn_{0.104}As_{1-y}P_y$ (blue). Solid lines represent fits to the data according (eq.3.6). Errors bars for the anisotropy constants are estimated to <5 % which is below the size of the symbols.

expression:

$$\frac{K_{2\perp}}{p} = C.\varepsilon_{zz} \tag{3.6}$$

where p is hole concentration and C is a prefactor.

We show also that the prefactor depends on the Mn and hole concentrations. Glunk et al.(fig.3.2) have shown that for $Ga_{1-x}Mn_xAs$ layers deposited on GaInAs/GaAs(001) partially relaxed buffer layers with different In concentration, $K_{2\perp}(\varepsilon_{zz})$ is strongly influenced by the hole concentration and the exchange-splitting parameter B_G. The exchange splitting parameter is defined as:

$$B_G = \frac{A_F \beta M}{6 g \mu_B} \tag{3.7}$$

where A_F is the Fermi liquid parameter, β the p-d exchange integral, M magnetization, g Landé factor and μ_B the Bohr magneton. It can be seen in fig.3.25 that the linear fit of these results does not pass through the origin. Whereas such a behaviour would have been expected for the total perpendicular anisotropy field due to the contribution of the demagnetization field, this is not the case for the $H_{2\perp}$ defined by $2K_\perp/M$. We attribute this small deviation to the fact that the samples have slightly different values of the exchange splitting parameters due to the alloying which will scatter the corresponding $K_{2\perp}$ values [64].

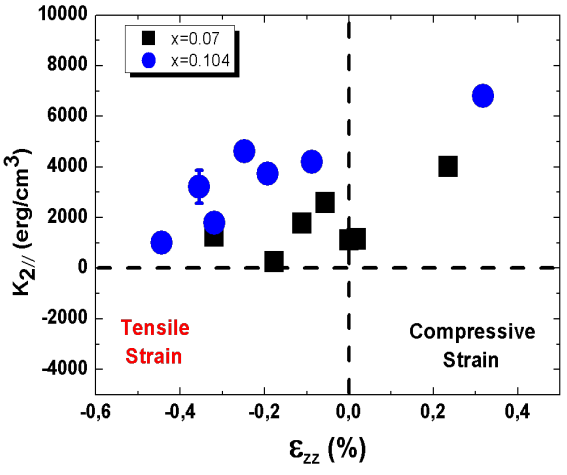

Figure 3.26: The uni-axial in-plane anisotropy $K_{2\|}$ at 4K dependence on ε_{zz} for $Ga_{0.093}Mn_{0.07}As_{1-y}P_y$ (squares, black) and $Ga_{0.896}Mn_{0.104}As_{1-y}P_y$ (circle, blue)

In fig.3.26, we show that the uni-axial in-plane anisotropy constant $K_{2\|}$ varies between 1000 and 4000 erg/cm^3, 1000 and 7000 erg/cm^3 for $Ga_{0.093}Mn_{0.07}As_{1-y}P_y$

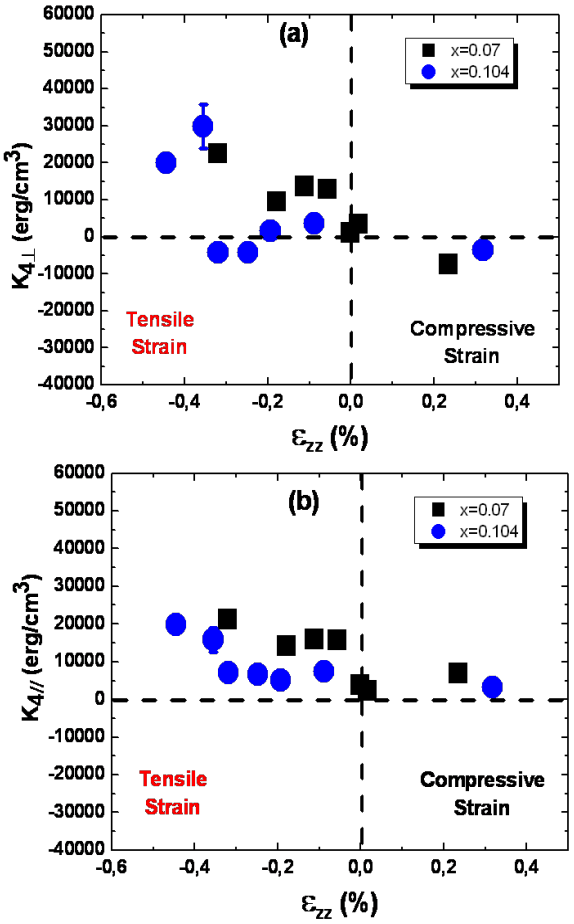

Figure 3.27: The cubic anisotropy $K_{4\perp}$(a) $K_{4\parallel}$(b) dependence on ε_{zz} for $Ga_{0.093}Mn_{0.07}As_{1-y}P_y$ (squares, black) and $Ga_{0.896}Mn_{0.104}As_{1-y}P_y$ layers (circle, blue)

and $Ga_{0.896}Mn_{0.104}As_{1-y}P_y$ respectively. The fourth-order parameters $K_{4\perp}$ and $K_{4\parallel}$ are presented in figs.3.27(a),(b). $K_{4\parallel}$ varies slightly between 0 and 20000 erg/cm^3. $K_{4\perp}$ is negative with values close to -3000 erg/cm^3 for $\varepsilon_{zz} \lesssim$ -0.22%, $\varepsilon_{zz} \gtrsim 0.1\%$ and positive for -0.2%$\lesssim \varepsilon_{zz} \lesssim 0\%$ in the metallic regime. A change of sign for $K_{4\perp}$ has also been reported by [64], where the authors attributed it to extrinsic influences and, as it has been shown, it is not reproduced by calculations within the frame of micromagnetic models.

We can estimate the critical strain ε_{zz}^{crit}, where the magnetization switches between in-plane to out of plane, from the condition $H_{2\perp}+H_{4\perp}=H_{2\parallel}+H_{4\parallel}$. We obtain ε_{zz}^{crit}=-0.12 %, ε_{zz}^{crit}=-0.08 % for $Ga_{0.093}Mn_{0.07}As_{1-y}P_y$ and $Ga_{0.896}Mn_{0.104}As_{1-y}P_y$ respectively. In the following chapter the variation with tem-

perature of the magnetization, magneto-crystalline anisotropy constants and the free energy density will be discussed in more details.

3.6.5 Free Energy Densities

The reorientation of the magnetization by an external magnetic field is strongly dependent on the energy barriers related to the internal anisotropy fields. From the numerical values of the anisotropy constants we can calculate the free-energy density F as a function of the crystalline orientation (Θ,Φ). In figures 3.28 and 3.29 we show the free energy surfaces for zero applied magnetic field for $Ga_{0.093}Mn_{0.07}As_{1-y}P_y$ and $Ga_{0.896}Mn_{0.104}As_{1-y}P_y$ layers respectively. These surfaces show clearly the energy barriers for the magnetization reorientation and define the preferential axes of the magnetization. A more detailed view can be obtained from cross sections of the surfaces in particular planes.

For example in Fig.3.30 we have plotted the out-of plane angular variation of the free-energy density as a function of Θ angle. These figures illustrate that while for the two extreme cases the difference between the energy along the easy and hard axes are considerably large, for the intermediate case of the sample with y=0.056, the energy density is nearly isotropic. This is a very important result as it shows that one can reduce the energy barriers for the magnetization switching. Layers with reduced barriers should be very interesting objects in FM/NM/FM trilayer structures currently studied for their tunnelling magneto resistance effects. The energy surfaces for the in-plane orientations (Θ=90°) of the magnetization for the $Ga_{0.093}Mn_{0.07}As_{0.966}P_{0.034}$ sample are shown in figures 3.31(a)-(c) at several temperature. At low temperature, the easy axis of the magnetization is not aligned in the absence of applied magnetic fields along any high symmetry direction of the film due to competing second order and fourth order anisotropy fields. The easy axis is oriented along an intermediate direction given by Φ=-8.1° with respect to the [100] direction. When we raise the temperature the easy axis monotonously shifts to the [1-10] direction. These particular orientations correspond to the predominance of the $K_{2\|}$ and $K_{4\|}$ constants, as shown in figure 3.31(d). In addition to the strain, the temperature is thus another control parameter which can be used to manipulate the orientation of the magnetization of $Ga_{1-x}Mn_xAs_{1-y}P_y$ ferromagnetic films with a fixed Mn concentration [156, 83]. However, the orientation of in-plane easy axes at low temperature and their shifts with temperature to the [1-10] direction depend on y and Mn concentration.

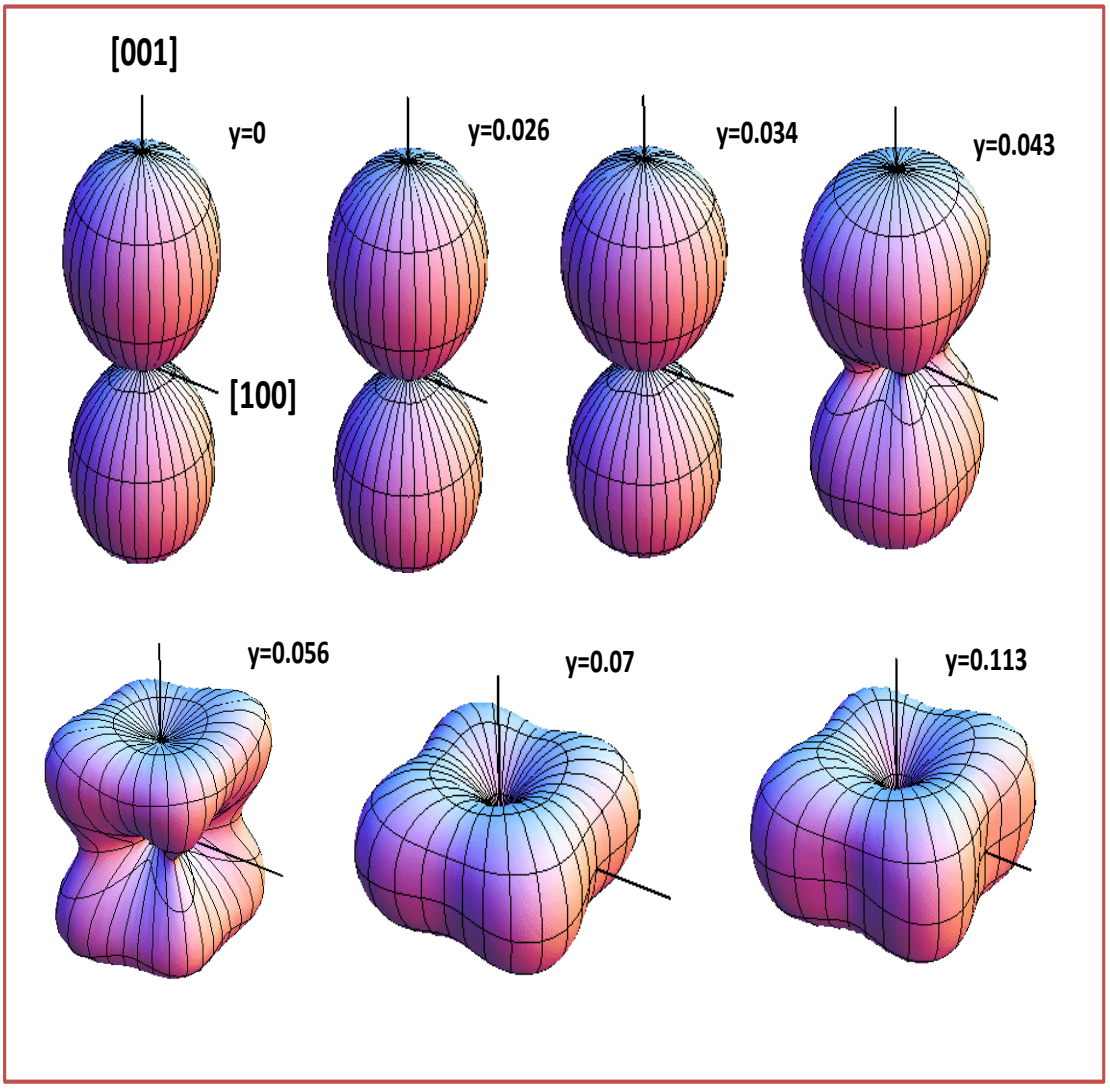

Figure 3.28: Three-dimensional plot of free-energy densities for $Ga_{0.093}Mn_{0.07}As_{1-y}P_y$ layers at 4K with different y.

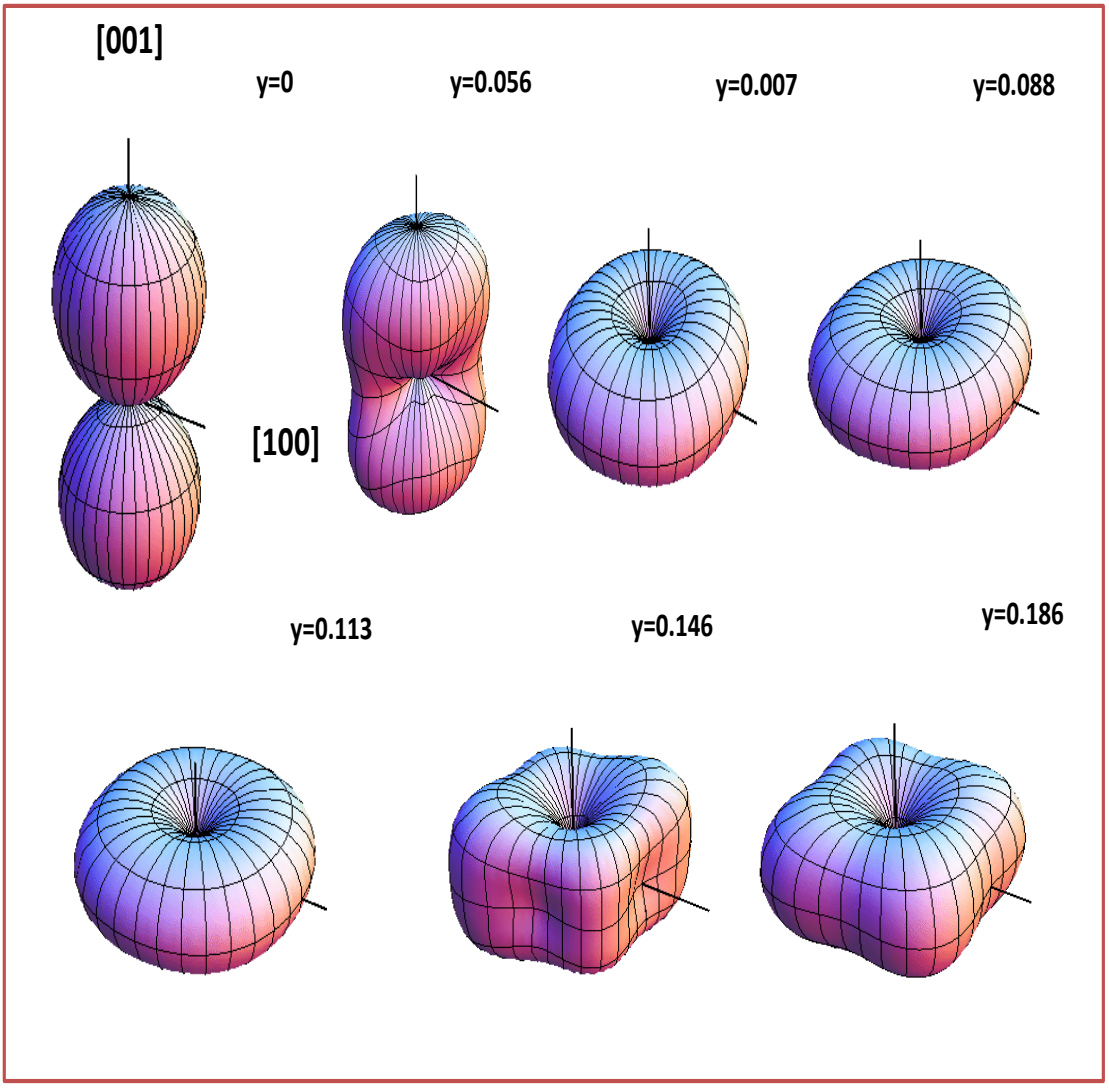

Figure 3.29: Three-dimensional plot of free-energy densities $Ga_{0.896}Mn_{0.104}As_{1-y}P_y$ layers with different y.

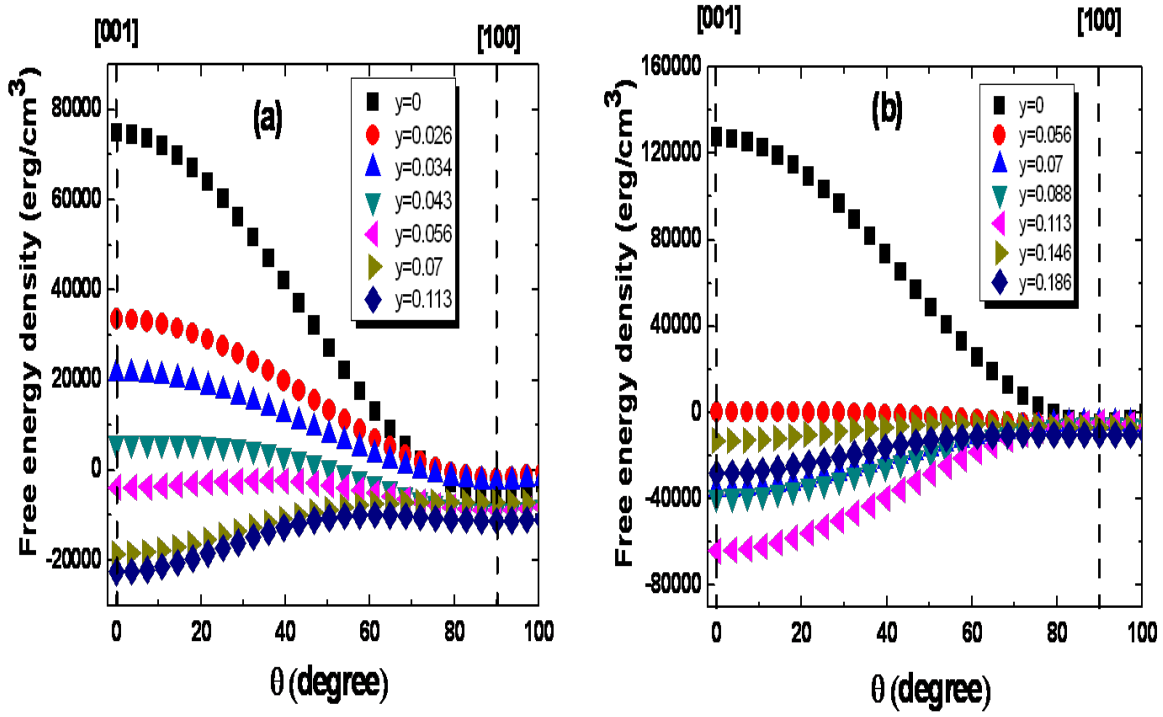

Figure 3.30: Free energy densities at 4K for $Ga_{0.093}Mn_{0.07}As_{1-y}P_y$ (a) and $Ga_{0.896}Mn_{0.104}As_{1-y}P_y$ (b) layers as a function of the out-of plane orientation Θ for Φ=45° and for different values of y.

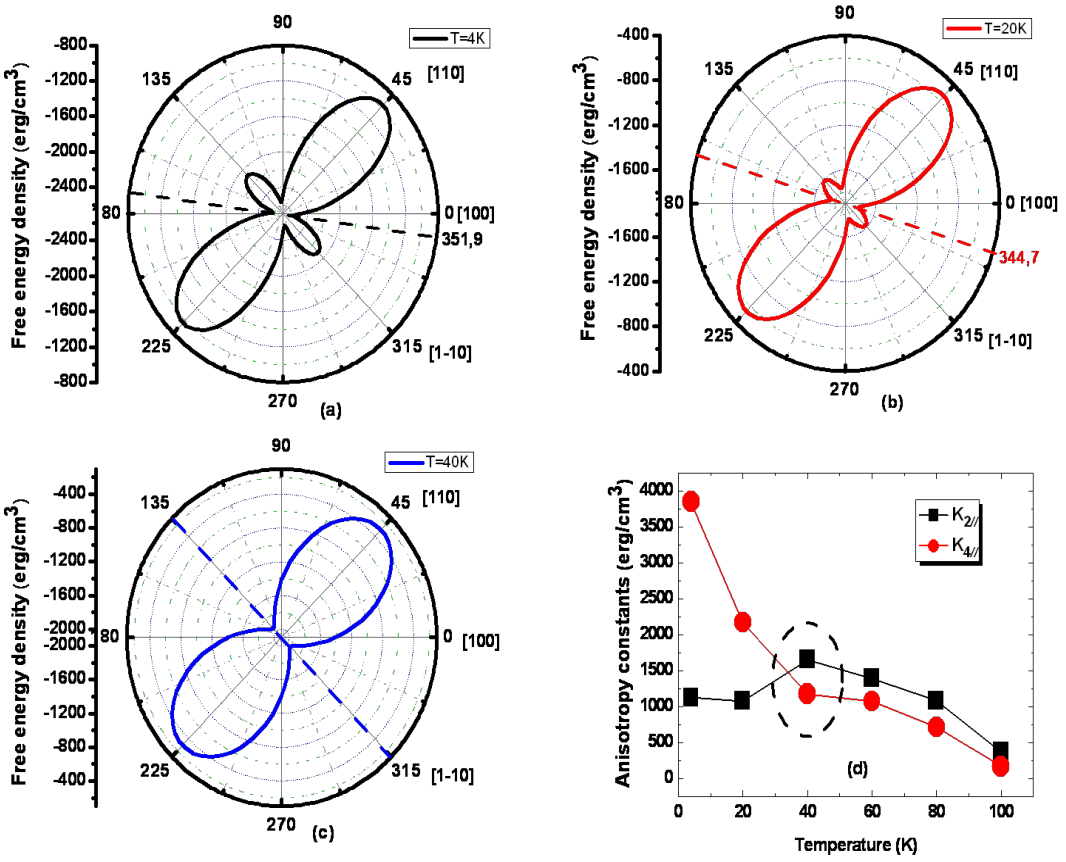

Figure 3.31: Free energy densities as a function of the in-plane magnetization orientation for |M| | cosΦ, sinΦ,0| for $Ga_{0.093}Mn_{0.07}As_{0.966}P_{0.034}$ at T=4K (a) T=20K (b) T=40K (c). The directions of the energy minima shift toward [1-10] with increasing temperature. (d) The magneto-crystalline anisotropy constant $K_{2\|}$ and $K_{4\|}$ as a function of temperature. The lines are guides for the eyes. The change in easy axis orientation is indicated by the circle.

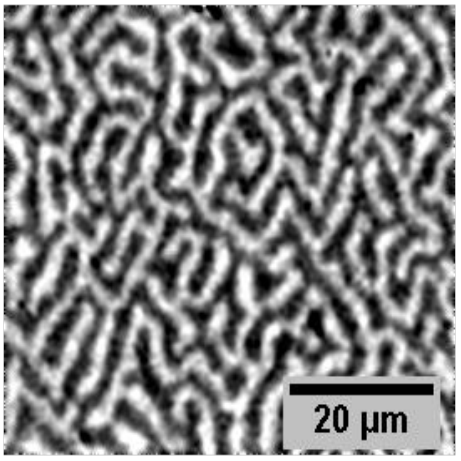

Figure 3.32: The magneto-optical images of domains with magnetization perpendicular to the layer "up" (white) and "down" (in gray) self-organized in zero field at 80K for $Ga_{0.896}Mn_{0.104}As_{0.93}P_{0.07}$ sample.

3.6.6 Magneto-optical Kerr (MOKE) microscopy measurements

An easy axis of magnetization perpendicular to the layer enables studies of the dynamics of magnetic domain walls (DW) by Magneto-optical Kerr microscopy [40, 67]. This configuration was first achieved by the growth of $Ga_{0.093}Mn_{0.07}As$ films on a thick (>2μm) relaxed GaInAs buffer layer. However, this approach introduces fluctuations of the magnetic properties, which are detrimental for the propagation of the magnetic DW [41]; pointlike pinning centers for the DW were observed and attributed to emerging dislocations [155]. We have shown in a previous section that a few percent of phosphorus can lead to the same geometry, a perpendicular magnetic easy axis, but the layer now contains much less extended defects. In this section we report the experimental results by magneto-optical Kerr (MOKE) microscopy from which we can obtain the important micro-magnetic parameters such as the DW width and the spin stiffness constant. In addition, the determination of the spin stiffness constant gives access to the exchange interaction constant between localized Mn and itinerant holes(J_{pd}).

Competition between dipolar energy and exchange results in the self-organization of domains into periodic patterns if the DW pinning by defects is negligible. Fig.3.32 shows the images of the domain structure taken with magneto-optical Kerr microscope. They were measured at 80 K for a $Ga_{0.896}Mn_{0.104}As_{0.93}P_{0.07}$ sample in zero field. Owing to the very low density of dislocation the magnetic domains can reach

self-organized configurations in the demagnetized state in zero field. The domain walls may bend in the plane, giving a labyrinthine structure at a macroscopic scale. However a quasi-period can still be measured. In order to determine the micromagnetic parameters from this period one can use the model of domain self organisation. The period is obtained from the minimization of the energy. It satisfies the equation[75];

$$\lambda_c = \frac{p^2}{\pi^3}\sum_{n=1}^{\infty} n^{-3}[1-(1+\frac{2\pi n}{p})exp(-\frac{2\pi n}{p})]sin^2(\frac{\pi}{2}n(1+<m>)) \qquad (3.8)$$

where p is the reduced period, <m> is the reduced magnetization, λ_c is a dimensionless parameter . The reduced period p and λ_c are defined by;

$$p = \frac{W_1 + W_2}{d} \qquad (3.9)$$

$$\lambda_c = \frac{4\sqrt{AK_u}}{\mu_0 M_s^2 d} = \frac{\sigma}{2K_d d} \qquad (3.10)$$

where d is the thickness of the layer, M_s is the saturation magnetization, W_1 et W_2 are the stripe width of domain with magnetization parallel (up) and anti-parallel (down) to the to the applied field respectively.

Using eq. 3.8 one determines λ_c and from eq.3.10 one determines the effective exchange constant A between Mn spins and the magnetic domain wall width, two key parameters for the domain wall dynamics. A clear improvement is obtained as compared to the previous study performed on $Ga_{0.093}Mn_{0.07}As$/GaInAs [66]. The values of the DW width $\triangle$ and spin stiffness constant A as a function of temperature are shown in fig.3.33. The domain width is weakly dependent on the temperature which was already predicted by Dietl et al.[36]. We find that the DW width in the $Ga_{0.896}Mn_{0.104}As_{0.93}P_{0.07}$/GaAs layer is larger than in $Ga_{0.093}Mn_{0.07}As$/GaInAs ($\triangle \approx 3.2$ nm from ref.[66]). This implies that one could expect a higher DW mobility in the P alloyed thin films.

The spin stiffness constant A is found to be larger in $Ga_{0.896}Mn_{0.104}As_{0.93}P_{0.07}$ than in comparable $Ga_{0.093}Mn_{0.07}As$ (A$\approx$0.1 pJ/m^{-1} at 4K from ref.[66]). Note that, the stiffness constant A depends on J_{pd}, carrier (hole) and Mn concentrations. We have also studied $Ga_{0.896}Mn_{0.104}As_{1-y}P_y$ films with y=0.088 and y=0.113. However, we have not observed a significant change in the spin stiffness constant A within this range of Phosphorous concentration(0.07$\leq$y$\leq$0.113) for the $Ga_{0.896}Mn_{0.104}As_{1-y}P_y$ samples. More details results are given in ref.[70].

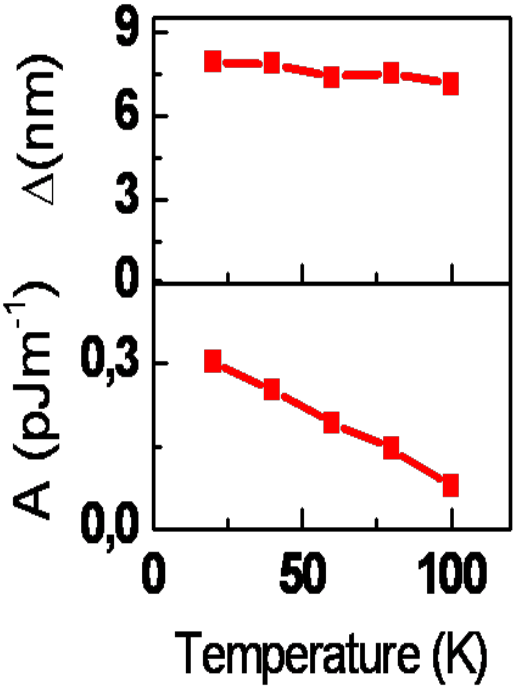

Figure 3.33: The DW width $\triangle$ and spin stiffness constant A as a function of the temperature obtained from the stripe domain period for $Ga_{0.896}Mn_{0.104}As_{0.93}P_{0.07}$ sample.

3.6.7 Conclusion

In this chapter we have shown that quaternary $Ga_{1-x}Mn_xAs_{1-y}P_y$ 50 nm thin layers can be conveniently grown by LT-MBE at conditions close to those used for $Ga_{1-x}Mn_xAs$ film growth. Phosphorous concentrations of up to y=0.20 have been incorporated without any degradation so the sample properties. Kerr microscopy has shown that the density of pinning centres is strongly reduced as compared to previously used GaInAs substrates such that selforganization of domains has been observed. The ion beam analysis performed on one highly doped film confirms the calibration of the P concentration deduced separately from the lattice parameter variation of GaAsP reference layers. We have not found any indication of the incorporation of phosphorous on interstitial lattice sites. As concerns the Mn dopant concentration we have only explored a limited region of x=0.07 and x=0.104 which were considered to be optimal for the magnetic properties (saturation magnetization, Curie temperature) in view of our previous studies of ternary $Ga_{1-x}Mn_xAs$ alloys. We have not addressed the subject of high doping levels which might be on interest if higher Curie temperatures are searched for. We have neither optimized the annealing conditions which might be specific for different P doping levels. In all models a random distribution of the Mn atoms over the Ga lattice sites is assumed. The question whether this is also valid with additional P alloying should be explored further. In this context one might mention that for particular P/As ratios ordered anion sublattice structures have been reported in GaAsP alloys.

The P alloying at fixed Mn dopig has allowed us to vary the uni-axial strain continuously from compressive to tensile. We can thus grow on GaAs(001) substrates ferromagnetic thin layers with in-plane and out-of-plane anisotropies. Contrary to previous reports for $Ga_{1-x}Mn_xAs_{1-y}P_y$ layers obtained by ion implantation [126], LT-MBE grown layers stay metallic up to P doping levels of y$\approx$ 0.10. The exact value will depend on the Mn doping. The increasing depth of the Mn acceptor level allows also to engineer ferromagnetic layers with thermally activated conductivity due to a freeze out of holes at temperatures below T=40K. Such layers might be interesting for the electrical control of the magnetization due to the reduced effective carrier concentration. Quaternary $Ga_{1-x}Mn_xAs_{1-y}P_y$ thin films might also give further insight in the ferromagnetism mediated by carriers located in an impurity band. This subject has not yet been studied theoretically at all.

Chapter 4

In-Plane/Out-of Plane Magnetization switching in films with critical strain

4.1 Introduction

The magnetic properties of $Ga_{1-x}Mn_xAs$ depend largely on the Mn and the related free hole concentrations, strain and native growth related defects. They are further modified by the post growth annealing step required to obtain high critical temperatures [139, 5, 37, 156, 160]. The highest critical temperature were observed for total Mn doping levels of x=0.10 which requires the use low temperature MBE as the equilibrium solubility of Mn is below x=0.01. In chapter 3, we have shown that additional alloying with phosphorous allows to modify the epitaxial strain and consequently the magnetic anisotropy of $Ga_{1-x}Mn_xAs_{1-y}P_y$ films on GaAs(001), independently from the Mn doping level. Thus $Ga_{1-x}Mn_xAs_{1-y}P_y$ layers with either in-plane or out-of-plane easy magnetization axis can be elaborated for Mn concentrations of x=0.07 and 0.104. In particular, a choice of an intermediate P doping level (y≈0.06) allows to obtain layers with unique properties: when their uni-axial anisotropy field just compensates the demagnetization field switching of the magnetization between in-plane and out-of plane orientations becomes possible by a small temperature rise or by application of a small magnetic field. This is important for memory device application. In this chapter we report a combined ferromagnetic resonance (FMR), and static magnetization study of such layers in which we have investigated in detail the magnetic anisotropies.

4.2 Experiment and samples characteristics

We present here the study of a set of three samples which are 50 nm thick $Ga_{1-x}Mn_xAs_{1-y}P_y$ films grown by low temperature MBE on GaAs(001) substrates. After the growth the samples were thermally annealed under N_2 atmosphere at 250° for 1 hour. Two samples have a Mn concentration of x=0.07: $Ga_{0.093}Mn_{0.07}As_{1-y}P_y$ with y=0.043 or y=0.056. The uni-axial strain ε_{zz} determined by high resolution X-ray diffraction are -0.056 % and -0.112 % respectively (after the annealing step). The third sample is; $Ga_{0.896}Mn_{0.104}As_{0.944}P_{0.056}$ with uni-axial strain ε_{zz} equal to -0.089%. The magnetization of the films was measured by SQUID. The magneto-crystalline anisotropy constants and their temperature dependence were determined by X-band (9 GHz) FMR measurements.

4.3 FMR measurements

4.3.1 FMR spectra

In fig.4.1(a),(b) we show typical FMR spectra of the $Ga_{0.093}Mn_{0.07}As_{0.944}P_{0.056}$ sample for the in-plane and out-of plane orientation at T=4K and T=60K respectively. The resonance positions indicate the [100] and [001] as the easy axes at T=4K and T=60K respectively. Note that we have observed the reduction of line-width with the temperature (for temperature well below Tc) particularly for the [110] and [1-10] directions which is also observed in other samples.

We show in fig.4.2 typical FMR spectra of the $Ga_{0.896}Mn_{0.104}As_{0.944}P_{0.056}$ sample for the in-plane and out-of plane orientation at T=4K. The easy axis is parallel to [100] with a resonance field of H=3100 Oe. We observe only a small difference in the resonance positions between the four high symmetry directions. The linewidth of the FMR spectra is very small indicating that the layers are also very homogeneous. We have also observed a second resonance of small intensity which from its angular dependence can be identified as the first mode of spin-waves.

4.3.2 Angular dependence of the FMR field

From the angular dependences of the FMR spectra we can determine the easy axes of magnetization under an applied magnetic field and deduce the anisotropy constants which allow us to calculate the equilibrium orientations of the magnetization for any value of the applied magnetic field. In fig.4.3(a),(b) we show the angular

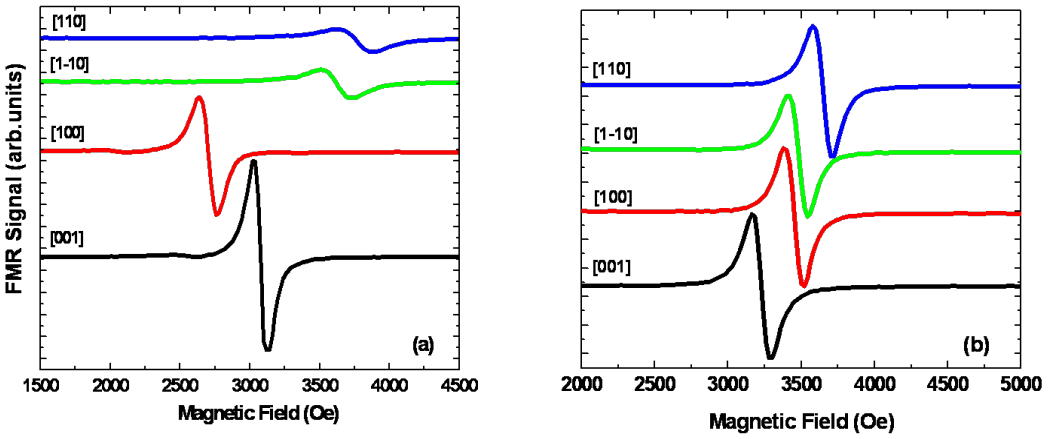

Figure 4.1: FMR spectra observed at T=4K (a) and T=60K (b) of $Ga_{0.093}Mn_{0.07}As_{0.944}P_{0.056}$ for the magnetic field aligned along the four high symmetry directions: the perpendicular(H‖[001]) and three in-plane (H‖[110],H‖[1-10] and H‖[100]) directions.

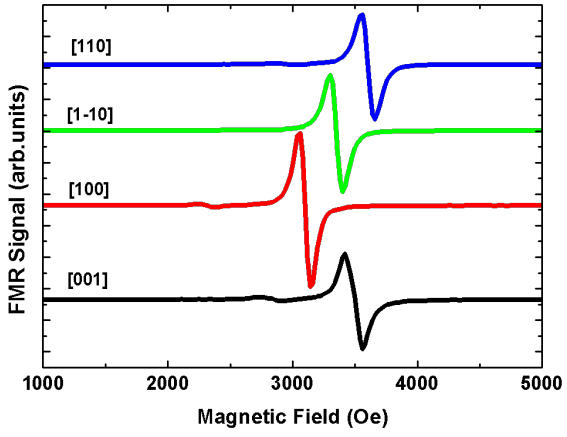

Figure 4.2: FMR spectra observed at T=4K of $Ga_{0.896}Mn_{0.104}As_{0.944}P_{0.056}$ for four high symetry axes: the perpendicular (H‖[001]) and three in-plane (H‖[110],H‖[1-10] and H‖[100]) directions.

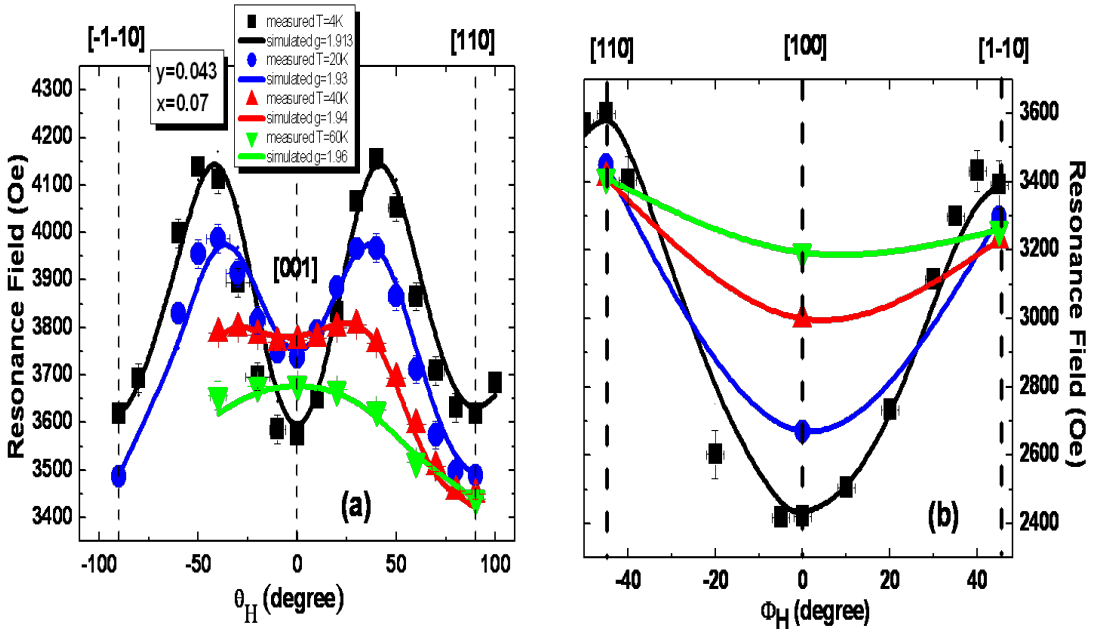

Figure 4.3: Angular dependence of the FMR resonance field (symbols) for the $Ga_{0.093}Mn_{0.07}As_{0.957}P_{0.043}$ in the out-of plane configuration (a) and in-plane configuration (b); the simulated angular variations (solid lines) are obtained from the anisotropy constants and the g-values of g=1.913 at 4K g=1.93 20K, g=1.94 at 40K, and g=1.96 at 60K

dependences of the uniform mode spectra in the (1-10), (001) planes respectively at different temperatures for the $Ga_{0.093}Mn_{0.07}As_{0.957}P_{0.043}$ sample. For this sample the easy axis of magnetization is always along the [100] direction for all temperatures. At low temperature the hard axis of magnetization is no longer aligned along any high-symmetry direction but is rotated towards the [111] direction; with increasing temperature the hard axis shifts back to the [001] direction. These orientations can be attributed to a competition between the cubic $H_{4\perp}$ and the uni-axial $H_{2\perp}$ anisotropy fields: the angular dependence of the resonance field is determined by $H_{4\perp}$ at low temperature (see fig.4.6) whereas at higher temperatures all anisotropy fields are of comparable value. The Landé g factor has equally been evaluated from the angular variation. It is slightly different from g=2.00 and varies from g=1.913 at 4K to 1.96 at 60K. The assumption of a constant g-factor of 2.00 of assumed in a simplified approach would have led to different K values.

In fig.4.4(a),(b) the angular dependences of the uniform mode spectra of the $Ga_{0.093}Mn_{0.07}As_{0.944}P_{0.056}$ sample in the (1-10), (001) planes respectively are shown

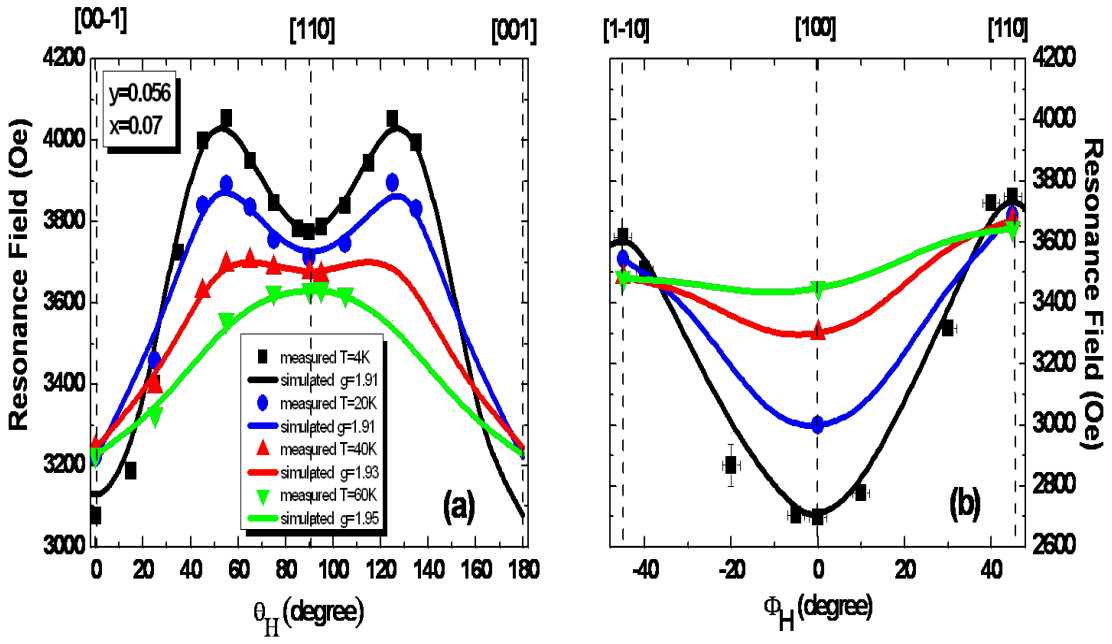

Figure 4.4: Angular dependence of the FMR resonance field (symbols)for $Ga_{0.093}Mn_{0.07}As_{0.944}P_{0.056}$ in the out-of plane configuration (a) and in-plane configuration (b); the simulated angular variations (solid lines) are obtained from the anisotropy constants and the g-values of g=1.91 at 4K and 20K, g=1.93 at 40K, and g=1.95 at 60K

for different temperatures. We observe that at 4K as in the previous case the H||[100] axis is the easy axis of magnetization but with increasing temperature to T=40K the easy axis shifts to the [001] orientation which indicates that the easy axis of magnetization has rotated from an in-plane direction at T=4K to an out-of-plane orientation at T=40 K. If the temperature is further increased the FMR spectra become quasi isotropic for in-plane rotations and only a small in-plan out-of-plane anisotropy persists. For this sample, the hard axis magnetization is also not aligned along any high-symmetry direction at low temperature, but with increasing temperature the hard axis monotonously shifts to the [110] direction.

The angular dependence of the uniform mode FMR spectra for the $Ga_{0.896}Mn_{0.104}As_{0.944}P_{0.056}$ at two temperature shows that the easy axis of magnetization is parallel to [100] at 4K with a resonance field of 3100 Oe(4.5). Note that the easy axis switches also from H||[100] to H||[001] at T=100K for this sample.

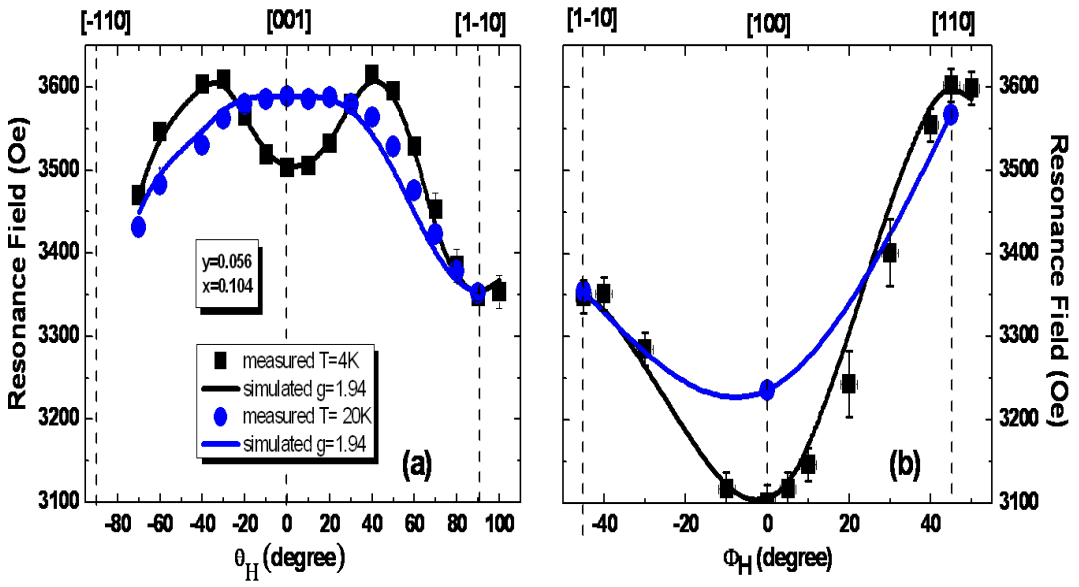

Figure 4.5: Angular dependence of the FMR resonance fields (symbols) for $Ga_{0.896}Mn_{0.104}As_{0.944}P_{0.056}$ in the out-of plane configuration (a) and in-plane configuration (b); the simulated angular variations (solid lines) are obtained from the anisotropy constants and the g-values of g=1.94 at 4K and 20K

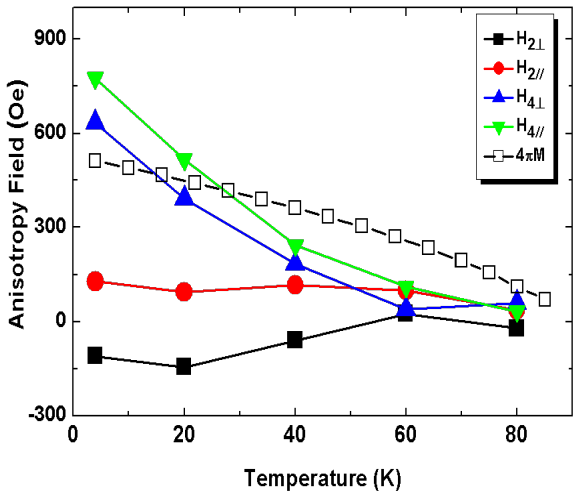

Figure 4.6: Anisotropy fields for the $Ga_{0.093}Mn_{0.07}As_{0.957}P_{0.043}$ sample as a function of temperature; the demagnetization field is equally indicated; $H_{2\perp}$(squares, black), $H_{2\|}$(circles,red), $H_{4\perp}$(up triangle, blue), $H_{4\perp}$(down triangle, green). The symbols are experimental results; lines are guide for the eyes.

4.3.3 Magneto-crystalline Anisotropy

Anisotropy fields play a critical role in the process of the magnetization easy axis reorientation. We will now discuss for these quasi-isotropic layers the anisotropy fields defined as $2K_i$/M and their variation with temperature. As in the previous chapter the constants were determined from a fit of the angular variation of the FMR spectra. The anisotropy fields obtained from the FMR analysis for the $Ga_{0.093}Mn_{0.07}As_{0.957}P_{0.043}$ sample are shown in fig.4.6 as a function of temperature. At low temperature the cubic anisotropy is always much larger than the perpendicular uni-axial anisotropy. The cubic anisotropy decreases rapidly with increasing temperature. As a result, at T= 60K the perpendicular uni-axial anisotropy has a value comparable to the cubic anisotropy.

In fig.4.7, we show the temperature dependence of the anisotropy fields for the $Ga_{1-x}Mn_xAs_{0.944}P_{0.056}$ samples with x=0.07 (a) and x=0.104 (b). As shown in fig.4.7 (a), at T=4K the cubic anisotropy fields dominate the magnetic anisotropy field; however, with increasing temperature they decrease rapidly down to zero and the perpendicular uni-axial anisotropy field becomes dominant at T>40K. The per-

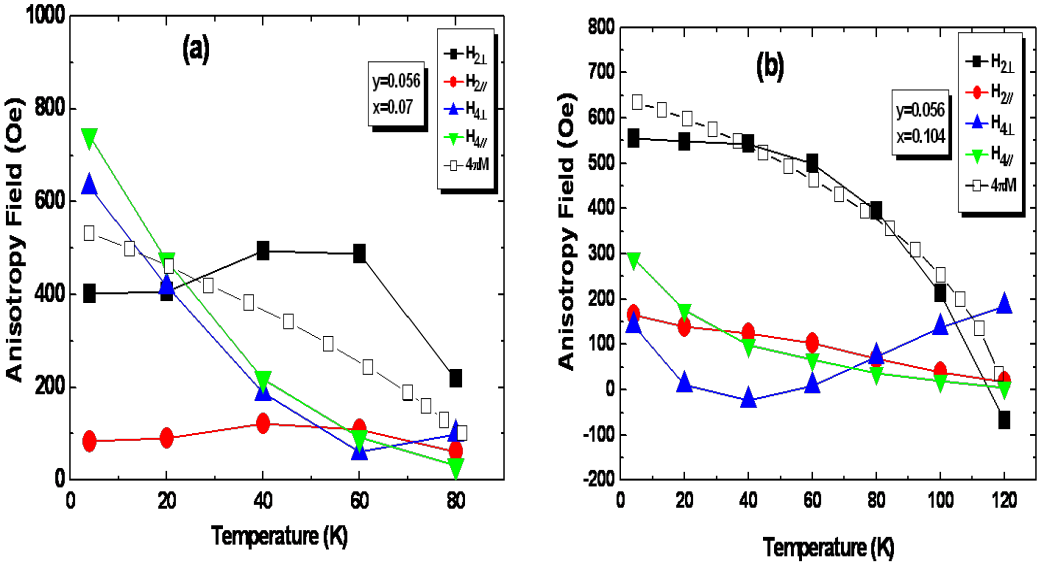

Figure 4.7: Anisotropy fields for $Ga_{1-x}Mn_xAs_{0.944}P_{0.056}$ with x=0.07 (a) and x=0.104 (b)as a function of temperature; the demagnetization field is equally indicated;$K_{2\perp}$(squares, black) $K_{2\|}$(circles,red), $K_{4\perp}$(up triangle,blue), $K_{4\perp}$(down triangle, green).The symbols are experimental results; lines are guide for the eyes.

pendicular uni-axial field $H_{2\perp}$ is comparable but slightly inferior below T=30K and becomes superior above this temperature. Its value is however small and positive whereas a similar doped GaMnAs layer on GaAs(001) has typical $H_{2\perp}$ value of 3500 Oe. As shown in fig.4.7 (b), the perpendicular uni-axial anisotropy is dominant at low temperature and comparable with demagnetization field 4πM, but it decreases monotonously with increasing temperature.

4.3.4 Free energy density

The free energy density F at zero applied field can now be calculated from these anisotropy field values. In fig.4.8 we present F as a function of the crystalline orientation (Θ,Φ) for the $Ga_{0.093}Mn_{0.07}As_{0.944}P_{0.056}$ sample at several temperatures. These 3D plots illustrate clearly the reorientation with temperature of the easy magnetization axis direction from in-plane to out-of plane: at 4K the in-plane direction [100] energy minima are deeper than those that appeared along the out-of

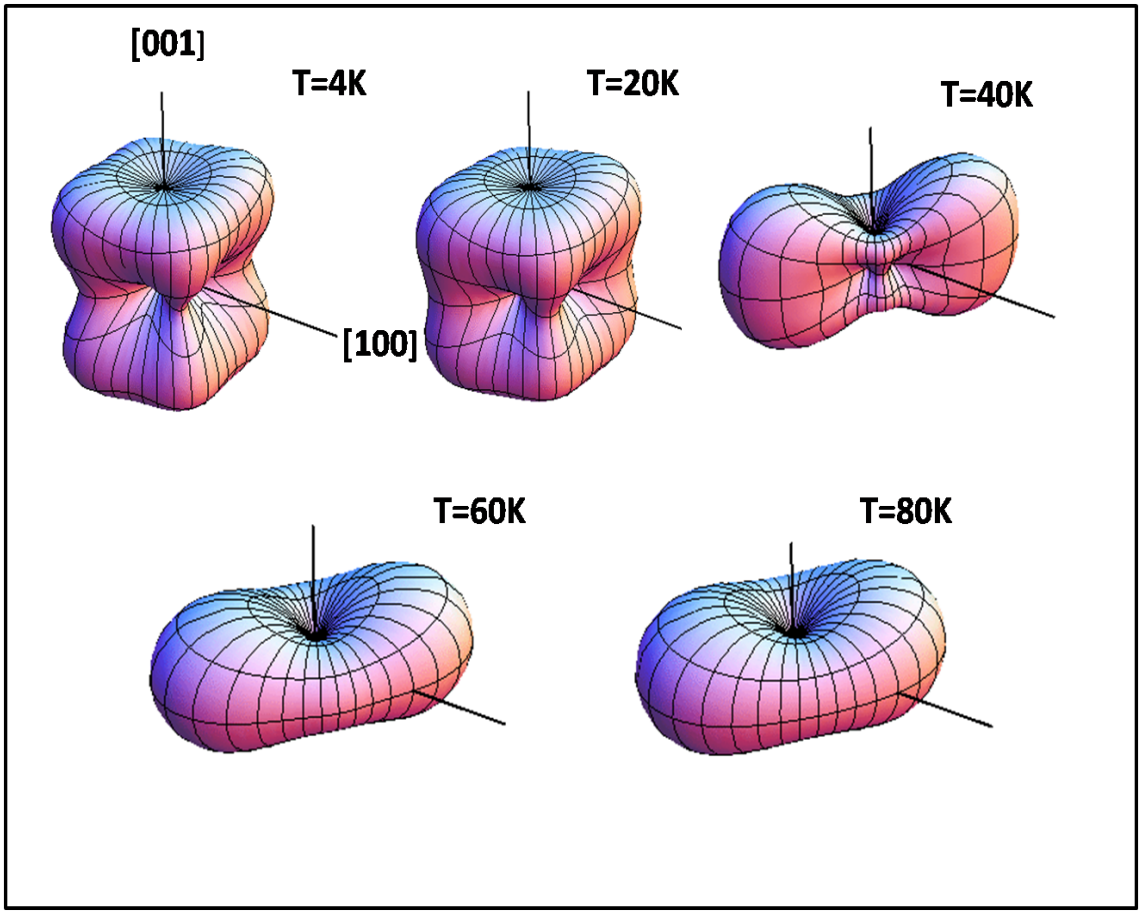

Figure 4.8: 3D plot of free energy densities for $Ga_{0.093}Mn_{0.07}As_{0.944}P_{0.056}$ at different temperatures calculated from the anisotropy field given in fig.4.7(a). Energy minima occur near the [100] direction at 4K and shift to the [001] direction as the temperatures increases

plane [001] direction; however with increasing temperature these minima become relatively deeper while the ones in the [100] direction become shallower. For T=40K the minima energy is along the out-of plane [001] direction. The deepest energy minima indicate the easiest magnetic axes direction.

In fig.4.9 we show this transition in more detail in a 2D plot corresponding to the crossection of the free energy surface with the (010) plane. The in-plane anisotropy changes also with temperature: the easy in-plane orientation shifts monotonously from near [100] for T=4K to [1-10] for T=60K (fig.4.10).

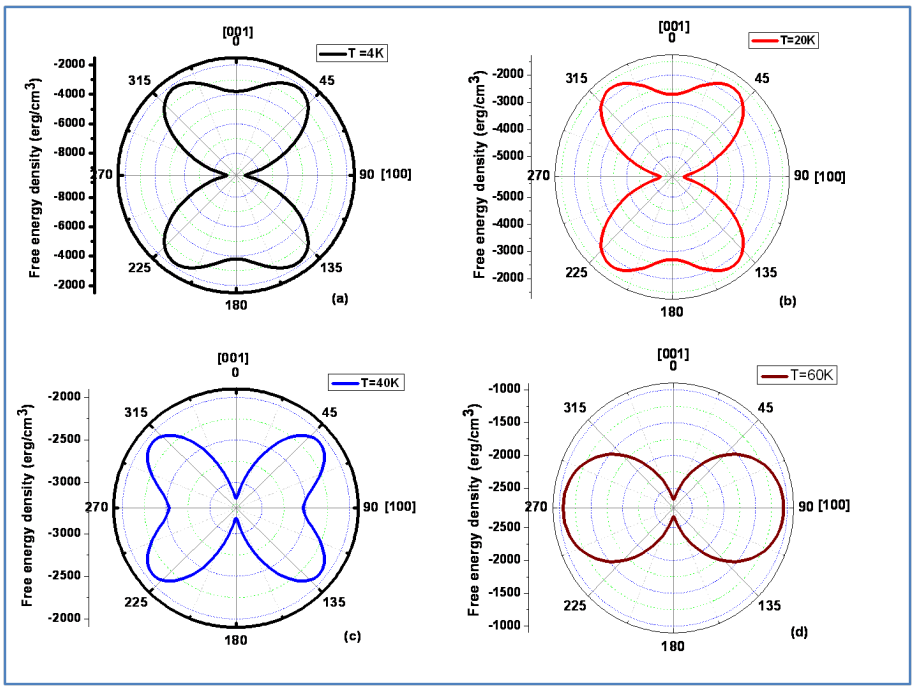

Figure 4.9: The energy density as a function of the out-of-plane orientation for Θ, Φ=0°. The energy minima occur near the [100] direction at 4K and shift to the [001] direction as the temperature increases.

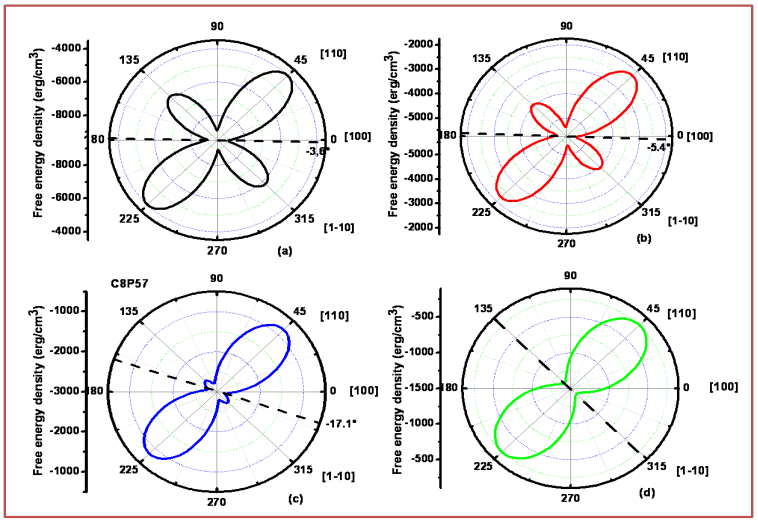

Figure 4.10: Free-energy densities as a function of the in-plane magnetization orientation |M| | cosΦ, sinΦ,0| at T=4K (a) T=20K (b) T=40K (c) and T=60K (d). The directions of the energy minima shift toward the [1-10] direction with increasing temperature.

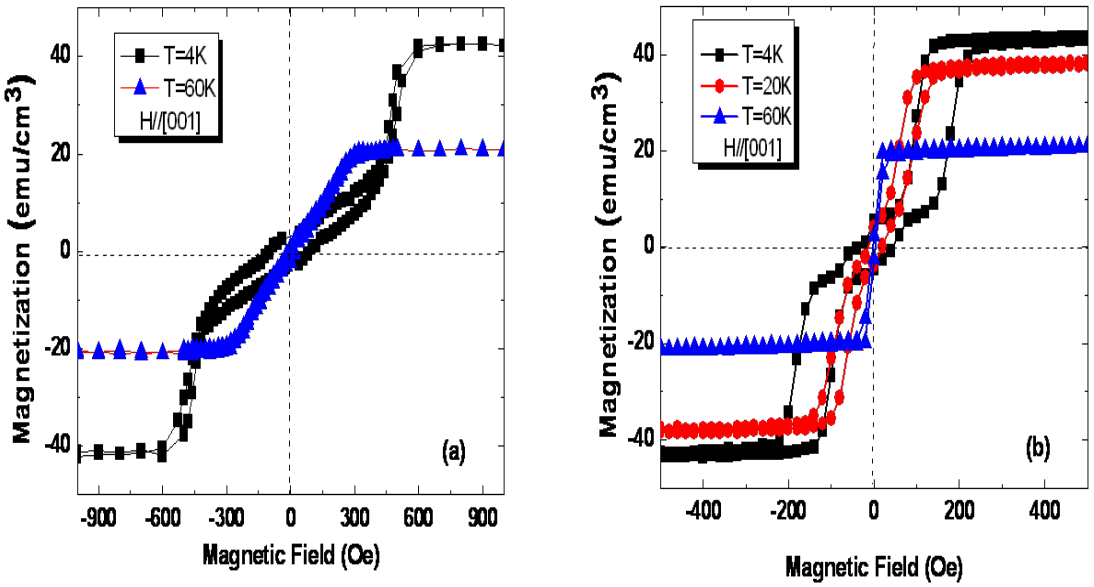

Figure 4.11: Magnetization curves as a function of the magnetic field applied along [001] direction for $Ga_{0.093}Mn_{0.07}As_{1-y}P_y$ layers with y=0.043 (a) and y=0.056 (b); T= 4K (square, black), T=20K (circle, red), T=60K (triangle, blue)

4.4 Magnetization measurements

In fig.4.11, we show the magnetization curves M(H) for H||[001] for $Ga_{0.093}Mn_{0.07}As_{1-y}P_y$ with y=0.043 (a) and y=0.056 (b) for different temperatures. In fig.4.11 (a), at T=4K, we observe a double slope characteristic for a non-coherent magnetization reversal. At 60 K the remnant magnetization is close to zero. In Fig.4.11 (b), for the $Ga_{0.093}Mn_{0.07}As_{0.944}P_{0.056}$ sample, we observe also a double slope characteristic for a non-coherent magnetization reversal at T=4K and T=20K. At T=60K we observe square loops with coercive fields H_c=3 Oe. For this temperature the easy axis is perpendicular to the film plane. The non-coherent magnetization reversal at low temperature can be understood as follows: at high magnetic fields, the Zeeman term is dominant and orients the magnetization out of plane; when the magnetic field is decreasing, the equilibrium orientation switches gradually to the [100] direction -the easy axis for zero applied field- due to the influence of the magneto-crystalline anisotropy fields. In the following subsection we will discuss this in details.

Magnetization curves M(H) for with H||[100] for $Ga_{0.093}Mn_{0.07}As_{0.944}P_{0.056}$ sample are shown in fig.4.12 for different temperatures. We observe square hysteresis

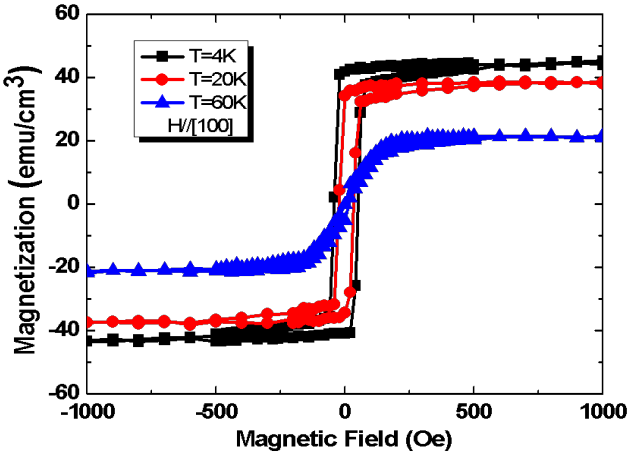

Figure 4.12: Magnetization curves as a function of the magnetic field applied along H‖[100] for the $Ga_{0.093}Mn_{0.07}As_{0.944}P_{0.056}$; T= 4K (square, black), T=20K (circle, red), T=60K (triangle, blue)

cycles with a coercive field of 45 Oe and 25 Oe at 4K and 20K respectively. At 60K the remnant magnetization is close to zero as the easy axis is now perpendicular. The hysteresis cycles of these samples are consistent with previously discussed FMR measurements.

4.5 Mechanism of in-plane/out-of-plane magnetization reversal

In order to understand the non-coherent magnetization reversal at low temperature, and its change with temperature and magnetic field in samples with critical strain, we need to examine the magnetic anisotropies which determine the equilibrium orientations of the magnetization. The free energy density F of a homogeneous magnetized thin film with a magnetic field applied perpendicular to the layer plane (i.e., along the [001] direction) can be expressed as follows[160, 96]:

$$F = -MHcos\theta + 2\pi M^2 cos^2\theta - \frac{M}{2}\left[H_{2\perp}cos^2\theta + \frac{1}{2}H_{4\perp}cos^4\theta + \frac{1}{2}H_{4\parallel}sin^4\theta + \frac{1}{2}H_{2\parallel}sin^2\theta\right] \tag{4.1}$$

Here, the first term is the Zeeman energy; θ is the angle between the magnetization vector and the sample normal (i.e. the [001] direction); the second term

is the demagnetization energy (or shape anisotropy) and last term is the magneto-crystalline anisotropy.

We show in fig.4.13 (a),(b) the magnetization hysteresis curves M(H) at 4K for the $Ga_{0.093}Mn_{0.07}As_{0.944}P_{0.056}$ sample for a magnetic field applied parallel to [001] and the corresponding free energy curves in the (010) plane for different applied fields. As shown in 4.13 (b), the free energy density has a minimum at $\Theta=\pi/2$ for H=0 Oe which indicates that the easy axis is parallel to the [100] direction. When the external magnetic field is applied along [001] direction, the minimum energy shifts from the in-plane direction [100] to the out-of plane [001]. One can show from eq.4.1 that at low field the perpendicular magnetization M_z increases proportionally to the applied field with the slope [96]:

$$\frac{dM_z}{dH} = \frac{M}{4\pi M_{eff} + \frac{1}{2}H_{2\parallel} + H_{4\parallel}} \tag{4.2}$$

where $4\pi\ M_{eff}$=4πM-$H_{2\perp}$. As shown in fig.4.13 (b) the local minimum at θ=0° becomes increasingly pronounced as the field increases. In particular, the energies of the two local minima (at θ=0° and $\theta \approx 80°$) become equal at the field H_T in the middle hysteresis loop. This field H_T can be expressed with the anisotropy constants as follows [96]:

$$H_T = (4\pi M_{eff} + \frac{1}{2}H_{2\parallel} + H_{4\parallel}) - \sqrt{\frac{1}{2}(4\pi M_{eff} + \frac{1}{2}H_{2\parallel} + H_{4\parallel})(H_{4\perp} + H_{4\parallel})} \tag{4.3}$$

A similar behavior has already been reported in low doped $Ga_{1-x}Mn_xAs$ layers with x<0.03 [96], low hole concentration [160] and with x=0.03 in which a strain compensating intermediate GaInAs layer had been grown [90]. However, in such layers, if the uni-axial strain is indeed very weak, the magnetization and critical temperature of these layers are also reduced due to the low Mn concentration.

This can be described by the condition [96];

$$1/2(H_{4\perp} - H_{4\parallel}) < 4\pi_{M_{eff}} + 1/2H_{2\parallel} < 3H_{4\perp} + 2H_{4\parallel} \tag{4.4}$$

The uni-axial anisotropy fields have values similar to the cubic ones.

When the temperature increases, the anisotropy fields decrease but differently, as detailed in the previous section. For example; at 60K for $Ga_{0.093}Mn_{0.07}As_{0.944}P_{0.056}$ sample (fig.4.11(b)), the easy axis is parallel to the out-of-plane direction [001], resulting in the inequality $4\pi M_{eff} \equiv 4\pi$M-$H_{2\perp}$ <0. The magnetization reorients in this case at very small applied magnetic fields.

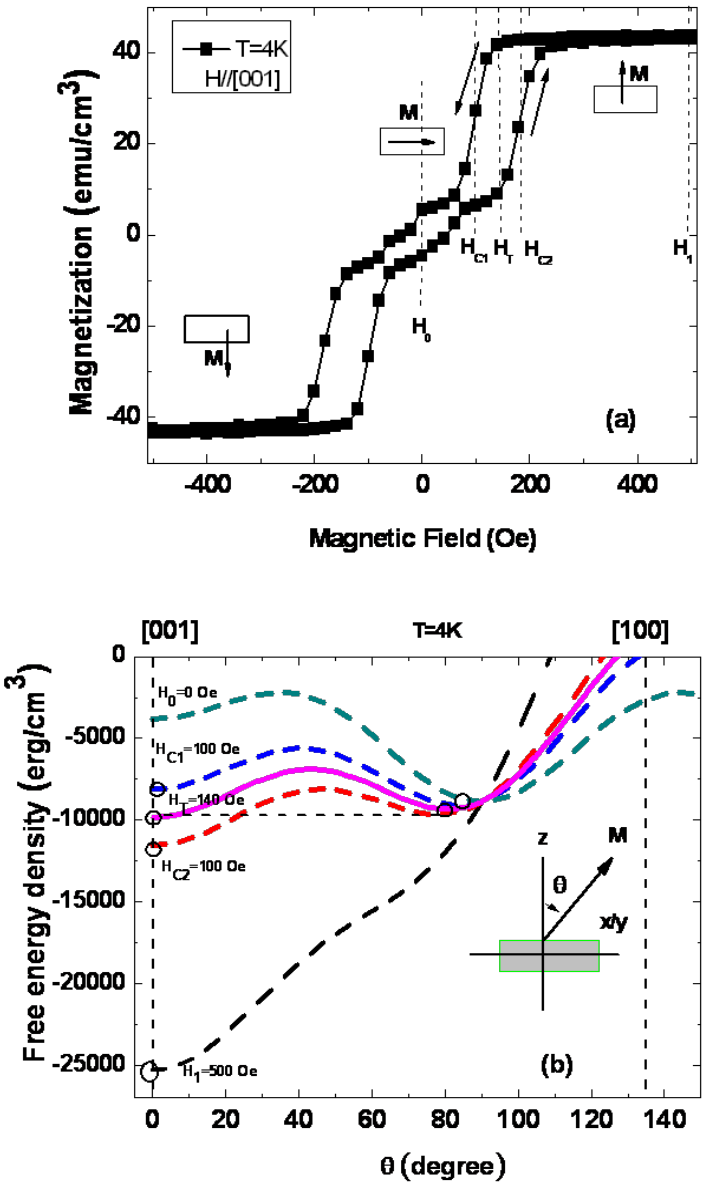

Figure 4.13: (a) Magnetization curves as a function of the magnetic field applied along [001] for $Ga_{0.093}Mn_{0.07}As_{1-y}P_y$ with y=0.056 (b) The free energy density as the function of Θ for different values of a magnetic field H along [001]. As the applied field increase, the local energy minimum moves continuously towards the applied field direction. Two local minima are equal at H_T=140 Oe.

4.6 Conclusion

$Ga_{1-x}Mn_xAs_{1-y}P_y$ films with critical strain can be obtained with intermediate phosphorous alloying. It is possible to reduce the uni-axial strain to an extend that it just balances the weak demagnetization field. In this case the equilibrium orientations of the magnetization are determined by a competition between the uni-axial and cubic anisotropy fields which are small and of comparable magnitude at low temperature. The different temperature dependencies of these fields give rise to magnetization reorientations even for small temperature changes. Such layers should be very suitable for laser assisted thermal switching of their equilibrium magnetizations.

Chapter 5

Interfacial exchange coupling MnAs/GaMnAs bilayers

5.1 Introduction

The basic understanding of spin-dependent transport and exchange coupling in ferromagnetic semiconductor multilayers is of current interest within the context of semiconductor spintronics [26, 86, 27, 76]. The exchange biasing of the ferromagnetic semiconductor GaMnAs layer by interfacing it with an antiferromagnetic layer has been investigated recently by SQUID magnetometry and FMR [45, 42]. Exchange bias effects are detected from the shift H_E of the magnetization loop M(H) relatively to the H=0 position. The unidirectional magnetic anisotropy H_{UD}, which characterizes the exchange biasing of the ferromagnetic GaMnAs layer by the antiferromagnetic top layer can also be investigated by FMR [42].

Exchange coupled bilayers of hard and soft ferromagnetic thin films show many analogies to antiferromagnetic/ferromagnetic exchange biased heterostructures which have been studied in the past [12, 68, 7, 162, 150, 109]. MnAs/GaMnAs bilayers are a good example of such composite ferromagnetic thin films [175, 166, 31, 174]. As the MnAs layer can be epitaxially grown on GaMnAs, abrupt interfaces with low interface defect densities can be obtained. For two different uni-axial anisotropic films in close contact with each other ferromagnetic exchange coupling occurs between the spins in a narrow region close to the interface between the two ferromagnetic films [65]. A recent study [175] has reported the observation of the current-perpendicular-to-the-plane (CPP) spin valve effect in such "self-exchange biased" bilayers. The results are consistent with the formation of exchange spring due to interfacial ex-

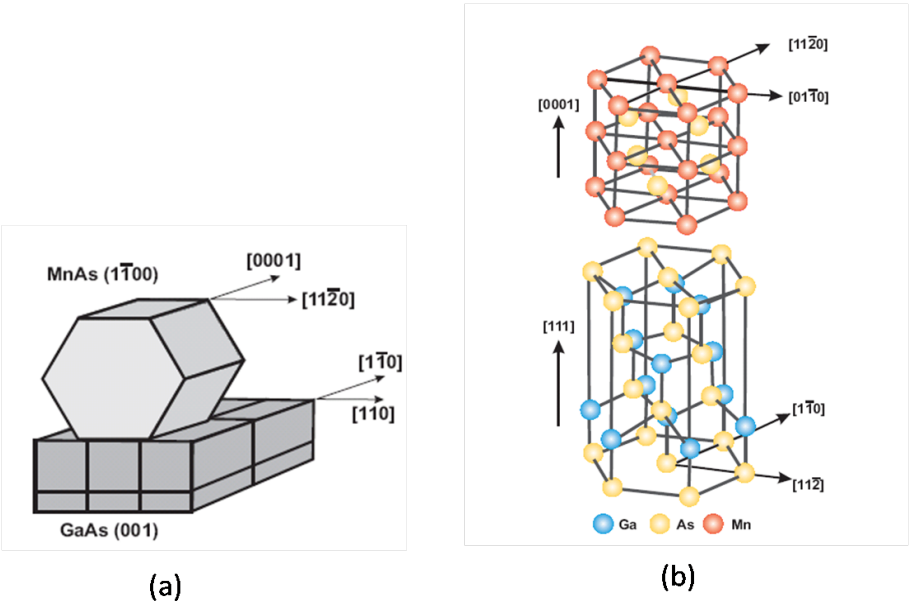

Figure 5.1: The crystallographic orientations of epitaxial MnAs layers grown on GaAs(001)(a) substrates and GaAs(111)(b) substrates[107]

change coupling between MnAs/GaMnAs bilayers with a region of inhomogeneous magnetization within the biased GaMnAs layer [166, 174]. In this chapter we report the results of SQUID and FMR measurements on MnAs/GaMnAs bilayers with very thin (15nm) MnAs layers.

The presence of the MnAs layer on top of the GaMnAs layer is also expected to modify the strain and thus its magnetic properties. It is one of the characteristics of ferromagnetic GaMnAs thin layers grown on GaAs that the lattice mismatch induced strain leads to strong anisotropy fields which determine the easy axes of magnetization. Up to now no information is available on how the strain will be modified by the MnAs top layer. We have investigated this problem by FMR spectroscopy.

In the context of spintronics hybride systems composed of ferromagnetic metals and classical semiconductors like GaAs have become increasingly important. MnAs, a ferromagnetic metal, is an interesting case for spin injection in GaAs as it can be grown epitaxially with abrupt interfaces in spite of an important lattice mismatch [49, 62, 123, 153]. The epitaxy depends on the substrate orientation and two cases GaAs(001) and GaAs(111) are generally investigated (fig. 5.1). FMR has however not yet been really applied for the study of this system due to experimental difficulties. We report also in this chapter the results of experimental FMR studies performed at high frequency which bring new interesting information for this system.

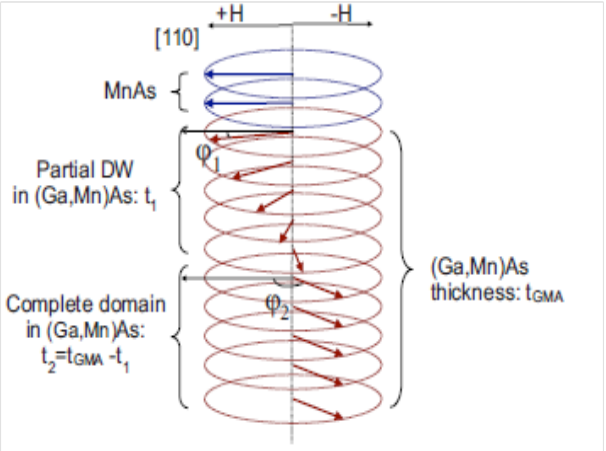

Figure 5.2: Schematic illustration of a partial domain wall configuration (PDW) in GaMnAs, with spins continuously rotating as a function of the distance from the interface[166]

5.2 Description of the exchange spring model of bilayers

Wilson et al.[166] have developed a partial domain wall (PDW) model analogous to the one used by Mauri et al.[106] and Guo et al.[69] to describe exchange biased sytems. The exchange bias field H_E of AFM/FM heterostructure and hard/soft metallic FM bilayers such as MnAs/GaMnAs bilayers can be calculated by this approach. The interfacial exchange coupling in MnAs/GaMnAs bilayers is schematically illustrated in fig.5.2 where a partial domain wall (PDW) is nucleated in the GaMnAs soft layer. In this model the magnetization of the MnAs layer is saturated along the [110] axis of GaMnAs by applying a strong magnetic field in this direction. This direction corresponds to the [11-20] easy axis of magnetization of the hexagonal MnAs layer. When the external field is turned off the MnAs magnetization remains in this easy axis direction whereas the magnetization of GaMnAs layer becomes free to switch back to its equilibrium position.

The PDW of thickness t_1 is formed in the GaMnAs layer close to the interface. When a strong interfacial exchange coupling is assumed, the MnAs magnetization and the GaMnAs magnetization are aligned at the interface, thus $\Phi_1 \approx 0$ and t_1 can be neglected since it is much smaller than the thickness of the GaMnAs t_2 layer. The energy per unit area can be expressed as:

$$E = 2\sqrt{AK}(1 - cos\Phi_2) - A_{ex} + K_u t_{GMA} sin^2\Phi_2$$
$$+1/4 K_c t_{GMA} cos^2 2\Phi_2 - HMt_{GMA} cos\Phi_2 \tag{5.1}$$

The first term is the energy of the PDW where A and K are the spin stiffness and the effective anisotropy constant of GaMnAs, respectively. The second term represents the exchange coupling at the interface. The third and fourth terms are the uni-axial and biaxial anisotropy energies in GaMnAs where K_u and K_c are the uni-axial and biaxial anisotropy constants, respectively. The last term is the Zeeman energy with H the applied magnetic field and M the saturation magnetization of GaMnAs. Assuming a strong cubic anisotropy the energy is minimum at an angle between MnAs magnetization and the bulk GaMnAs magnetization Φ_2=$\pi/4$ and Φ_2=$3\pi/4$. The two switching fields can be determined from the second derivative of the energy with respect to Φ_2.

$$H > H_{C1} = \frac{-2\sqrt{2AK} - 4K_c t}{\sqrt{2}Mt} \tag{5.2}$$

$$H > H_{C2} = \frac{-2\sqrt{2AK} + 4K_c t}{\sqrt{2}Mt} \tag{5.3}$$

The exchange bias field H_E, given by (H_{C1}+H_{C2})/2=-$2\sqrt{AK}$/Mt, is mainly determined by the intrinsic parameters A, K, M and depends inversely on the thickness of the GaMnAs layer. In addition the coercive field H_c, given by (H_{C2}-H_{C1})/2=$8K_c/\sqrt{2}$M, depends on the cubic anisotropy constant and the saturation magnetization of the GaMnAs layer.

5.3 Sample preparation

MnAs/GaMnAs bilayers samples were grown at the Penn State University by the group of Prof. Nitin Samarth. They were deposited by low temperature molecular beam epitaxy (LT-MBE) on a n-type GaAs(001) substrate after the deposition of a 170 nm thick high temperature GaAs buffer layer (grown at 580 °C). In fig.5.3 we show the MnAs/GaMnAs structures. The 30 and 50 nm thick $Ga_{1-x}Mn_xAs$ (x$\sim$0.055) layers are grown at a substrate temperature of $\sim$ 240 °C. After this growth, the substrate temperature is further lowered to 200 °C with the As shutter open. A few monolayers of MnAs are first deposited at 200 °C to form a template for "type-A MnAs." [136]. Then, the substrate temperature is raised to $\sim$240 °C

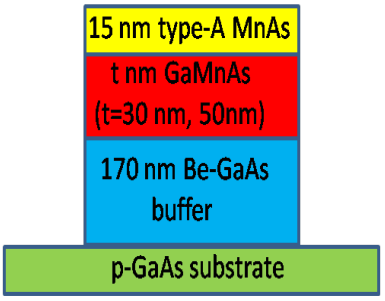

Figure 5.3: Schematic illustration of bilayers structures

to deposit a 15 nm thick MnAs layer. This process produces high quality "type-A MnAs". In this particular epitaxy, the [0001] axis of the MnAs layer lies in the plane of the (001) GaAs substrate and is parallel to the [1-10] GaMnAs axis. The GaMnAs layer has not been annealed purposely but the growth of the MnAs layer at 240°C is expected to indirectly anneal it. Here, we focus on two different samples. Sample A consist with 15 nm type-A on top of 50 nm $Ga_{1-x}Mn_xAs$ (x∼0.055) and Sample B consist 15 nm type-A on top of 30 nm $Ga_{1-x}Mn_xAs$ (x∼0.055). Note that the MnAs layers are very sensitive to oxidation, for this reason we have kept our samples under vacuum between the measurement periods.

5.4 SQUID measurements

The magnetization of the bilayers are measured using a DC SQUID magnetometer. In the SQUID measurements discussed here, the external magnetic field is applied parallel to the [110] direction of the GaAs substrate which corresponds to the [11-20] easy axis of magnetization of the MnAs layer. We show results for sample A but similar results are observed for sample B. We first discuss the magnetization dependence on temperature and magnetic field. The temperature dependence of the remnant magnetization M(T), measured in a field of 30 Oe after cooling down from room temperature in a 1T field, shows clearly two different Curie temperatures for the GaMnAs (T_c =110 K) and MnAs (T_c=320 K) layers (fig.5.4(a)). The saturation magnetizations (M_{sat}) were 28 emu/cm^3 and 666.6 emu/cm^3 for GaMnAs and MnAs respectively. Fig.5.4(b) shows the major magnetization hysteresis loop measured after first saturating the MnAs layer in a field of 20 kOe. We observe very different coercive fields for MnAs ($H_c \sim$ 1.4 kOe) and GaMnAs ($H_c \sim$ 500 Oe).

Fig.5.5 (a),(b) shows the minor hysteresis loop measured over a field range -1kOe≤H≤ 1kOe after first saturating the MnAs layer in a field of +20 kOe and -20

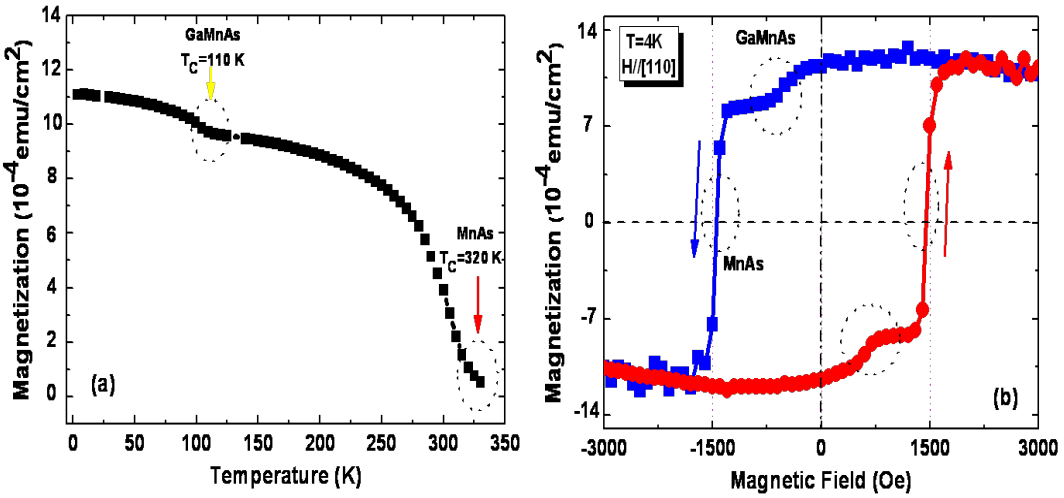

Figure 5.4: (a) Temperature-dependent magnetization M(T)(b)Major hysteresis loop M(H) at 4 K for a bilayer sample, showing two distinct coercive fields of the GaMnAs and MnAs layers. The magnetization is shown per unit area.

kOe respectively. We note that the minor loop of the bilayers is the major loop of the GaMnAs layer. The displacement of the center of the hysteresis loop from zero field is opposite to the magnetization of the MnAs layer (a positive or negative ~ 340 Oe) indicates that the MnAs and GaMnAs layers are FM coupled, whereas a parallel alignment of two layers evidences "negative exchange biasing" of the GaMnAs layer. With the experimental values of M=28emu $/cm^3$,K $\approx K_c/4 \approx 2672$ erg$/cm^3$ (in fig.5.8), t=50 nm at T=4K, we obtain the spin stiffness A=0.5 pJ/m for the GaMnAs layer which is consistent with theoretical calculation by Sugawara et al.[151].

In fig.5.5(a) we show the minor hysteresis loop at several temperatures. We find that the coercive field H_c and the exchange bias field H_E decrease up to the Curie temperature T_c (fig.5.5(b)). Previous studies of ferromagnet films exchange biased by an anti-ferromagnet layer have shown that the H_E decreases with increasing temperature; in fact both fields H_E and H_c are correlated [45, 46]. However, Wilson et al.[166] have observed no variation with temperature of H_E for high doping Mn concentration (x=0.16). It should be recalled that the PDW model predicts that the anisotropy and magnetization depend on H_c and H_E. The anisotropy constants and magnetization of GaMnAs are a function of temperature, decreasing with increasing temperature [31].

In fig.5.7 we show that the exchange field H_E decreases with increasing thickness

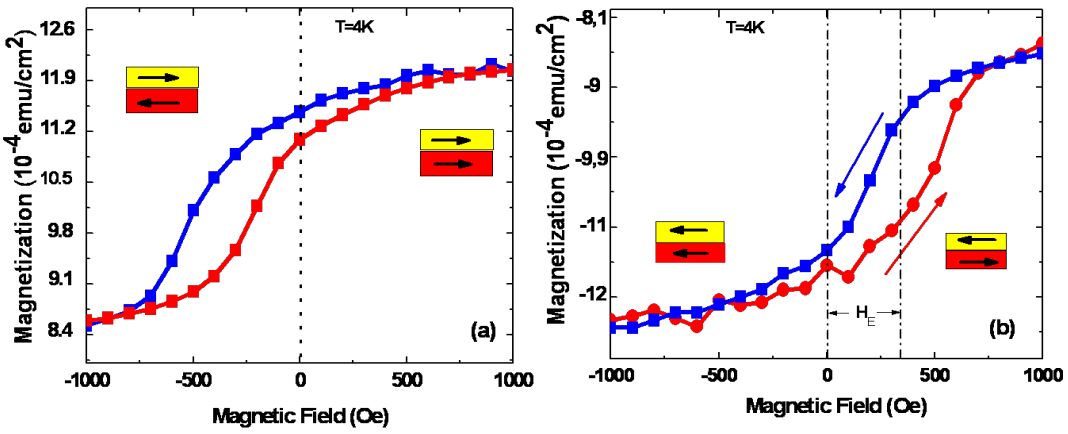

Figure 5.5: Minor hysteresis loop at 4K after saturation of the MnAs layer at +20 kOe (a) or -20 kOe (b) The minor loops are seen to shift to the opposite direction of the MnAs magnetization by a field which is called exchange field H_E. The orientations of the two layers are also shown.

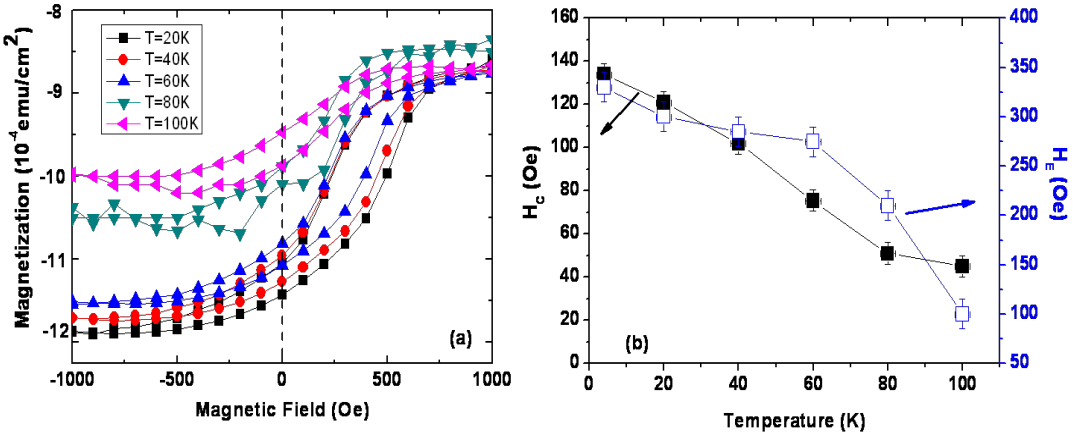

Figure 5.6: (a)Minor hysteresis loop at several temperatures for sample A after saturating the MnAs at -20 kOe (b) The exchange field H_E as a function of temperature.

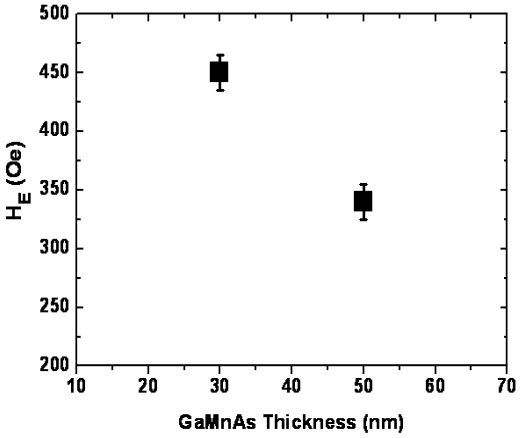

Figure 5.7: The exchange field H_E as a function of GaMnAs thickness

of the soft layer GaMnAs. Similar results have been observed on a different samples MnAs/GaMnAs layers[175, 166]. Our results are in good agreement with the PDW model.

Metal/GaMnAs bilayer are systems of high current interest as they may be used to increase the Curie temperature of GaMnAs up to room temperature. Recent studies of Fe/GaMnAs bilayers have shown an antiferromagnetic coupling between Fe and Mn in the near surface regions of GaMnAs. The effect induced by the presence of the Fe cap layer, persists even above room temperature as deduced from X-ray magnetic circular dichroism (XMCD) measurements. However, SQUID measurements have not given direct evidence for such an effect [99, 117]. Note that via SQUID measurements it is difficult to evidence a small magnetized fraction of the GaMnAs layer near the interface which might be coupled to the MnAs layer due to its small thickness and thus small contribution to the total SQUID signal.

5.5 FMR measurements

The FMR measurements on the MnAs/GaMnAs bilayers were performed at different frequencies in the 4 K to T_c temperature range.

5.5.1 9.5 GHz(X-Band) measurements

The angular dependences of the GaMnAs FMR spectra were measured in two different planes of GaMnAs: (001) and (1-10) at 9.5 GHz (X-Band). In this setup,

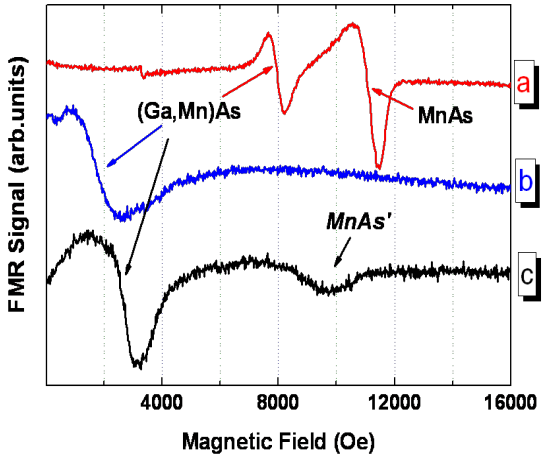

Figure 5.8: FMR spectra at T=4 K for H||[001] (a), H||[1-10] (b) and H||[110] (c) of the MnAs/GaMnAs bilayer at a frequency of 9.5GHz. The low intensity MnAs spectrum in (c) results from a fraction of the MnAs layer with a different orientation as compared to the main alpha phase, characterized by an in-plane intermediate axis

the maximum available magnetic field H is 17.8 kOe. These two sets of measurements enable us to determine the resonance position for the high symmetry orientations of the GaMnAs film: H||[001], [110], [1-10] and [100] from which the anisotropy constants can be determined [97].

In Fig. 5.8, we show typical X-band FMR spectra of the bilayer for H||[001], H||[1-10] and H||[110] at T = 4 K. For H||[001] (fig.5.8a), we observe both the uniform mode of the GaMnAs and the one of the MnAs layer. They can be easily distinguished and attributed due to their different angular variations, intensities and temperature dependence. For H||[1-10] (fig.5.8b) i.e., parallel to the hard axis [0001] of MnAs only the GaMnAs spectrum can be observed in the available magnetic field range. For this orientation the resonance field for the MnAs spectrum is expected to be close to 3T. For H||[110](fig.5.8c), the easy axis of magnetization of the MnAs layer, the MnAs spectrum can not be observed neither at X-band spectroscopy as the microwave energy is too low; its observation requires at least Q-band (35GHz) frequencies. We observe nevertheless a weak spectrum at the resonance position close to the intermediate axis orientation, which we attribute to the fact that a small fraction of the MnAs film has a different, $\approx 90^\circ$ rotated crystallographic orientation. Such mixed epitaxies occur frequently in MnAs layers on GaAs(001).

The line-widths of the GaMnAs spectra are highly increased as compared to

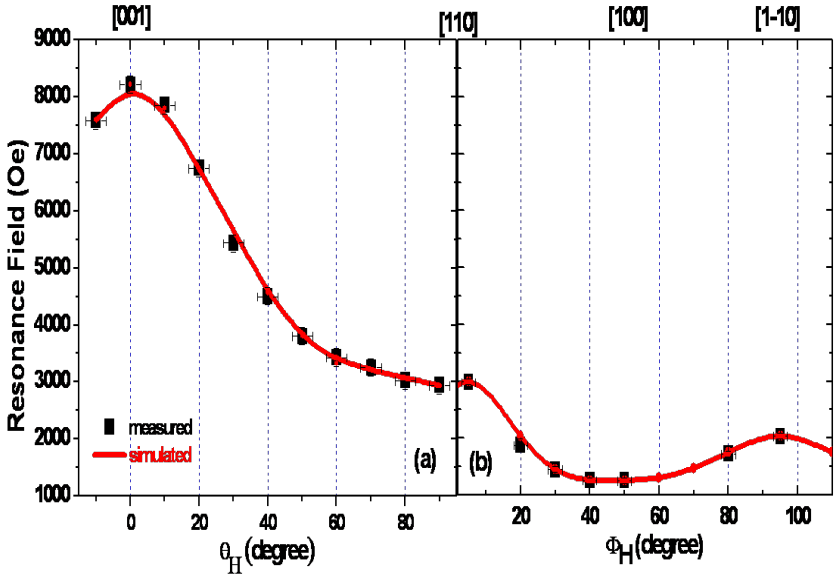

Figure 5.9: The resonance field of the FMR uniform mode of the GaMnAs layer at 4K (squares) for sample A and the simulated angular variation (solid lines, red) as a function of different orientation of applied field in out-of plane configuration(a) and in-plane configuration(b).

the values observed in layers without a MnAs cap layer. In particular for the in-plane orientation typical line-widths of single layers of GaMnAs are in the 100 to 200 Oe range, whereas in these bilayers they increase up to 2000 Oe. An increase of the linewidth can be due to different mechanisms such as strongly reduced hole concentrations, increased Gilbert damping factors in bilayer systems or magnetic inhomogeneities. It seems reasonable to attribute the major contribution to the multidomain structure of the MnAs layer which are characterized by coercive fields above 1T for the hard in-plane axis. The high critical temperature of 110 K for the GaMnAs layer indicates a hole concentration of $> 10^{20}$ which are to high to explain this increase in linewidth [83].

The angular variation of the GaMnAs FMR spectra was measured at temperatures between 4 K and 110 K and the anisotropy constants have been determined by the standard procedure [97, 146, 83]. In fig.5.9 we show the angular variation of the "out-of plane" and "in-plane" configuration at 4K.

We observe the usual in-plane [100] easy axis and [001] hard axis orientation. However, the dominant uniaxial constant $K_{2\perp}$ is strongly reduced and the cubic con-

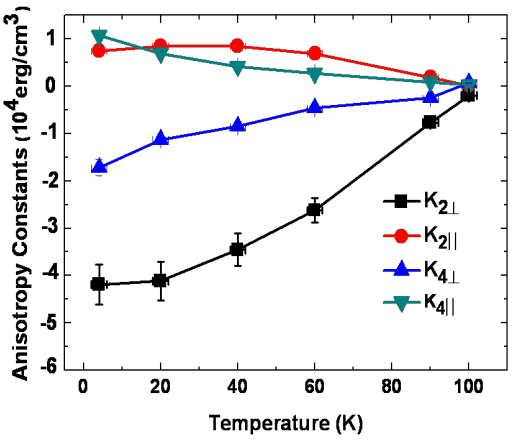

Figure 5.10: Variation of the four magnetocrystalline anisotropy constants $K_{2\perp}$ (black,square), $K_{2\parallel}$(red,circle), $K_{4\perp}$(blue,upper triangle) and $K_{4\parallel}$(green,lower triangle) as a function of temperature for the MnAs capped GaMnAs/GaAs layer. The symbols are experimental results; lines are guides for the eyes.

stant $K_{4\perp}$increased as compared to comparable standard layers (Fig. 5.10) [83, 32]. The growth of the MnAs layer on top of the GaMnAs layer seems to modify the strain dependent anisotropy constants [37] from those of comparable, uncapped layers. Exchange coupling between MnAs/GaMnAs bilayers can also shift of resonance positions of the GaMnAs spectra [29] which might modify the apparent anisotropy constants of GaMnAs.

In principle, it is also possible to study the exchange coupling of two layers by FMR via the resonance field shifts of the GaMnAs layer if parallel and anti-parallel magnetization orientations can be realized. However, this appears to be precluded in this case since the resonance field for GaMnAs is comparable to the coercive field of the easy axis of MnAs. Indeed, the SQUID major loop measurements with H$\|$[110] show that the MnAs layer is already fully magnetized for H=1.4 kOe whereas the FMR resonance field of the uniform mode in GaMnAs occurs at a higher field of 2.5 kOe. Thus, a field reversal will always lead to parallel oriented magnetizations in both layers and consequently no shift in the resonance fields will be observed.

5.5.2 35 GHz(Q-Band) measurements

In fig.5.11, we show Q-band FMR spectra of the MnAs/GaMnAs layer measured at different temperatures; the motivation for Q-band measurements is that the easy

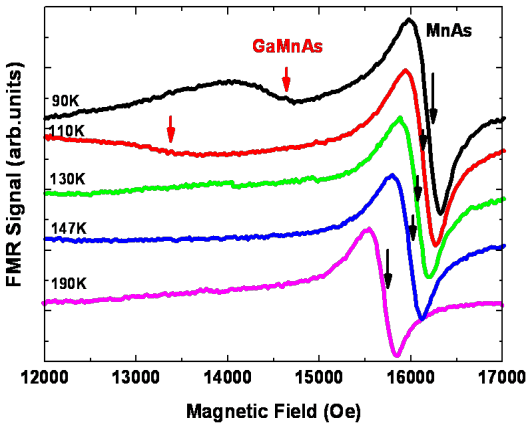

Figure 5.11: FMR spectra at several temperatures for H||[001] MnAs/GaMnAs bilayer at a frequency of 35GHz. The arrows indicate the resonance field of the GaMnAs and MnAs layers

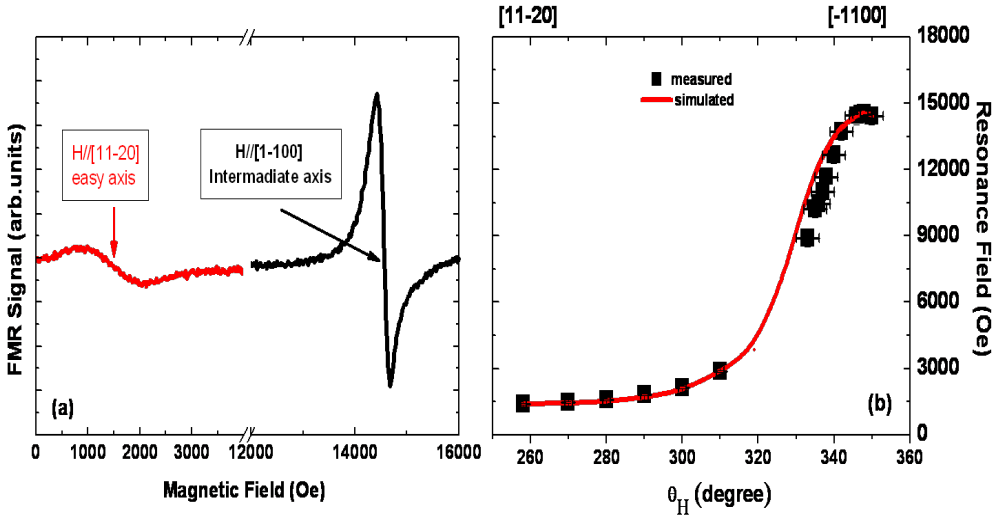

Figure 5.12: (a)FMR spectra at 260K for H||[11-20](left,red), H||[-1100](right,black) MnAs layer at a frequency of 35GHz. The arrows indicate the resonance field of the MnAs layer. (b) The resonance field of the MnAs layer at 260K (squares) and the simulated angular variation (solid lines, red) as a function of different orientation of applied field in the out-of plane configuration (i.e. from the intermediate axis H|| [-1100] to the easy axis H||[11-20]

axis FMR spectra can now be observed at intermediate temperatures. For a magnetic field applied H‖[001]. We observe two distinct FMR spectra which can be attributed to the uniform mode spectra of the GaMnAs layer and the MnAs layer respectively.

In fig.5.12(a) we show the typical FMR spectra at 260K for the easy axis H‖[11-20] and intermediate axis of the magnetization H‖[1-100] of the MnAs layer at a frequency of 35GHz. We observe the intermediate axis resonance at 14550 Oe and the easy axis resonance at 1510 Oe. However, we have not observed the easy axis resonance at lower temperature at this frequency as it shifts to negative field values. The angular dependence of the resonance field at 260K in the out-of plane configuration is shown in fig.5.12(b). We obtain a good agreement between the simulated resonance field and the measured ones.

5.5.2.1 Phase Transitions in ultrathin MnAs layer

Thin epitaxial layers of MnAs grown epitaxially on GaAs(001) or GaMnAs have been intensely investigated recently due to the particular phase transitions in the 270K to 300K range which lead to the formation of a stripe system composed of ferromagnetic alpha stripes separated by paramagnetic beta phase regions[25, 122, 81, 94, 25]. The details of the magnetic domain structure of the MnAs layers depend on the thickness of the MnAs layer. For 25 nm thick layers Ryu et al. [133] have shown by magnetic force microscopy (MFM) closed domain structures spreading across some FM stripes(fig.5.13). In fig.5.14(a,b), we show the FMR resonance spectra measured close to the α/β phase transition their temperature dependence in the range from 65 K to 301 K; the magnetic field is applied parallel to the [1-100]axis. We observe two FMR spectra between 294 K and 301 K. The spectrum at higher field is the one of the striped α phase and the spectrum at lower field is related to the remaining fraction of the alpha phase in non-striped region of the layer.

In fig. 5.15 we show that the FMR linewidth is also sensitive to the phase transition; it increases strongly above 270 K due to spin fluctuations. As the stripes have no simple geometrical shape in these ultrathin MnAs films a quantitative analysis of the FMR spectra with the consideration of the modified shape anisotropy is not possible.

5.5.3 High Frequency -115GHz- FMR measurements

The ferromagnetic α phase of both bulk MnAs and epitaxial MnAs layers on GaAs has been studied in the past by a number of experimental techniques. The first

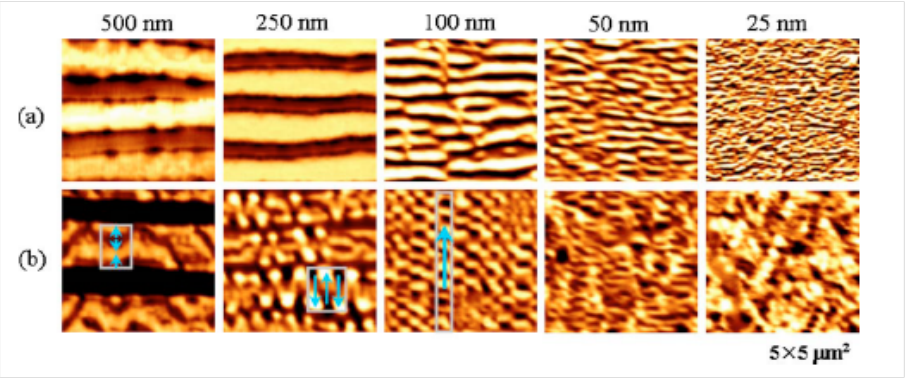

Figure 5.13: Variation of the MFM images for MnAs film with decreasing thickness at (a) saturated state and (b) demagnetized state. The images have observed at room temperature and the easy axis is perpendicular to the FM stripe direction[133]

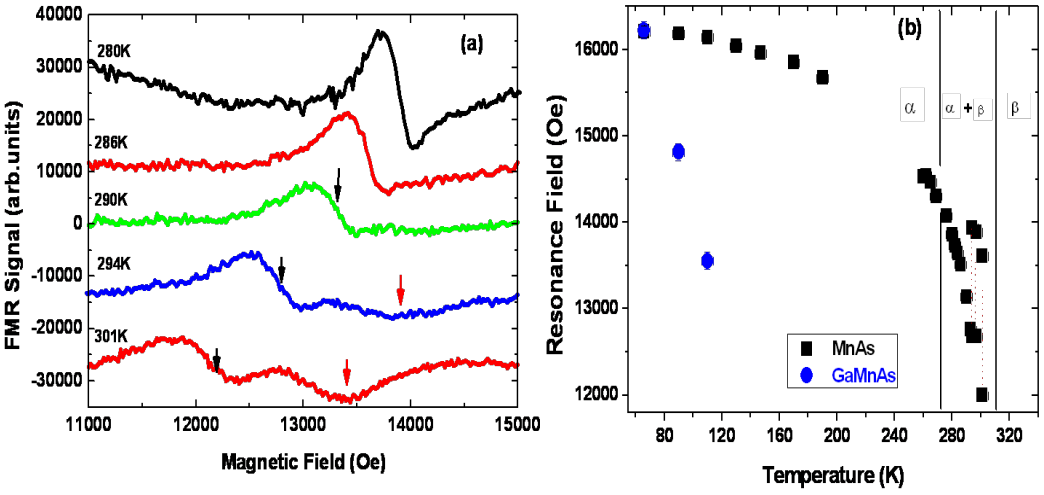

Figure 5.14: (a) FMR spectra close to the transition between α phase and the striped α-β phase measured in the direction normal to the film (i.e. H$\|$[1-100]).(b) Temperature dependence of the resonance field measured in the direction H$\|$[1-100] MnAs layer. The dashed lines represent the transition temperature between the α phase, the striped α-β phase and the β phase.

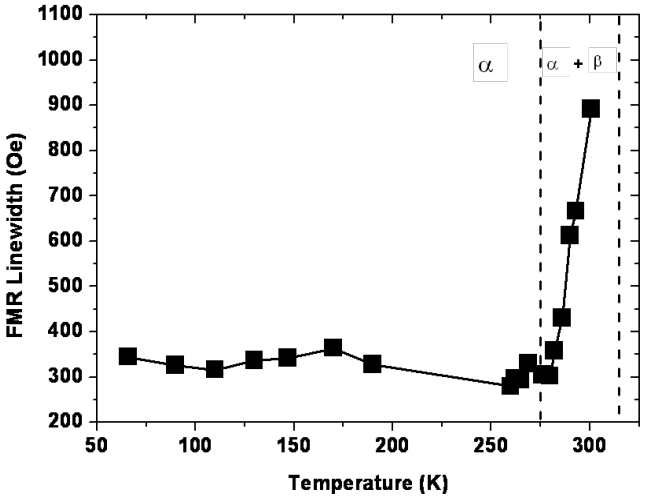

Figure 5.15: Temperature dependences of the linewidth of the FMR spectrum of the alpha phase of MnAs measured in the direction [1-100].

results on bulk single crystals have been obtained by De Bois and Rodbell[13]. Their studies concerned the mechanism of the FM long range order, the determination of the saturation magnetization and the high intrinsic uni-axial anisotropy linked to the hexagonal crystal structure. The exceptionally high magneto-crystalline anisotropy is at the origin of the experimental difficulty to measure this anisotropy and its strain induced modifications by FMR spectroscopy. In particular with X-band and Q-band spectrometers;

- the easy axis not observable at low temperature
- the hard axis not observable
- the Magnetization is not saturated at the resonance fields of the intermediate axis [147]

To overcome these difficulties, we have performed high frequency FMR measurements at the Grenoble High Magnetic Field Laboratory. We have investigated the magneto crystalline anisotropy of epitaxial MnAs layers grown on GaAs by high frequency FMR at 115GHz with magnetic fields up to 12T. At this frequency the g=2 resonance field is close to 4T. In a typical FMR experiment we measure the angular variation of the resonance fields of the uniform mode for orientations of the applied magnetic field in two crystal planes. The geometry is described in polar coordinates with the polar and azimuthal angles Θ and Φ. A particularity of the high anisotropy is the extreme non collinearity of the applied magnetic field and the

equilibrium magnetization.

The resonance positions of the uniform mode spectra can be derived from the free energy density F[94] and its derivatives relative to Θ and Φ in the Smit Beljers formalism [146]. It contains the Zeemann term, the shape anisotropy and the magnetocrystalline anisotropy. The free energy density for MnAs layers on GaAs(001) is:

$$\begin{aligned} F = -HM(sin\Theta sin\Theta_H cos(\Phi - \Phi_H) + cos\Theta cos\Theta_H) \\ -(K_1 - \tfrac{N_b}{2}M^2)cos^2\Theta - (K_2 - \tfrac{N_a}{2}M^2)sin^2\Theta cos^2\Phi \end{aligned} \tag{5.4}$$

where Θ and Θ_H are the polar angle of the magnetization and the external field with respect to the MnAs[-1100]-axis, i.e., to the normal plane (b-axis) respectively, whereas Φ and Φ_H are the in-plane angle taken relative to the MnAs[11-20]-axis, i.e., easy axis (a-axis), K_1 and K_2 represent the out-of plane and in-plane anisotropy constants respectively, the N_i (i=a,b) are the demagnetizing factors of the stripes along a- and b-axis. For a homogeneously magnetized α phase-MnAs film we have a simple thin film geometry and the demagnetizing factors are N_a=0 and N_b=4π.

Using eq.5.4 and the Smit Beljers formalism[146], the resonance equation for the polar angular dependency assuming Φ_H=0°is given by:

$$\begin{aligned} \left(\frac{\omega}{\gamma}\right)^2 = [Hcos(\Theta - \Theta_H) - (M_{eff}^{\perp} - M_{eff}^{\parallel})cos2\Theta] \\ \times[Hcos(\Theta - \Theta_H) - (M_{eff}^{\perp} - M_{eff}^{\parallel})cos^2\Theta - M_{eff}^{\parallel}] \end{aligned} \tag{5.5}$$

where $M_{eff}^{\perp}$=N_bM-$\dfrac{2K_1}{M}$ and $M_{eff}^{\parallel}$=N_aM-$\dfrac{2K_2}{M}$.

Simultaneously, the equilibrium condition F_Θ=0 (free energy derivative with respect to Θ) has to be fulfilled, i.e.:

$$Hsin(\Theta - \Theta_H) = \frac{1}{2}(M_{eff}^{\perp} - M_{eff}^{\parallel})sin2\Theta \tag{5.6}$$

5.6 High Frequency FMR spectroscopy of 15nm thin MnAs epilayers grown on GaMnAs(001)

The angular variation of the FMR spectra has been measured for a rotation from the intermediate axis to the easy axis and from the intermediate axis to the hard

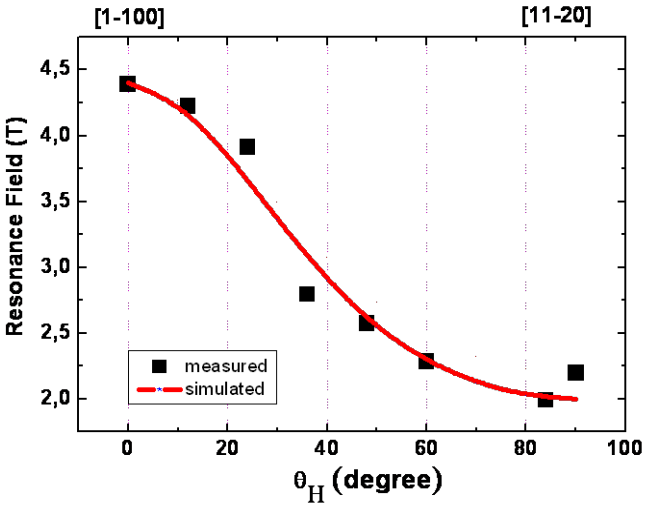

Figure 5.16: Angular variation of the resonance field (squares) of the FMR spectra of the MnAs layer; T=160K. The simulated angular variation from eq. 5.5is shown (solid lines, red). The applied field is changed from the intermediate axis H‖[-1100](Θ=0) to the easy axis H‖[11-20](Θ=90)

axis both being out-of-plane configurations. Due to the maximum field of 12T even the hard axis uniform mode spectrum could be measured.

In fig.5.16 we show the angular variation of the uniform mode resonance fields for the first case. The measurement temperature was 160K; at this temperature the MnAs layer is in the single α phase and the GaMnAs layer paramagnetic. We observe resonance fields of 4.4 T and 2.0 T respectively for the intermediate and easy axis orientation of the applied magnetic field. In the second configuration the hard axis resonance field is 7.8 T. The physically relevant parameters are the anisotropy constants which we obtain via the resonance equations and the knowledge of M, determined independently from SQUID measurements.

5.6.1 Magnetic Anisotropy of MnAs thin films on GaMnAs(001)

The anisotropy constants for the MnAs layer on GaMnAs/GaAs(001) determined from the high frequency FMR measurements using eq.5.5 are given in Table 5.6.1. There are a number of important observations:

– The anisotropy constants are not identical for out-of plane and in-plane ori-

T(K)	M(emu/cm^3)	K_1(erg/cm^3)	K_2(erg/cm^3)
160	627	6.6x10^6	8.8x10^6
260	500	3.3x10^6	3.7x10^6
301	260	1.5x10^6	1.8x10^6

Figure 5.17: Values of the Magnetization and anisotropy constants at T=160K, T=260K and T=301K

entations. This demonstrates that the simple model of a relaxed layer is not correct.

- We observe that the difference between the two constants increases when the temperature is lowered. The layers become more and more biaxially strained at low temperature.
- The difference of nearly 2x10^6 erg/cm^3 is very high; for comparison, typical anisotropy constants of strained epitaxial GaMnAs films on GaAs are an order of magnitude smaller.
- the numerical values of the constants increase at low temperature, as expected.
- if we compare the value of uni-axial anisotropy K_1 to the bulk value (11x10^6) [13], we observe that the epitaxial layers are under tensile strain. Note that this strain exists in the pure α phase and might even induce β phase formation at unexpectedly low temperature.

5.7 High Frequency FMR spectroscopy of thin MnAs epilayers grown on GaAs(111)

We extended our FMR studies also to the case of ultrathin MnAs layers epitaxialy grown on (111) oriented GaAs substrates. For this epitaxy the hard axis of MnAs is oriented perpendicular to the film plane and the in-plane properties of the layer are isotropic in a first order approximation. In this section we present the results of epitaxial MnAs layers of $\approx$ 10 nm thickness grown on GaAs(111) by molecular beam epitaxy at 250°C. A typical high FMR (115GHz) spectrum is shown in figure 5.18. Remarkable is the unexpected small linewidth of only 120 Oe which expresses an excellent crystallographic quality and as shown later, a small Gilbert damping factor.

We show in fig.5.19 the angular variation of the uniform mode resonance fields.

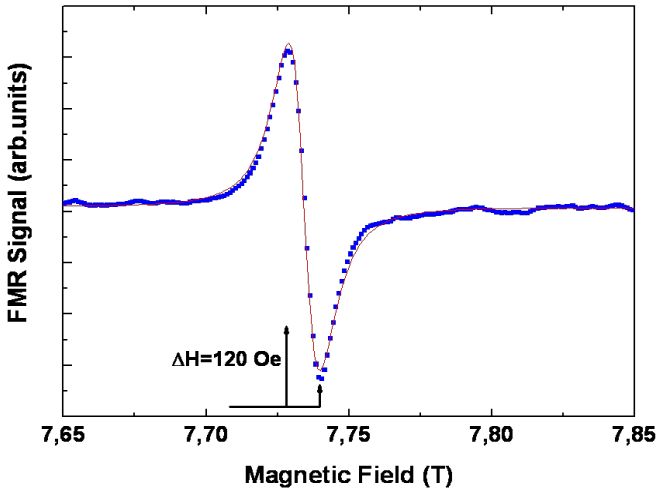

Figure 5.18: FMR spectrum measured at 200K in the direction hard axis H‖[0001] at a frequency of 115 GHz

The hard axis resonance is at 7.7 T and the easy axis resonance at 2.7 T. At such high magnetic fields, we observe the FMR spectra of a homogeneously magnetized film, a condition always assumed in the standard Smit Beljers analysis.

Whereas in a first order approximation, the in-plane angular variation of the FMR spectra not show any angular dependence higher order terms can however introduce a small sixfold angular variation reflecting the hexagonal crystal structure. If the epitaxy is not fully homogenous over the mm^2 sized sample this additional small anisotropy will be hidden. To test this and determine this additional constant we have measured this variation at Q-band (35GHz) at 200K. As shown in fig.5.20 we do indeed observe a sixfold variation but the anisotropy is small, of the order of 30 Oe only.

We derived the anisotropy constants using the Free energy density F[20] and its derivatives relative to Θ and Φ in the Smit Beljers formalism [146].

The Free energy density F for hexagonal films with the c-axis perpendicular to the film plane have been given by Chappert et al. We use their equations adapting it to our notation of the polar and azithumal angles:

$$F = -HMsin\Phi cos(\Theta_H - \Theta) + \frac{1}{2}(4\pi M^2)sin^2\Phi$$
$$-(K_1 + 2K_2)sin^2\Phi sin^2\Theta + K_2 sin^4\Phi sin^4\Theta \tag{5.7}$$

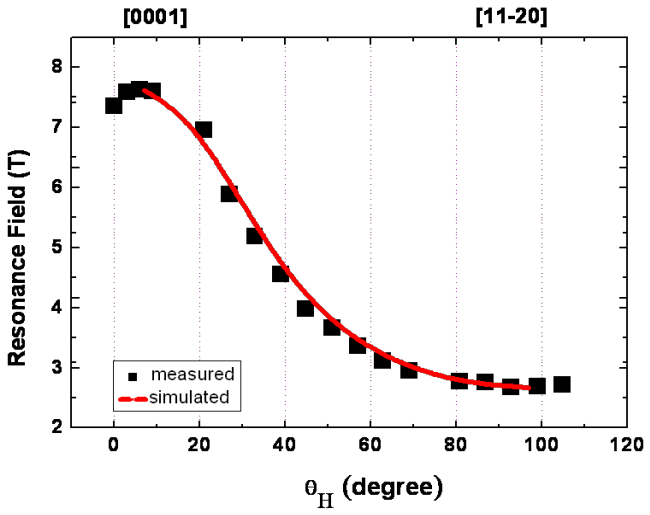

Figure 5.19: The resonance field of MnAs layer at 200K (squares) and the simulated angular variation (solid lines, red) in the out-of plane configuration (i.e., the applied magnetic field is changed from the hard axis H||[0001] to the easy axis H||[11-20]; microwave frequency 115GHz

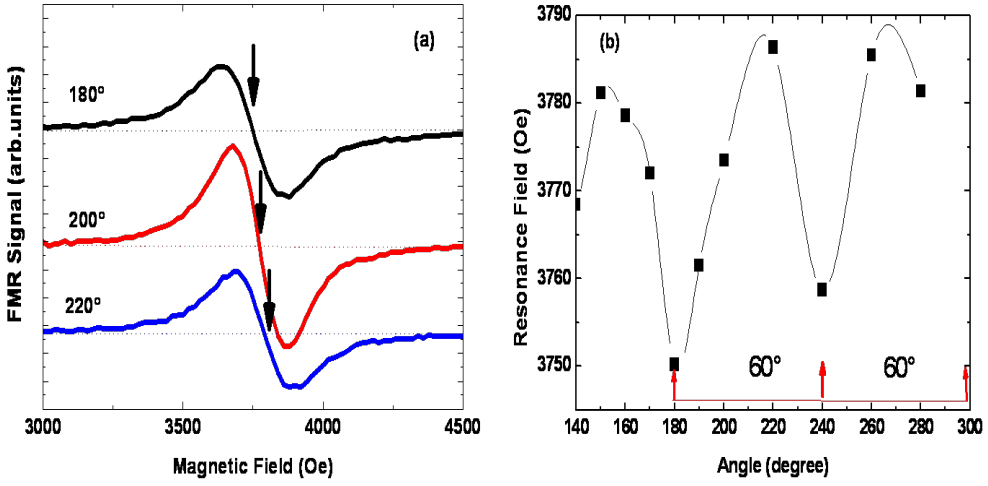

Figure 5.20: (a) FMR spectra at 200K for different orientations of the applied field in the film plane at a frequency of 35GHz (b) The resonance field at 200K (squares) in in-plane configuration at a frequency of 35GHz (Q-band). Lines are guide for the eyes

where the first term represents the Zeeman energy, the second the magnetostatic energy, and last two term the axial anisotropy energy with c axis parallel to perpendicular to the layer. K_1 and K_2 are the uni-axial out-of plane and uni-axial in-plane anisotropy constants respectively.

The resonance equation for the polar angular Θ dependency is given by:

$$\left(\frac{\omega}{\gamma}\right)^2 = [Hcos(\Theta_H - \Theta) + (4\pi M - \tfrac{2K_1}{M})cos2\Theta + \frac{4K_2}{M}(3sin^2\Theta cos^2\Theta - sin^4\Theta)]$$

$$\times[Hcos(\Theta_H - \Theta) - (4\pi M - (\frac{2K_1}{M} + \frac{4K_2}{M}))sin^2\Theta - \frac{4K_2}{M}sin^4\Theta] \tag{5.8}$$

where Θ and Θ_H represent the polar angle of the magnetization and the external field respectively.

At the temperature of 200K, we obtained following values for K_1=-10.56x10^6 erg/cm^3 and K_2=-1,4x10^5 erg/cm^3.

In fig.5.21 we compare our results to the previously published values of the uni-axial anisotropy K_1 constants. The blue triangle corresponds to a previous X-band measurement by Repetto et al.[92]. These authors had only observed at X-band the uniform mode spectrum for a very limited magnetic field range between 0 Oe and 1.5 kOe which raises a number of problems. The second value given by Steren et al.[147] (green triangle) has been determined from SQUID magnetization measurements. Our results (red circles) are in excellent agreement with the ones published by De Blois et Rodbell [13] for bulk samples which indicates that the strain in these layers on GaAs(111) is probably very small.

The phenomenological Gilbert damping factor α allows to parametrize the relaxation of the magnetization; it can be deduced from FMR measurements at least two frequencies. It is the frequency dependence of the uniform mode linewidth (fig.5.22) which allows its determination. The FMR linewidth is generally decomposed in a frequency independent term corresponding to an inhomogeneous broadening (obtained by extrapolation to zero frequency) and a linear term corresponding to the homogeneous broadening. Here we have used two measurements at 115 GHz and 230 GHz for its determination. It would have been interesting in order to increase the precision of this value to dispose of more than two frequencies but this was not possible in these experiments. As shown in fig.5.22, we deduce from the two measurements a damping factor of α=0.002. This is the first determination of the damping factor in epitaxial MnAs films. Its value is comparable to the one determined for Fe

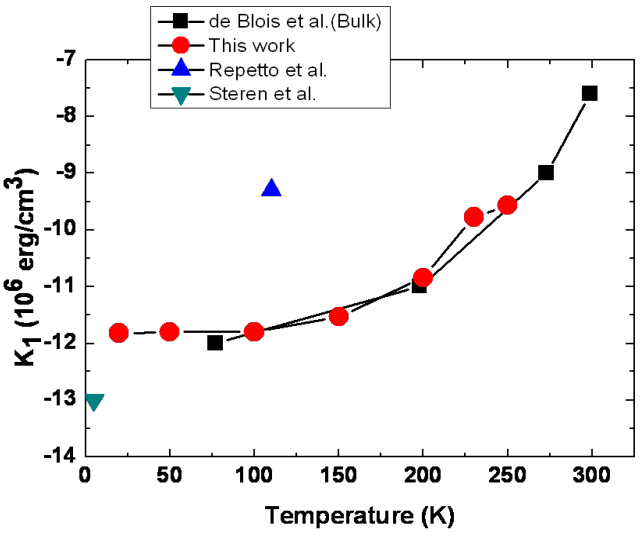

Figure 5.21: Uniaxial anisotropy constants K_1 MnAs/(111)GaAs as a function of temperature, determined from 115GHz FMR measurements and literature values previously published

thin films.

5.8 Conclusion

In this chapter we have presented a number of magnetization measurements and FMR measurements of MnAs/GaMnAs and MnAs/GaAs bilayers. The coupling of two ferromagnetic bilayers such as Fe/GaMnAs[99, 117] or Fe/MnAs [134, 15] is of high current interest. We observe at low temperatures a ferromagnetic coupling between the MnAs and GaMnAs layers characterized by an exchange field of 350 Oe. This value is interpreted in a partial domain wall model. Whereas the domain wall model limits the coupling to a small interface region we observe a strong perturbation of the GaMnAs FMR spectra by the MnAs top layer. It is characterized by an extreme line broadening for the in-plane orientation. FMR measurements of the magnetic anisotropies of MnAs thin films even in the low temperature alpha are difficult due to the high intrinsic anisotropy of MnAs thin films which preclude the observation of the angular variation due to the limitation of the available magnetic field ranges. Our high frequency measurements have allowed us to follow the complete angular variations. From these results we could determine the anisotropy constants for both GaMnAs/GaAs(001) and GaAs(111) epitaxies. Our results show

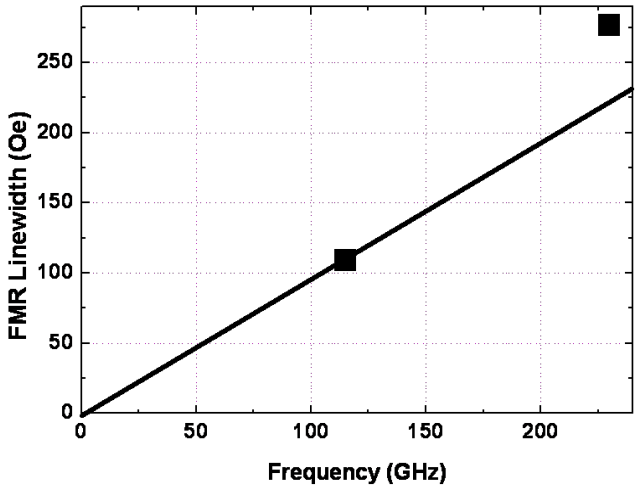

Figure 5.22: High frequency FMR linewidth at 115GHz and 230GHz for the MnAs/GaAs(111) film; T=200K and H||[0001]

the presence of an unexpected important strain in the (001) epitaxies and confirm the first publication of this value by De Blois et Rodbell [13]. We have equally been able to give a first estimation of the Gilbert damping factor by 115Ghz and 230GHz measurements.

Chapter 6

Spin relaxation in Magnetic Semiconductor Layer

The dynamics and relaxation processes of the magnetization of ferromagnetic semiconductor layers have been investigated in the last few years [145, 104, 167]. Previous FMR studies focussed either on unusually low doped GaMnAs layers [145, 167] or were performed on standard layers but with the limiting condition of a single microwave frequency [145]. Recently, we have investigated by FMR at X-band and Q-band frequencies the damping of compressive and tensile strained GaMnAs thin films grown on GaAs and GaInAs substrates respectively [84]. The knowledge and control of the relaxation processes are of particular importance for device applications as they determine for example the critical currents required for the magnetization switching in FM/NM/FM trilayers [145]. In this chapter we present the results of similar FMR studies of the magnetization relaxation in $Ga_{1-x}Mn_xAs_{1-y}P_y$/GaAs layers with different Phosphorous concentrations. We also investigated the anisotropy of the magnetization relaxation process in these layers.

6.1 Magnetization relaxation; Gilbert Damping

The damping factor α is generally assumed to be a scalar quantity [57, 72]. It can be determined from FMR or Kerr effect measurements, these two techniques probing the relaxation phenomenon in two different regimes. The FMR spectroscopy measures the magnetization relaxation for small angle precession in a homogeneously magnetized thin film. On the contrary, large precession angles are involved in magnetization reversal processes in domain wall motion generally studied by MOKE

spectroscopy. The value of the Gilbert damping factor α determined by Kerr spectroscopy is usually higher than the one determined by FMR ($\alpha_{DW} > \alpha_{FMR}$) but the two can be related theoretically[21, 74].

The Gilbert damping fctor for the magnetization precession in the small angle regime is defined by the Landau-Lifschitz-Gilbert (LLG) equation to which now a damping term is added[89, 93],

$$\frac{1}{\gamma}\frac{d\overrightarrow{M}}{dt} = -[\overrightarrow{M} \times \overrightarrow{H}_{eff}] + \frac{\alpha}{\gamma}[\overrightarrow{M} \times \frac{d\overrightarrow{s}}{dt}] \tag{6.1}$$

where M is the magnetization, H_{eff} is the effective magnetic field, α is the damping factor, γ is the absolute value of the electron gyromagnetic ratio and s is the unit vector in the direction of M.

The Gilbert damping factor α has been modelled for ferromagnetic GaMnAs thin films by Sinova et al[145]in the framework of the mean field kinetic exchange model:

$$\alpha = \frac{J_{pd}h_{eff}}{4\hbar}\int\frac{d^3k}{(2\pi)^3}\sum_{a,b}|<\phi_a(\mathbf{k}) \mid s^+ \mid \phi_b(\mathbf{k})>|^2 \times A_{a,\mathbf{k}}(\epsilon_F)A_{b,k}(\epsilon_F) \tag{6.2}$$

where h_{eff}=J_{pd} N_{Mn} $< S >$ is an effective kinetic-exchange field, J_{pd} is the exchange integral, N_{Mn}=4x/a_{lc}^3 is the density of uniformly distributed Mn ions in $Ga_{1-x}Mn_xAs$(a_{lc} is the GaAs lattice constant), $\phi_a(\mathbf{k})$ is the band eigenstates and $A_a(\epsilon, \mathbf{k})$ is the spectral function.

In the DMS systems where the magnetic properties are introduced by doping like GaMnAs, the spin orbit interaction is strong and high values of damping factor α are expected, as compared metallic system like Co, Fe and MnAs.

6.1.1 FMR linewidth

The Gilbert damping factor can be experimentally determined by FMR spectroscopy from the variation of the uniform mode linewidth $\triangle H_{pp}$ with the microwave frequency [163, 143];

$$\triangle H_{pp}(\omega) = \triangle H_{inhom} + \triangle H_{hom} = \triangle H_{inhom} + \frac{2}{\sqrt{3}}\frac{G}{\gamma^2.M}\omega \tag{6.3}$$

where $\triangle H_{pp}$ is the peak-to-peak linewidth of the first derivative of the uniform mode resonance (Lorentzian line shape), ω is the angular microwave frequency, and G is the Gilbert damping factor from which magnetization-independent damping factor α can be deduced by α=G/γM. In Eq.6.4 it is assumed that the magnetization

and the applied magnetic field are colinear; this is fulfilled for the high symmetry directions in GaMnAs: [001], [110, [1-10] and [100]. Otherwise a $1/\cos(\theta\text{-}\theta_H)$ term has to be added to Eq.6.4 [57]. $\triangle H_{inhom}$ is the inhomogeneous, frequency-independent linewidth; it can be further decomposed in three contributions, related to the crystalline imperfections of the film [20]:

$$\triangle H_{inhom} = \mid \frac{\delta H_r}{\partial_H} \mid . \triangle \theta_H + \mid \frac{\delta H_r}{\delta \phi_H} \mid . \triangle \phi_H + \mid \frac{\delta H_r}{\delta H_{int}} \mid . \triangle H_{int} \qquad (6.4)$$

The first two terms are introduced to take into account a slight mosaic structure of the metallic films defined by θ and ϕ and their distributions ($\triangle\theta$,$\triangle\phi$) and the third term takes into account a distribution of the internal anisotropy field H_{int}. For epitaxial III-V films grown by MBE like GaMnAs or GaMnAsP on GaAs, high quality films without any mosaic structure are obtained and, in this case, only the third term may play a role.

The Gilbert damping factor can thus be determine by measuring $\triangle H_{pp}$ at different frequencies (values of ω). The variation of the FMR linewidth with microwave frequency has been measured with resonant-cavity systems at 9 GHz (X-band) and 35 GHz (Q-band) in the 4K to Tc temperature range and for different orientations of the applied magnetic field. The peak-to peak linewidth of the uniform mode FMR spectrum is then decomposed into a frequency independent inhomogeneous linewidth, and a frequency (linearly) dependent linewidth. The inhomogeneous linewidth is strongly dependent on the presence of macroscopic defects such as dislocations and is also influenced by the presence of a cap layer. On the contrary, the homogeneous linewidth depends on the intrinsic sample properties.

In diluted magnetic semiconductors like GaMnAs and quaternary GaMnAsP alloys, the damping parameter is expected to depend on:

- The magnetic compensation which depends on the growth conditions
- The Mn concentration and the carrier (hole) concentration which is responsible for the ferromagnetic Mn-Mn interaction.
- The strain which modifies the valence band splitting

6.1.2 FMR linewidth studies

In this section we present the studies of the magnetization relaxation process in a 50 nm thick $Ga_{1-x}Mn_xAs_{1-y}P_y$ layer with x≈0.08 and y≈0.08 (high P doping), grown at 250°C by Low-Temperature MBE on a semi-insulating (100) oriented GaAs substrate. In this tensile strained layer, the easy axis of magnetization is along the

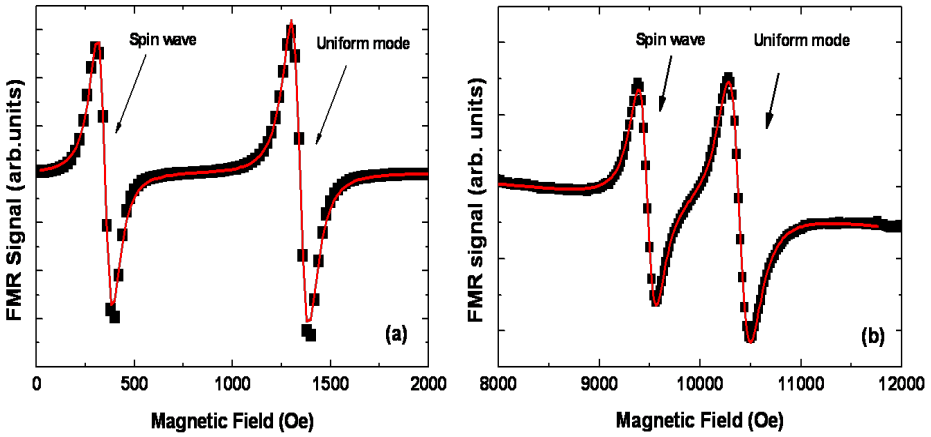

Figure 6.1: (a) X-band and (b) Q-band FMR spectra at 60K and H‖[001] (easy axis) for the $Ga_{0.92}Mn_{0.08}As_{0.92}P_{0.08}$ sample; the peak-to-peak linewidth of the FMR uniform mode is 90 and 210 Oe respectively. Black squares are the experimental data and their simulation by a Lorentzian line is shown by a line (red).

out-of plane [001] direction. This sample is metallic and its resistivity at T=15K is ρ=0.016 Ω.cm. The saturation magnetization at T=4K is 44 emu/cm^3 and the Curie temperature is 105 K, as determined by SQUID and Hall effect measurements respectively.

In figs. 6.1(a) and (b), we show typical X-band and Q-band spectra measured for H‖[001] at 60K. The spectra are characterized by an excellent signal to noise ratio and the resonances have well-defined line shapes. The line shape is perfectly Lorentzian at the two frequencies. In addition to the uniform mode, one spin-wave resonance is observed at lower field, for both frequencies. The observation of spin wave resonance in this highly P doped sample allows us to determine the effective exchange integral between the Mn ions; according to theoretical predictions its value is expected to be higher in phosphorous alloyed films [102]. In order to deduce this parameter, we have applied the phenomenological model proposed by Liu et al.[98]. The exchange constant, D, determined at T=40K, is ≈2.733 T nm^2. Considering the magnetization value at this temperature, this value corresponds to a spin stiffness value of A=0.06 pJ/m. This value is two times smaller than the one determined via magneto-optical Kerr effect microscopy [70]; We deduced from this value an effective exchange integral between the Mn ions of J_{Mn-Mn}=0.22meV.

In fig.6.2, we show the uniform mode linewidth measured at X-band as a function

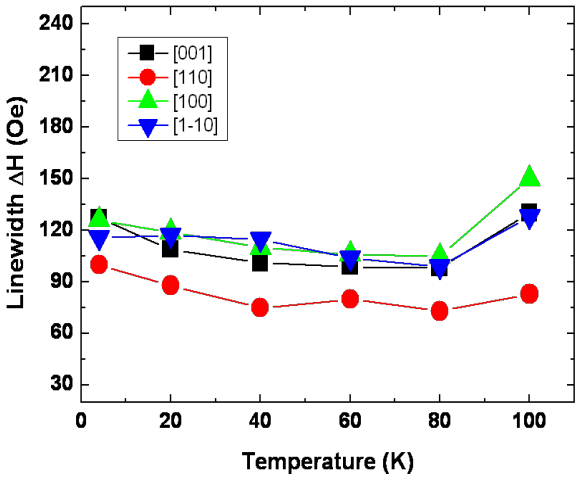

Figure 6.2: X-band FMR peak-to-peak linewidth of the uniform mode as a function of temperature for the $Ga_{0.92}Mn_{0.08}As_{0.92}P_{0.08}$ sample, for the four main orientations of the applied field: H‖[001](black,squares), H‖[110](circle,red), H‖[100](green,upper triangle) and H‖[1-10(blue,down triangle)

of temperature and orientation of the magnetic field for a y=0.08 P doped layer. The values vary between 70 and 120 Oe with weak orientation and temperature dependences. The linewidth increases close to the critical temperature (100K).

In fig.6.3, we show the Q-band results for the same sample. In the low temperature region the linewidth is about 200 Oe, a twofold increase over the X-band values. The linewidth are strictly isotropic below T=60K. For higher temperatures we observe a systematic increase of the linewidth with temperature and an increasing anisotropy. The relatively small values of the linewidth indicate a high crystalline quality and a good magnetic homogeneity of the sample.

The damping factor α is obtained from the slope of the linewidth versus microwave frequency curves assuming a linear variation. For example, fig.6.4 shows the uniform mode linewidth measured at T=80K for four high symmetry directions of the applied field. Fig.6.5 displays the uniform mode linewidth measured when the external magnetic field is parallel to [001], for different temperatures between 4K and 100K.

We show fig.6.6 the temperature dependence of the inhomogeneous linewidth. The linewidth does not vary dramatically with the temperature up to 80K, and then increases close to T_c. The inhomogeneous linewidth for H‖[001] at T=60 K is

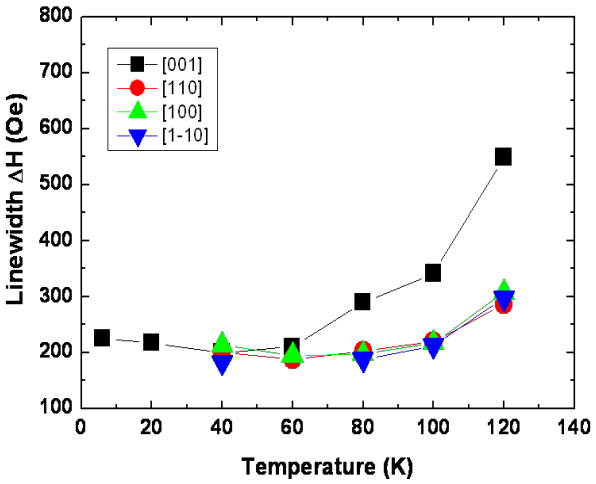

Figure 6.3: Q-band FMR peak-to-peak linewidth of the uniform mode as a function of temperature for the $Ga_{0.92}Mn_{0.08}As_{0.92}P_{0.08}$ sample, for the four main orientations of the applied field: H||[001(black,squares), H||[110](circle,red), H||[100](green,upper triangle) and H||[1-10](blue,down triangle)

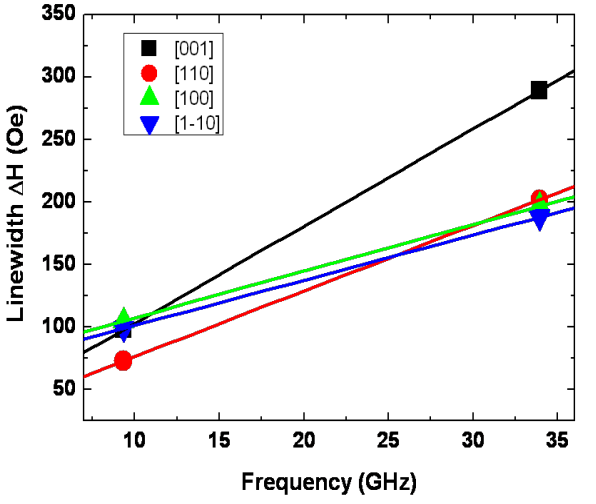

Figure 6.4: FMR peak-to-peak uniform mode linewidth as a function of microwave frequency (9.5 GHz and 35 GHz); T=80K and H||[001(black,squares), H||[110](circle,red), H||[100](green,upper triangle) and H||[1-10](blue,down triangle) for $Ga_{0.092}Mn_{0.08}As_{0.092}P_{0.08}$ sample

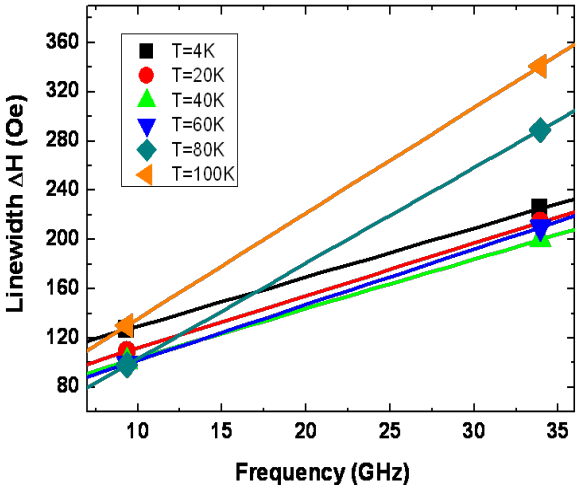

Figure 6.5: FMR peak-to-peak uniform mode linewidth as a function of microwave frequency (9.5 GHz and 35 GHz) for H||[001](easy axis) at different temperature for $Ga_{0.092}Mn_{0.08}As_{0.092}P_{0.08}$ sample

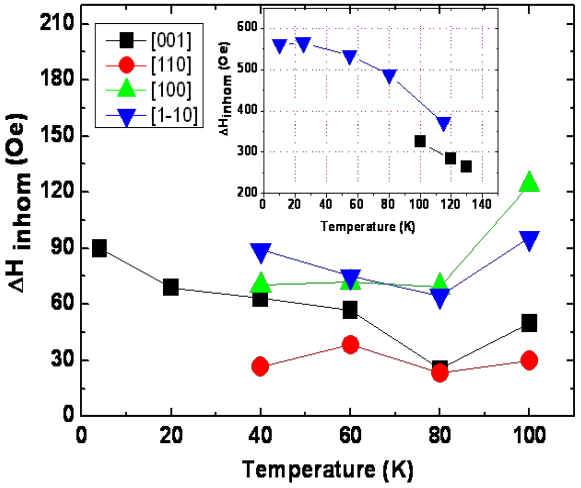

Figure 6.6: Inhomogeneous linewidth as a function of temperature for four orientations of the applied field: H||[001(black,squares), H||[110](circle,red), H||[100](green,upper triangle) and H||[1-10](blue,down triangle) for the $Ga_{0.092}Mn_{0.08}As_{0.092}P_{0.08}$ sample. Inset: $Ga_{0.92}Mn_{0.08}As$/GaInAs inhomogeneous linewidth as a function of temperature for two orientations of the applied field: H||[001(black,squares), H||[1-10](blue,down triangle)

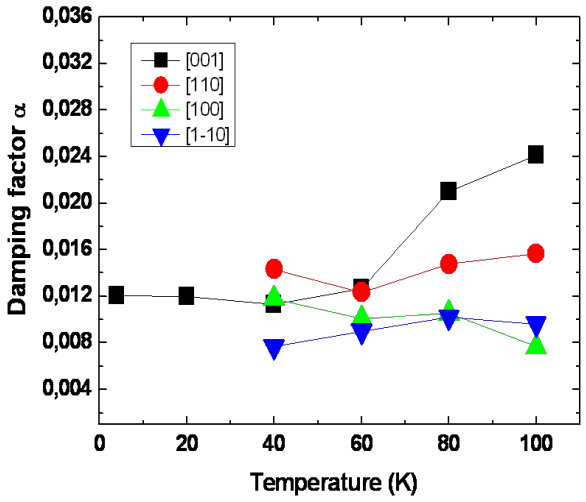

Figure 6.7: Damping factor α as a function of temperature for four orientations of the applied field: H||[001(black,squares), H||[110](circle,red),H||[100](green,upper triangle) and H||[1-10](blue,down triangle) for $Ga_{0.92}Mn_{0.08}As_{0.92}P_{0.08}$ sample. The error for α is below 0.001 as estimated from a maximum error of 10 Oe for the FMR linewidth.

about 50 0e, i.e., 50% of the total linewidth at X-band. However, Sinova et al.[145] have used the approximation $\Delta_{inhom} \ll \Delta_{hom}$ to deduce the damping factor from a single X-Band frequency measurement, but this approximation is not fullfilled here. We obtain the damping factor α from the slope of the uniform linewidth variation with microwave frequency (fig.6.7). The damping factor does not vary clearly with temperature between 4 K and 0.8 T_c and increases when the temperature approaches T_c.

6.1.3 Damping factor as a function of Phosphorous induced strain

In order to verify the influence of the Phosphorous concentration on the damping factor we have measured a second sample with a two times smaller phosphorous content: the 50 nm thick $Ga_{0.92}Mn_{0.08}As_{0.957}P_{0.043}$ layer is grown under very similar conditions as the previous shown sample. The easy axis of the magnetization of this sample is parallel to [100] direction, and its resistivity at T=15K is ρ=0.015 Ω.cm. The saturation magnetization at T=4K is 44 emu/cm^3 and the Curie temperature

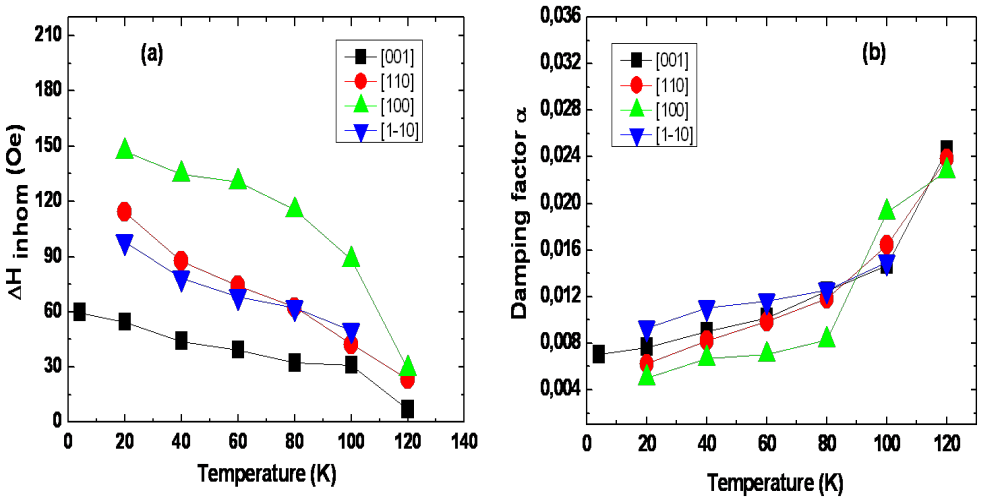

Figure 6.8: Inhomogeneous linewidth $\triangle$ H_{inhom} (a) and damping factor α (b) as a function of temperature for four orientations of the applied field; H||[001(black,squares), H||[110](circle,red),H||[100](green,upper triangle) and H||[1-10](blue,down triangle) for $Ga_{0.92}Mn_{0.08}As_{0.957}P_{0.043}$ sample

is ≈112 K.

The temperature dependence of the inhomogeneous linewidth and of the damping factor are shown in Fig.6.8(a) and Fig.6.8(b) respectively. The inhomogeneous linewidth are very anisotropic for this sample and vary by more than a factor of two. They are equally higher than in the y=0.08 doped sample. The damping factor is slightly lower andd shows a systematic increase with temperature. (Fig.6.8(b)). Typpical values are of the order of 0.010. The values are also anisotropic independent of the temperature. Near Tc, the damping factor increases strongly -0.024.

Fig.6.9 presents the inhomogeneous linewidth as a function of temperature, measured for H along [001] (a) and [110] (b) directions respectively . The inhomogeneous linewidth along [001] direction is higher for the highest Phosphorous concentration. For both concentrations, it decreases progressively with increasing temperature. On the conrary, for the [110] in plane direction (fig.6.9(b)), the inhomogeneous linewidth is smaller for the Phosphorous concentration of 0.08 than for 0.043. Whereas the inhomogeneous linewidth of the sample $Ga_{0.92}Mn_{0.08}As_{0.92}P_{0.08}$ does not vary with temperature, on the contrary the linewidth of the $Ga_{0.92}Mn_{0.08}As_{0.957}P_{0.043}$ decreases from 118 down to 28 Oe when T increases from 20K up to T_c.

As shown in fig.6.7 the damping factor of the sample with the highest P concen-

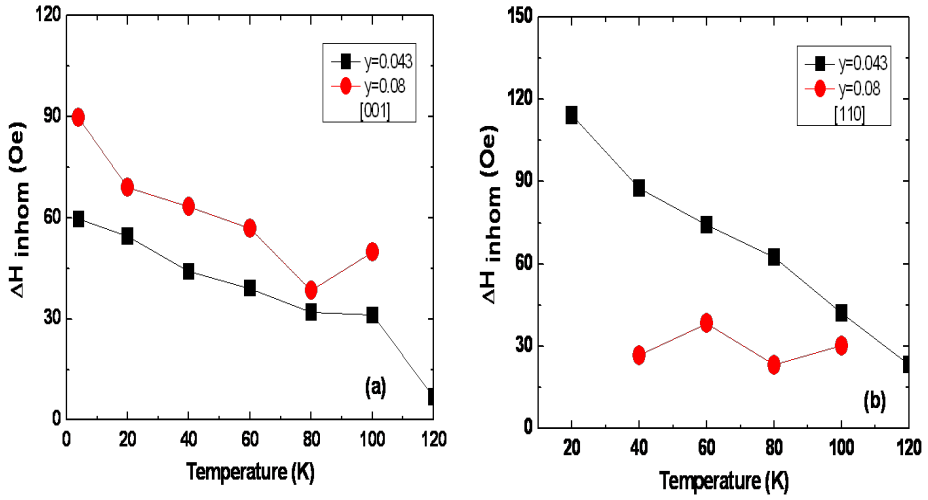

Figure 6.9: Inhomogeneous linewidth as a function of temperature measured for an external applied field along [001] axis (a) and [110] axis (b), for the $Ga_{0.92}Mn_{0.08}As_{1-y}P_y$ layers with y=0.043 (squares,black) and y=0.08 (circles,red)

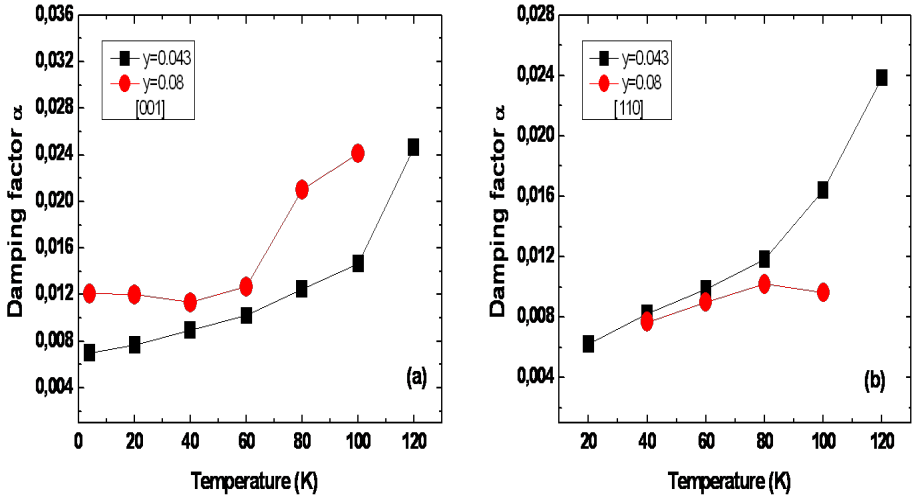

Figure 6.10: Damping factor α as a function of temperature, measured with an applied field along [001] axis (a) and [110] axis (b) for the $Ga_{0.092}Mn_{0.08}As_{1-y}P_y$ samples with y=0.043 (squares,black) and y=0.08 (circles,red)

tration is α=0.012 at low temperature (4K); this value is about three times higher than the one reported previously for phosphorous free $Ga_{0.93}Mn_{0.07}As$/GaAs layers [84]. A further interesting aspect is the small value of the inhomogeneous part of the FMR linewidth. Its value is only 40 Oe, which is comparable to the one measured in the best, state of the art, GaMnAs samples grown on GaAs(001) substrates. It is however an order of magnitude smaller than the one reported in the case of (Ga,Mn)As layers with perpendicular anisotropy, which have been obtained by epitaxial growth on GaInAs substrates (the tensile strained samples). The inhomogeneous linewidth as a function of temperature for the $Ga_{0.92}Mn_{0.08}As$/GaInAs sample are shown in the inset in fig 6.6. The inhomogeneous linewidth is a probe of the magnetic homogeneity of such films and its low value in phosphorous alloyed films indicates the absence of dislocation related to inhomogeneous doping or charge carrier distribution, which are a major drawback for the use of GaInAs buffer layers.

In the P concentration range studied here, our results show that the Phosphorous alloying in films with metallic conductivity does not lead to a significant modification of the inhomogeneous linewidth nor the damping factor. As in the case of GaMnAs layers the Gilbert damping factor is anisotropic and varies with the temperature.

6.2 Conclusion

We have determined the Gilbert damping factor α in a low and high phosphorous alloyed sample with a Mn doping level of x=0.08. The values are of the order of 0.01 but show an angular dependence -typically by a factor of two- and increase with increasing temperatures. The values are slightly higher than those previously determined for phosphorous free GaMnAs layers [84]. It would be interesting to compare these values with those determined for large angle precession MOKE measurements but such values are not yet available.

Conclusion and Perspectives

In my PhD thesis work I have studied the transport and magnetic properties of a series of ferromagnetic semi conducting thin epitaxial films and multi-layers based on manganese doped GaAs alloys. I have chosen a combination of different experimental techniques, FMR, SQUID , Hall effect measurements to measure and model the magnetic anisotropies as a functions of strain and temperature. Whereas $Ga_{1-x}Mn_xAs$ has been studied in quite detail previously the major part of my studies was performed on a new quaternary alloy system -$Ga_{1-x}Mn_xAs_{1-y}P_y$-. My results show that this system has some important advantages over the ternary alloys where due to the direct link between the strain and the Mn doping concentration these two parameters can not be changed independently.

I have shown that the phosphorous alloying introduces also a new functionality in this system due to the dependence of the Mn acceptor level position on the P concentration. Due to the increase in the thermal ionization energy of the Mn acceptor which changes from 113 meV in GaAs to 200 meV in GaP above typically 10 % phosphorous the conductivity of the layers changes from metallic to impurity band like hopping with a thermal activation energy. This change in the conduction regime modifies pronouncedly all magnetic properties like the critical temperature, the anisotropy constants. It offers further the possibility to prepare thin layers with increased resistivities which will facilitate the depletion by applied electric fields.

I have shown that thin films doped with standard Mn concentration of 7 % to 10 % and intermediate phosphorous concentrations of 6 % are very interesting as the small residual lattice mismatch related strain field can made be equal to the demagnetization field which gives rise to a system with a so-called critical strain. Such layers are quasi isotropic and characterized by drastically reduced energy barriers for magnetization switching. I have shown by FMR measurements that even small temperature shifts of 20K allow to switch such layers from a in-plane easy axis to an out-of-plane easy axis regime.

The manipulation of the orientation of the equilibrium magnetization of $Ga_{1-x}Mn_xAs$

thin films is of high fundamental and technological interest. The unique property of ferromagnetic semiconductors i.e., the long range order mediated by the hole carriers offers the possibility to modify their characteristics by changing the carrier concentration by applying electric fields. Different authors have performed such experiments and we have established cooperation with some of them to evaluate this effect also by FMR measurements. Two different systems have been studied: p/n diodes where the $Ga_{1-x}Mn_xAs$ layer is the p-type part of the diode (in collaboration with Hitachi Cambridge laboratory, UK) and ferroelectric/ferromagnetic bilayers (in collaboration with Swiss Federal Institute of Technology, Switzerland) in which a non volatile electric field can be obtained. As the measurements on diodes were not successful in the sense that no change in the FMR parameters could be observed they are not presented in this manuscript. The work on ferroelectric top layers is still in progress and further sample optimization is necessary in order to study the influence of electric fields by the FMR technique. Due to the incomplete character of these results they are neither presented in this thesis. However quaternary layers in the impurity conduction regime seem to be good candidates for further studies in this field.

The ferromagnetic compound MnAs has found increasing attention in the last years due to its high critical temperature and the fact that it can epitaxially grown on GaAs. I have studied the magnetic anisotropies of epitaxial ultra-thin films grown on (111) and (100)GaAs or $Ga_{1-x}Mn_xAs$ by FMR and SQUID techniques. The choice of high frequency FMR studies has allowed me to overcome the traditional difficulties linked to the extremely high built in anisotropy and I have measured for the first time the uniform mode spectra of these films by FMR. I have determined the anisotropy constants for both epitaxies and shown that the generally assumed full relaxation of MnAs layers on GaAs(001) is not correct. These layers are equally submitted to an important strain linked to the lattice mismatch.

I have equally determined by FMR measurements at 115 GHz and 230 GHz the Gilbert damping factor for this material which had not been known up to now.

When grown on ferromagnetic $Ga_{1-x}Mn_xAs$ films the bilayers are characterized by an exchange bias field of several 10^2 Oe which I have determined by SQUID measurements as a function of temperature. We have not observed any significant change in the critical temperature of the $Ga_{1-x}Mn_xAs$ layer due to the coupling with the MnAs top layer. This is quite different to the recently published results [99, 117] on the similar system of Fe/$Ga_{1-x}Mn_xAs$ bilayers.

Now that many basic properties of the ferromagnetic GaAs based thin films are well known it would be interesting to extend these studies to patterned films in order to modify the shape anisotropy and determine the related anisotropies. Given the high sensitivity of the FMR technique it should be possible to measure wires, pillars on 100 μm sized samples which can be obtained by lithography.

We should also pursue the studies of ultra-thin layers with thickness inferior to 10 nm. Up to now it is not known which is the minimum layer thickness, given the DMS character of this material-for the onset of long range order-. From similar studies on ultra-thin Fe films it is known that below a certain thickness surface anisotropies will become important and can even become dominant for the magnetic properties of such layers. No study in this sense has been reported up to now.

Bibliography

[1] *http://nobelprize.org/nobel$_p$rizes/physics/laureates/2007/press − fr.html.*

[2] *http://www2.cnrs.fr/en/992.htm.*

[3] *http://hyperphysics.phy-astr.gsu.edu/Hbase/solids/squid.html.*

[4] A. Jander A. A. Serga A. V. Chumak, P. Dhagat and B. Hillebrands. *arXiv:0907.2902v1*, 2009.

[5] M. Abolfath, T. Jungwirth, J. Brum, and A. H. MacDonald. *Phys. Rev. B*, 63:054418, 2001.

[6] K. Akabli and H. T. Diep. *Phys. Rev. B*, 77:165433, 2008.

[7] M. Amato, M. G. Pini, and A. Rettori. *Phys. Rev. B*, 60:5, 1999.

[8] A. Barthelemy, A. Fert, J-P. Contoura, M. Bowen, V. Cros, J.M. De Teresa, A. Hamzic, J.C. Faini, J.M. George, J. Grollier, F. Montaigne, F. Paillouxa, F. Petroff, and C. Vouille. *J. Mag. Mag. Mat.*, 242-245:68–76, 2002.

[9] O. Beckman, K. Gramm, L. Lundgeren, K. V. Rao, and H. S. Chen. *Solid State Communication*, 39:777–780, 1981.

[10] C. Bihler, M. Althammer, A. Brandlmaier, S. Geprags, M. Opel, W. Schoch, W. Limmer, R. Gross, M. S. Brandt, and S. T. B. Goennenwein. *Phy. Rev. B*, 78:045203, 2008.

[11] C. Bihler, M. Kraus, H. Huebl, M. S. Brandt, S. T. B Goennenwein, M. Opel, M. A. Scarpulla, P. R. Stone, R. Farshchi, and O. D. Dubon. *Phy. Rev. B*, 75:214419, 2007.

[12] Ch. Binek, S. Polisetty, Xi He, and A. Berger. *Phys. Rev. Lett.*, 96:067201, 2006.

[13] R. W. De Blois and D. S. Rodbell. *Phyical Review*, 130:4, 1963.

[14] J. De Boeck, R. Oesterholt, A. Van Esch, H. Bender, C. Bruynseraede, C. Van Hoof, and G. Borghs. *Appl. Phys. Lett.*, 68:2744, 1996.

[15] R. Breitwieser, M. Marangolo, J. Luning, N. Jaouen, L. Joly, M. Eddrief, V. H. Etgens, and M. Sacchi. *Appl. Phys. Lett.*, 93:122508, 2008.

[16] K. S. Burch, D. B. Shrekenhamer, E. J. Singley, J. Stephens, B. L. Sheu, R. K. Kawakami, P. Schiffer, N. Samarh, D. D. Awschalom, and D. N. Basov. *Phys. Rev. Lett.*, 97:087208, 2006.

[17] K.S. Burch, D.D. Awschalom, and D.N. Basov. *J.Mag.Mag. Mat.*, 320:3207–3228, 2008.

[18] H. B. Callen and E. Callen. *J. Phys. Chem. Solid*, 27:1271, 1996.

[19] R. P. Campion, K.W. Edmonds, L.X. Zhao, K.Y. Wang, C.T. Foxon, B.L. Gallager, and C.R. Staddon. *Journal of Crystal Growth*, 247:42, 2003.

[20] C. Chappert, K. Le Dang, P. Beauvillain, H. Hurdequint, and D. Renard. *Phys. Rev. B*, 34:5, 1986.

[21] S. C. Chen and H. L. Huang. *IEEE Trans. Mag.*, 33:3978, 1997.

[22] D. Chiba, Y. Nishitani, F. Matsukura, and H. Ohno. *Appl. Phys. Lett.*, 90(12):122503, 2007.

[23] D. Chiba, M. Sawicki, Y. Nishitani, Y. Nakatani, F. Matsukura, and H. Ohno. *Nature (London)*, 455:515, 2008.

[24] D. Chiba, M. Yamanouchi, F. Matsukura, and H. Ohno. *Science*, 301:943, 2003.

[25] S. H. Chun, S. J. Potashnik, K. C. Ku, J. J. Berry, P. Schiffer, and N. Samarth. *Appl. Phys. Lett.*, 78:17, 2001.

[26] S.H. Chun, S. J. Potashnik, K. C. Ku, P. Schiffer, and N. Samarth. *Phys. Rev. B*, 66:100408(R), 2002.

[27] J.H. Chung, S. J. Chung, S. Lee, B. J. Kirby, J. A. Borchers, Y. J. Cho, X. Liu, and J. K. Furdyna. *Phys. Rev. Lett.*, 101:237202, 2008.

[28] B. Clearjaud, D. Wasik, R. Bouanani-Rahbi, G. Strzelecka, A. Hruban, and M. Kaminska. *J.Appl. Phys.*, 103:123507, 2008.

[29] J.F. Cochran, B. Heinrich, and A.S. Arrott. *Phys. Rev. B*, 34:7788, 1986.

[30] C. Cohen, J. A. Davies, A. V. Drigo, and T. E. Jackman. *Nuclear Instruments and Methods in Physics Research*, 218:147–148, 1983.

[31] M. Cubukcu, H. J. von Bardeleben, Kh. Khazen, J. L. Cantin, M. Zhu, M. J. Wilson, P. Schiffer, and N. Samarth. *J.Appl. Phys.*, 105:07C506, 2009.

[32] M. Cubukcu, H. J. vonB ardeleben, Kh. Khazen, J.L. Cantin, O. Mauguin, L. Largeau, and A. Lemaître. *Phys. Rev. B(Rapid communication)*, 81:041202(R), 2010.

[33] M. Cubukcu, H. J. vonBardeleben, J. L. Cantin, and A. Lemaître. *Appl. Phys. Lett.*, 96:102502, 2010.

[34] T. Dietl. *Semicond. Sci. Technol.*, 17:377–392, 2002.

[35] T. Dietl, A. Haury, and Y. M. d'Aubigne. *Phys. Rev. B*, 55:R3347–R3350, 1997.

[36] T. Dietl, J. Konig, and A.H. MacDonald. *Phys. Rev. B*, 64:241201, 2001.

[37] T. Dietl, H. Ohno, and F. Matsukura. *Phys. Rev. B*, 63:195205, 2001.

[38] T. Dietl, H. Ohno, F. Matsukura, J. Cibert, and D. Ferrand. *Science*, 287:1019–1022, 2000.

[39] M. Donath and W. Nolting. Local-moment ferromagnets. *Lecture Notes in Physics, Springer, 2005*, pages 147–159.

[40] A. Dourlat, V. Jeudy, A. Lemaître, and C. Gourdon. *Phys. Rev. B*, 78:161303(R), 2008.

[41] A. Dourlat, V. Jeudy, C. Testelin, F. Bernardot, K. Khazen, C. Gourdon, L. Thevenard, L. Largeau, O. Mauguin, and A. Lemaître. *J. Appl. Phys.*, 102:023913, 2007.

[42] K. Dziatkowski, Z. Ge, X. Liu, and J. K. Furdyna. *Appl.Phys.Lett.*, 88(14):142513, 2006.

[43] K. Dziatkowski, Z. Ge, X. Liu, J.K. Furdyna, B. Clerjaud, and A. Twardowski. *Acta Physica Polonica A*, 112, 2007.

[44] K. W. Edmonds, K. Y. Wang, R. P. Campion, A. C. Neumann, N. R. S. Farley, B. L. Gallagher, and C. T. Foxon. *Appl. Phys.Lett.*, 81(26):4991–4993, 2002.

[45] K. F. Eid, M. B. Stone, K. C. Ku, O. Maksimov, P. Schiffer, N. Samarth, T. C. Shih, and C. J. Palmstrøm. *Appl. Phys. Lett.*, 85:9, 2004.

[46] K. F. Eid, M. B. Stone, O. Maksimov, T. C. Shih, K. C. Ku, W. Fadgen, C. J. Palmstrøm, P. Schiffer, and N. Samarth. *J.Appl. Phys.*, 97:10D304, 2005.

[47] M. Elsen, O. Boulle, J.-M. George, H. Jaffrès, R. Mattana, V. Cros, A. Fert, A. Lemaitre, R. Giraud, and G. Faini. *Phys. Rev. B*, 73:035303, 2006.

[48] M. Elsen, H. Jaffrès, R. Mattana, L. Thevenard, A. Lemaitre, and J.-M. George. *Phys. Rev. B*, 76:144415, 2007.

[49] R. Engel-Herbert, T. Hesjedal, D. M. Schaadt, L. Daweritz, and K. H. Ploog. *Apl. Phys. Lett.*, 88:052505, 2006.

[50] A. Haury et al. *Phys. Rev. Lett.*, 79:511, 1997.

[51] J. Wang et al. *J. Phys. Condens. Matter*, 18:R501–R530, 2006.

[52] R. C. Myers et al. *Phy. Rev. B*, 74:155203, 2006.

[53] S. Metz et al. *Proc.6th Int.Symp.GaAs and Related Compounds*, page 6, 1977.

[54] S. Nilson et al. *Defects in semiconductors, Materials Science Forum*, 10-12:615, 1986.

[55] T. Jungwirth et al. *Phy. Rev. B*, 72:165204, 2005.

[56] Thompson et al. *Phy. Rev.*, 146:601.

[57] M. Farle. *Report on Progress in Physics*, 61:755, 1998.

[58] D. Ferrand, J. Cibert, A. Wasiela, C. Bourgognon, S. Tatarenko, G. Fishman, T. Andrearczyk, T. Dietl, B. Barbara, and D. Dufeu. *Phys. Rev. B*, 63:085201, 2001.

[59] Albert Fert. *Thin solid Films*, 517:2–5, 2008.

[60] Albert Fert, J-M. George, H. Jaffres, R. Mattana, and Pierre Seneor. *Europhysics news*, 34:227, 2003.

[61] M. E. Fisher. *Rev. Mod. Phys.*, 46:597, 1971.

[62] E. D. Fraser, C. H. Kim, S. Hegde, H. Zeng, H. Luo, and P. K. Wei. *J.Appl. Phys.*, 104:033921, 2008.

[63] J. A. Gaj, J. Ginter, and R. R. Galazka. *Phys. Status Solidi B*, 89:655, 1978.

[64] M. Glunk, J.Daeubler, L. Dreher, S.Schwaiger, W. Schoch, R.Sauer, W.Limmer, A. Brandlmaier, S.T.B. Goennenwein, C.Bihler, and M.S.Brandt. *Phys. Rev. B*, 79:195206, 2009.

[65] E. Goto, N. Hayashi, T. Miyashita, and K. Nakagawa. *J.Appl. Phys.*, 36:2951, 1965.

[66] C. Gourdon, A. Dourlat, V. Jeudy, K.Khazen, H. J. von Bardeleben, L. Thevenard, and A. Lemaître. *Phys.Rev. B*, 76:241301, 2007.

[67] C. Gourdon, V. Jeudy, A. Cebers, A. Dourlat, Kh. Khazen, and A. Lemaître. *Phys. Rev. B*, 80:161202(R), 2009.

[68] M. Grimsditch, R. Camley, E. E. Fullerton, S. Jiang, S.D. Bader, and C.H. Sowers. *J.Appl. Phys.*, 85:8, 1999.

[69] Z. J. Guo, J. S. Jiang, J. E. Pearson, S. D. Bader, and J. P. Liu. *Appl. Phys. Lett*, 81:11, 2002.

[70] S. Haghoo, M. Cubukcu, H. J. von Bardeleben, L. Thevenard, A. Lemaitre, and C. Gourdon. *Phys.Rev.B*, 041301(R), 2010.

[71] B. Heinrich and J. A. C. Bland. Ultrathin magnetic structures 2, edited by b. heinrich and j.bland. *Springer, Heidelberg*.

[72] B. Henrich. Ultrathin magnetic structures 3, edited by j. bland and b. heinrich. *Springer-Verlag, Berlin*, page p.143, 2005.

[73] M. C. Hickey and J. S. Moodera. *Phys.Rev.B*, 102:137601, 2009.

[74] H.L. Huang, V. L. Sobolev, and S. C. Chen. *J. Appl.Phys.*, 81:4066, 1997.

[75] A. Hubert and R. Schafer. *Magnetic Domains*, 1998.

[76] T. Jungwirth, W. A. Atkinson, B. H. Lee, and A. H. MacDonald. *Phys. Rev. B*, 59:9818, 1999.

[77] T. Jungwirth, J. Konig, J. Sinova, J. Kucera, and A. H. MacDonald. *Phys. Rev. B*, 66:012402, 2002.

[78] T. Jungwirth, J. Sinova, A. H. MacDonald, B. L. Gallagher, V. Novák, K. W. Edmonds, A. W. Rushforth, R. P. Campion, C. T. Foxon, L. Eaves, E. Olejnik, J. Masek, S.-R. Eric Yang, J. Wunderlich, C. Gould, L. W. Molenkamp, T. Dietl, and H. Ohno. *Phys. Rev. B*, 76:125206, 2007.

[79] T. Jungwirth, J. Sinova, J. Masek, J. Kucera, and A. H. MacDonald. *Rev. Mod. Phys.*, 78:809, 2006.

[80] K. Alberiand K. M. Yu. *Phys. Rev. B*, 65:201303, 2002.

[81] M. Kastner, C. Hermann, L. Daweritz, and K. H. Ploog. *J.Appl. Phys.*, 92:10, 2002.

[82] Kh. Khazen. *PhD thesis, Université Pierre et Marie Curie*, 2008.

[83] Kh. Khazen, H. J. von Bardeleben, J. L. Cantin, L. Thevenard, L. Largeau, O. Mauguin, and A. Lemaître. *Phys. Rev. B*, 77:165204, 2008.

[84] Kh. Khazen, H. J. von Bardeleben, M. Cubukcu, J. L. Cantin, V. Novak, K. Olejnik, M. Cukr, L. Thevenard, and A. Lemaître. *Phys.Rev.B*, 78:195210, 2008.

[85] Kh. Khazen, H.J. von Bardeleben, J. L. Cantin, A. Mauger, L. Chen, and J. H. Zhao. *Phys. Rev. B*, 81:235201, 2010.

[86] B. J. Kirby, J. A. Borchers, X. Liu, Z. Ge, Y.J. Cho, M. Dobrowolska, and J.K. Furdyna. *Phys. Rev. B*, 76:205316, 2007.

[87] C. Kittel. *Phys. Rev. B*, 110:836, 1958.

[88] P. M. Krstajiæ, F. M. Peeters, V. Fleurov, and K. Kikoin. *Phys. Rev. B*, 70:195215, 2004.

[89] L. Landau and E. Lifshitz. *Phys. Z. Sowjetunion*, 8:152, 1935.

[90] H. Lee, S. Chung, S. Lee, X. Liu, and J. K. Furdyna. *Solid State Communication*, 149:1300–1303, 2009.

[91] A. Lemaitre, A. Miard, L. Travers, O. Mauguin, L. Largeau, C. Gourdon, V. Jeudy, M. Tran, and J.-M. George. *Appl. Phys. Lett.*, 93(2):021123, 2008.

[92] A. H. V. Repetto Liamazares, J. Milano, L. B. Steren, V. Garcia, M. Marangolo M. Eddrief, and V. H.Etgens. *Physica B*, 398:372–375, 2007.

[93] E. M. Lifschitz and L. P. Pitaevskii. *Statistical Physics (Pergamon Press), Oxford, United Kingdom*, Part2, 1980.

[94] J. Lindner, T. Tolinski, K. Lenz, E. Kosubek, H. Wende, K. Baberschke, A. Ney, T. Hesjedal, C. Pampuch, R. Koch, L. Daweritz, and K. H. Ploog. *J. Mag.Mag.Mat.*, 277:159–164, 2004.

[95] M. Linnarsson, E. Janzén, B. Monemar, M. Kleverman, and A. Thilderkvist. *Phys. Rev. B*, 55:6938, 1997.

[96] X. Liu, W. L. Lim, L. V. Titova, M. Dobrowolska, J. K. Furdyna, M. Kutrowski, and T. Wojtowicz. *J.Appl.Phys.*, 98:063904, 2005.

[97] X. Liu, Y. Sasaki, and J. K. Furdyna. *Phys. Rev. B*, 67:205204, 2003.

[98] X. Liu, Y. Y. Zhou, and J. K. Furdyna. *Phys. Rev. B*, 75:195220, 2007.

[99] F. Maccherozzi, M. Sper, G. Panaccione, J. Minar, S. Polesya, H. Ebert, U. Wurstbauer, M. Hochstrasser, G. Rossi, G. Woltersdorf, W. Wegscheider, and C. H. Back. *Phy. Rev. Lett.*, 101:267201, 2008.

[100] A. H. MacDonald, P. Schiffer, and N. Samarth. *Nature Materials*, 4, 2005.

[101] S. Mack, R. C. Myers, J. T. Heron, A. C. Gossard, and D. D. Awschalom. *Appl. Phys. Lett.*, 92(19):192502, 2008.

[102] J. Masek, J. Kudrnovsky, F. Maca, J. Sinova, A. H. MacDonald, R. P. Campion, B. L. Gallager, and T. Jungwirth. *Phys. Rev. B*, 75:045202, 2007.

[103] J. Masek and F. Maca. *Phys. Rev. B*, 69:165212, 2004.

[104] Y. H. Matsuda, A. Oiwa, K. Tanaka, and H. Munekata. *Physica B*, 668:376–377, 2006.

[105] F. Matsukura, H. Ohno, A. Shen, and Y. Sugawara. *Phys. Rev. B*, 57:R2037, 1998.

[106] D. Mauri, H. C. Siegmann, P. S. Bagus, and E. Kay. *J.Appl. Phys.*, 62:3047, 1987.

[107] J. Mohanty. *PhD thesis*, 2005.

[108] H. Munekata, H. Ohno, S. von Molnar, A. Segmuller, L. L. Chang, and L. Esaki. *Phys. Rev. Lett.*, 63:1849, 1989.

[109] T. Nagahama, K. Mibu, and T. Shonjo. *J. Phys. D: Appl. Phys.*, 31:43–49, 1997.

[110] V. P. Nascimento, E. Baggio Saitovitch, F. Pelegrinia, L. C. Figueiredo, A. Biondo, and E. C. Passamani. *J.Appl. Phys.*, 99:08C108, 2006.

[111] V. Novak, K. Olejnik., J. Wunderlich, M. Cukr, K. Viborny, A.W Rushforth, K.W Edmonds, R.P Campion, B.L. Gallager, J. Sinova, and T. Jungwirth. *Phys. Rev. Lett.*, 101:077201, 2008.

[112] H. Ohno, D. Chiba, F. Matsukura, T. Omiya, E. Abe, T. Dietl, Y. Ohno, and K. Ohtani. *Nature*, 408:944, 2000.

[113] H. Ohno, H. Munekata, T. Penney, S. von Molnar, and L. L.Chang. *Phys. Rev. Lett.*, 68:2664, 1992.

[114] H. Ohno, A. Shen, F. Matsukura, A. Oiwa, A. Endo, S. Katsumoto, and Y. Iye. *Appl. Phys. Lett.*, 69(3):363–365, 1996.

[115] Y. Ohno, D. K. Young, B. Beschoten, F. Matsukura, H. Ohno, and D. D. Awschalom. *Nature (London)*, 402:790, 1999.

[116] J. Okabayashi, A. Kimura, O. Rader, T. Mizokawa, A. Fujimori, T. Hayashi, and M. Tanaka. *Phys. Rev. B*, 58:R4211, 1998.

[117] K. Olejnik, P. Wadley, J. A. Haigh, K. W. Edmonds, R. P. Campion, A. W. Rushforth, B. L. Gallager, C. T. Foxon, T. Jungwirth, J. Wiunderlich, S. S. Dhesi, S. A. Cavill, G. van der Laan, and E. Arenholz. *Phys. Rev. B*, 81:104402, 2010.

[118] M. Overby, A. Chernyshov, L. P. Rokhinso, X. Liu, and J.K. Furdyna. *Appl. Phys. Lett*, 92:192501, 2008.

[119] M. Overby, A. Chernyshov, L. P. Rokhinson, X. Liu, and J. K. Furdyna. *Appl. Phys. Lett*, 92:192501, 2008.

[120] M. H. S. Owen, J. Wunderlich, V. Novak, K. Olejnik, J. Zemen, K. Vyborny, S. Ogawa, A. C. Irvine, A. J. Ferguson, H. Sirringhaus, and T. Jungwirth. *New journal of Physics*, 11:023008, 2009.

[121] E. A. Pashitskii and S. M. Ryabchenko. *Sov. Phys. Solid State*, 21:322, 1979.

[122] T. Plake, T. Hesjedal, J. Mohanty, M. Kastner, L. Daweritz, and K. H. Ploog. *Appl. Phys. Lett*, 82:14, 2003.

[123] K. H. Ploog, L. Daweritz, R. Engel-Herbert, and T. Hesjedal. *Phys. stat. sol.*, 14:3574–3580, 2006.

[124] S. J. Potashnik, K. C. Ku, S. H. Chun, J. J. Berry, N. Samarth, and P. Schiffer. *Appl. Phys. Lett.*, 79(10):1495–1497, 2001.

[125] S.J. Potashnik, K.C. Ku, R. Mahendiran, S.H. Chun, R.F. Wang, N. Samarth, and P. Schier. *Phys. Rev. B*, 66:012408, 2002.

[126] P.R.Stone, K.Alberi, S.K.Z. Tardif, J.W. Beeman, K.M. Yu, W. Walukiewicz, and O.D. Dubon. *Phys. Rev. Lett.*, 101:087203, 2008.

[127] P.W.Sparks. *Phys.Rev.*, 163:779, 1967.

[128] J. Qi, Y. Xu, A. Steigerwald, N. Tolk, X. Liu, J. K. Furdyna, and T. V. Shahbazyan. *arXiv:0807.1740v1.*

[129] S. W. E. Reiester, I. Stolichnov, H. J. Trodahl, N. Setter, A. W. Rushforth, K. W. Edmonds, R. P. Campion, C. T. Foxon, B. L. Gallagher, and T. Jungwirth. *Appl. Phys. Lett.*, 94:063504, 2009.

[130] E. Rozkotova, P. Nemec, P. Horodyska, D. Sprinz, F. Trojanek, P. Maly, V. Novak, K. Olejnik, M. Cukr, , and T. Jungwirth. *Appl. Phys. Lett*, 92:122507, 2008.

[131] A. W. Rushforth, E. De Ranieri, J. Zemen, J. Wunderlich, K. W. Edmonds, C. S. King, E. Ahmad, R. P. Campion, C. T. Foxon, B. L. Gallager, K. Vyborny, J. Kucera, and T. Jungwirth. *Phys. Rev. B*, 78:085314, 2008.

[132] A. W. Rushforth, M. Wang, N. R. S. Farley, R. P. Campion, K. W. Edmonds, C. R. Staddon, C. T. Foxon, and B. L. Gallagher. *J.Appl. Phys.*, 104(7):073908, 2008.

[133] K.S. Ryu, J. Kim, Y. Lee, H. Akinaga, T. Manago, R. V., and S. Shin. *Appl. Phy. Lett.*, 89:232506, 2006.

[134] M. Sacchi, M. Marangolo, C. Spezzani, L. Coelho, R. Breitwieser, J. Milano, and V. H. Etgens. *Phys. Rev. B*, 77:165317, 2008.

[135] J. Sadowski and J. Z. Domagala. *Phys. Rev. B*, 69:075206, 2004.

[136] D. Saha, M. Holub, P. Bhattacharya, and Y. C. Liao. *Appl. Phys.Lett.*, 89(14):142504, 2006.

[137] H. Salto, V. Zayets, S. Yamagata, and K. Ando. *Phys. Rev. Lett.*, 90:207202, 2003.

[138] M. Sawicki, F. Matsukura, T. Dietl, G. Schoot, C. Ruster, G. Schmidt, L. Molenkamp, and G. G. Karczewski. *Journal of Superconductivity*, 16:7, 2003.

[139] M. Sawicki, F. Matsukura, A. Idziaszek, T. Dietl, G. M. Schott, C. Ruester, C. Gould, G. Karczewski, G. Schmidt, and L. W. Molenkamp. *Phys.Rev. B*, 70:245325, 2004.

[140] M. Sawicki, F. Matsukura, A. Idziaszek, T. Dietl, G. M. Schott, C. Ruester, C. Gould, G. Karczewski G. Schmidt, and L. W. Molenkamp. *Phys. Rev. B*, 70:245325, 2004.

[141] M.A. Scarpulla, B.L.Cardozo, R.Farshchi, W.M.H.Oo, M.D.McCluskey, K.M. Yu, and O.D.Dubon. *Phys. Rev. Lett.*, 20:207204., 2005.

[142] D. Schmaus and I. Vickridge. 4 mev ion beam analytical methods. *Analytical methods for corrosion science and engineering*, page 103, 2006.

[143] F. Schreiber, J. Pflaum, Z. Frait, Th. Muhge, and J. Pelz. *Solid State Communication*, 93:965, 1995.

[144] B. L. Sheu, R. C. Myers, J.-M. Tang, N. Samarth, D. D. Awschalom, P. Schiffer, and M. E. Flatte. *Phys. Rev. Lett.*, 99:227205, 2007.

[145] J. Sinova, T. Jungwirth, X. Liu, Y. Sasaki, J. K. Furdyna, W. A. Atkinson, and A. H. MacDonald. *Phys. Rev. B*, 69:085209, 2004.

[146] J. Smit and H.G. Beljers. *Philips Res. Rep.*, 10:113, 1955.

[147] L. B. Steren, J. Milano, V. Garcia, M. Marangolo, M. Eddrief, and V. H. Etgens. *Phys. Rev. B*, 74:144402, 2006.

[148] I. Stolichnov, S. W. E. Reister, H.J. Trodahl, N. Setter, A.W. Rushforth, K.W. Edmonds, R.P. Campion, C.T. Foxon, B.L. Gallagher, and T. Jungwirth. *Nature Material*, 7:464, 2008.

[149] P.R. Stone, J.W. Beerman, K.M. Yu, and O.D. Dubon. *Physica B*, 401-402:454, 2007.

[150] D. Suess. *Appl. Phys. Lett*, 89:113105, 2006.

[151] A. Sugawara, H. Kasai, A. Tonomura, P. D. Brown, R. P. Campion, K.W. Edmonds, B. L. Gallagher, J. Zemen, and T. Jungwirth. *Phys. Rev. Lett.*, 100:047202, 2008.

[152] J. Szczytko, A. Twardowski, M. Palczewska, M. Tanaka, T. Hayashi, and K. Ando. *Phys. Rev. B*, 60:8304, 1999.

[153] M. Tanaka, J. P. Harbison, M. C. Park, Y. S. Park, T. Shin, and G. M. Rothberg. *Appl. Phys. Lett*, 65:15, 1994.

[154] H. X. Tang, R. K. Kawakami, D. D. Awschalom, and M. L. Roukes. *Phys. Rev. Lett.*, 90:107201, 2003.

[155] L. Thevenard, L. Largeau, O. Maufuin, G. Patriarche, A. Lemaître, N. Vernier, and J. Ferré. *Phys. Rev. B*, 73:195331, 2006.

[156] L. Thevenard, L. Largeau, O. Mauguin, A. Lemaitre, Kh. Khazen, and H.J. vonBardeleben. *Phys. Rev. B*, 75:195218, 2007.

[157] L. Thevenard, L. Largeau, O. Mauguin, A. Lemaître, and B. Theys. *Appl. Phy. Lett.*, 87:182506, 2005.

[158] L. Thevenard, L. Largeau, O. Mauguin, G. Patriarche, A. Lemaitre, N. Vernier, and J. Ferré. *Phys. Rev. B*, 73:195331, 2006.

[159] L. Thevenard, E. Peronne, C. Gourdon, C. Testelin, M. Cubukcu, E. Charron, S. Vincent, A. Lemaitre, and B. Perrin. *Phys. Rev.B*, 82:104422, 2010.

[160] L. V. Titova, M. Kutrowski, X. Liu, R. Chakarvorty, W. L. Lim, J. K. Furdyna, and M. Dobrowolska. *Phys. Rev. B*, 72:165205, 2005.

[161] U.Welp, V. K. Vlasko-Vlasov, X. Liu, J. K. Furdyna, and T.Wojtowicz. *Phys. Rev. Lett.*, 90:167206, 2003.

[162] V.K. Vlasko-Vlasov, U. Welp, J. S. Jiang, D.J. Miller, G. W. Crabtree, and S. D. Bader. *Phys. Rev. Lett.*, 86:19, 2001.

[163] S. V. Vonsovskii. *Ferromagnetic Resonance (Pergamon, Oxford)*, 1966.

[164] J. Wang, L. Cywinski, C. Sun, J. Kono, H. Munekata, and L. J. Sham. *Phys. Rev. B*, 77:235308, 2008.

[165] K.Y. Wang, K.W. Edmonds, L.X. Zhao, M. Sawicki, R.P. Campion, B.L. Gallager, and C.T. Foxon. *Phys. Rev. B*, 72:115207, 2005.

[166] M. J. Wilson, M. Zhu, R. C. Myers, D. D. Awschalom, P. Schiffer, and N. Samarth. *Phys. Rev. B*, 81:045319, 2010.

[167] A. Wirthmann, X. Hui, N. Mecking, Y. S. Gui, T. Chakraborty, C. M. Hu, M. Reinwald, C. Schüller, and W. Wegschneider. *Appl. Phys. Lett.*, 92:232106, 2008.

[168] X.Liu and J.K. Furdyna. *J. Phys. Condens. Matter*, 18:R245–R279, 2006.

[169] A. M. Yakunin, A.Yu. Silov, P.M. Koenraad, J. H.Wolter, W.Van Roy, J. De Boeck, J.-M. Tang, and M. E. Flatte. *Phys. Rev. Lett.*, 92:216806, 2004.

[170] Y. Yeshurun, M. B. Salamon, K. V. Rao, and H. S. Chen. *Phys. Rev. B*, 24:1536, 1981.

[171] J. Zemen, J.Kucera, K., and T. Jungwirth. *Phys. Rev. B*, 80:155203, 2009.

[172] L. X. Zhao, C. R. Staddon, K. Y. Wang, K. W. Edmonds, R. P. Campion, B. L. Gallagher, and C. T. Foxon. *Appl. Phys. Lett*, 86:071902, 2005.

[173] M. Zhu. *PhD thesis*, The Pennsylvania State University, 2006.

[174] M. Zhu, M. J. Wilson, P. Mitra, P. Schiffer, and N. Samarth. *Phys. Rev. B*, 78:195307, 2008.

[175] M. Zhu, M. J. Wilson, B. L. Sheu, P. Mitra, P. Schiffer, and N. Samarth. *Appl. Phys.Lett.*, 91(19):192503, 2007.

CONFERENCES

Oral Presentations

- "High Frequency FMR spectroscopy of thin MnAs Epilayers grown on (111) and (100) GaAs" , **American Physical Society (APS) March Meeting**, Portland, OR, USA (2010)
- "Tayloring the Uniaxial Anisotropy and Conductivity Regimes in GaMnAsP" **11. Joint MMM/Intermag International Conference**, Washington DC, USA (2010)
- "FMR study of GaMnAsP thin films with variable P concentrations", **E-MRS Fall Meeting**, Warsaw, Poland (2009)
- **Journée de GaMnAs IDF**, Paris, France (2009)
- "Ferromagnetic Resonance Study of MnAs/GaMnAs Bilayers" **53th Conference on Magnetism and Magnetic Materials (MMM)**, Austin, Texas, USA (2008)
- "Magnetization relaxation and In homogeneity in annealed GaMnAs /GaAs epitaxial layers", **Electronic Material Conference (EMC)**, University of California,USA (2008)

Posters

- **International Conference on Magnetism (ICM)**, Karlsruhe, Germany (2009)
- **Fifty International School and Conference on Spintronics and Quantum Information Technology (SPINTEC V)**, Cracow, Poland (2009)
- **Journée scientifique de l'axe "electronique spin"CNanoIDF**, Versailles, France(2009)
- **International Magnetic Conference (INTERMAG)**, Madrid, Spain (2008)
- **International School of Nanomagnetism and Spintronics**, Prague, Czech Republic (2008)

PUBLICATIONS

- L. Thevenard, E. Peronne, C. Gourdon, C. Testelin, **M. Cubukcu**, E. Charron, S. Vincent, A. Lemaître, B. Perrin "Effect of picoseconds strain pulses on thin layers of the ferromagnetic semiconductor GaMnAsP", **Phys. Rev.B**, 82, 104422 (2010)

- S. Haghgoo, **M. Cubukcu**, H. J. von Bardeleben, L. Thevenard, A. Lemaître and C. Gourdon " Exchange constant and domain wall width in GaMnAsP films with self-organization of magnetic domains",**Phys. Rev.B (Rapid communication)**, 82, 041301(R) (2010)

- **M. Cubukcu**, H.J. vonBardeleben, J.L. Cantin, A. Lemaître "Temperature Induced In-Plane/Out-of-Plane Magnetization Transition in Ferromagnetic GaMnAsP Thin Films", **Appl. Phys. Lett.** 96, 102502 (2010)

- **M. Cubukcu**, H.J. vonBardeleben, Kh. Khazen, J.L. Cantin, O. Mauguin, L. Largeau and A. Lemaître, "Adjustable anisotropy in ferromagnetic GaMnAsP layered alloys" **Phys. Rev.B (Rapid communication)**, 81, 041202(R) (2010)

- **M. Cubukcu**, H.J. vonBardeleben, Kh. Khazen, J.L. Cantin, M.Zhu, M. Wilson, P. Schiffer and N. Samarth "Ferromagnetic Resonance Study of MnAs/GaMnAs Bilayers" **J. Appl. Phys.**, 105, 07C506 (2009)

- Kh. Khazen, H.J. vonBardeleben, **M.Cubukcu**, J.L. Cantin, V. Novak, K. Olejnik, M. Cukr, A. Lemaître "Anisotropic magnetization relaxation in ferromagnetic GaMnAs thin films" , **Phys. Rev.B**, 78, 195210 (2008)

The subject of this thesis is the experimental study of the magnetic anisotropy in thin ferromagnetic semiconductor films and the magnetic coupling in bilayers formed with ferromagnetic metals. I have focussed my studies on two different systems: quaternary ferromagnetic GaMnAsP thin films and MnAs/GaMnAs bilayers. In these systems I have investigated how the magnetic anisotropies are influenced by the lattice mismatch induced biaxial strain and the hole concentration. The principal experimental techniques used are ferromagnetic resonance spectroscopy, SQUID magnetization measurements as well as transport and high resolution X-ray diffraction.Two series of GaMnAsP layers characterized by different Mn concentrations of 7% and 10% were investigated. For each series the P concentration has been varied over a wide range from 0 to 20%. Of particular interest is the case of highly P doped layers where the conductivity regime changes from metallic to impurity band conduction. This change induces a profound modification of all pertinent magnetic parameters (T_c, M_{sat}, uniaxial anisotropy). The variation of the four anisotropy constants as a function of temperature and P has been determined. For intermediate P concentrations layers with zero uniaxial strain can be obtained. The temperature induced magnetization reorientations have been evidenced for 6% doped P. High frequency FMR measurements have been used to study the magnetic anisotropy of MnAs epitaxial films on (111) and (100) GaAs. A ferromagnetic exchange coupling has been evidenced for MnAs/GaMnAs bilayers.I have further studied the magnetization relaxation via the Gilbert damping factor which has been deduced from FMR linewidth studies at two different microwave frequencies.

***

Cette thèse présente une étude de l'anisotropie magnétique de semiconducteurs ferromagnétiques en couches minces et du couplage magnétique dans des bicouches formées à partir de ces matériaux et de métaux ferromagnétiques. Je me suis focalisé sur deux systèmes distincts : des films minces de l'alliage quaternaire GaMnAsP et des bicouches : MnAs/GaMnAs. Dans ces systèmes, j'ai étudié l'influence sur les anisotropies magnétiques d'une part, de la déformation biaxiale induite par le désaccord de maille avec le substrat et d'autre part, de la concentration en trous. Ces études ont été menées principalement par résonance ferromagnétique, mesures d'aimantation par SQUID, ainsi que grâce à des mesures de transport et de diffraction de rayons X à haute résolution.Deux séries de films de GaMnAsP caractérisées par des concentrations en Mn de 7 et 10% ont été étudiées. Pour chaque série, la concentration en P a été variée sur une large gamme de 0 à 20%. Les forts dopages en P sont intéressants car le régime de conduction peut changer, passant de métallique à bande d'impuretés. Ceci induit de profondes modifications de tous les paramètres magnétiques pertinents (T_c, M_{sat}, constantes d'anisotropies). Nous avons étudié les variations d'anisotropie magnétique avec la concentration en P. Une réorientation de l'aimantation avec la température a pu être mise en évidence pour une concentration 6% P.Des mesures de RFM à haute fréquence ont permis d'étudier l'anisotropie magnétique de films de MnAs épitaxiés sur (111) et (100) GaAs. Un couplage d'échange ferromagnétique est mis en évidence pour les bicouches MnAs/GaMnAs.La relaxation de l'aimantation de ces systèmes a été étudiée via le facteur de Gilbert, déterminé à partir de l'étude de la largeur des résonances en fonction de la fréquence des microondes utilisées.